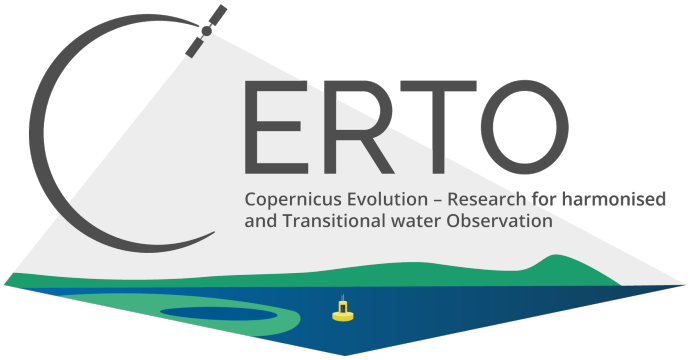

Horizon 2020

H2020 LC-SPACE-04-EO-2019-2020

Copernicus Evolution – Research for harmonised and Transitional-water Observation (CERTO)

Project Number: 870349

Deliverable No: D5.4		Work Package: 5	
Date:	27-FEB-2023	Contract delivery due date	30-SEP-2022
Title:	Final product evaluation and description of algorithmic evolutions		
Lead Partner for Deliverable	HYGEOS		
Author(s):	François Steinmetz, Didier Ramon, HYGEOS		
Dissemination level (PU=public, RE=restricted, CO=confidential)			PU
Report Status (DR = Draft, FI = FINAL)			DR

Acknowledgements

This project has received funding from the European Union's Horizon 2020 research and innovation programme grant agreement N° 870349

Table of Contents

1 Executive Summary

- The Polymer atmospheric correction (AC) algorithm has been updated based on the first analysis performed in D5.1, to improve the performance over the complex waters that occur in transitional waters:
    - The water reflectance model implemented in Polymer has been updated to improve the algorithm performance over turbid waters.
    - The spectral optimisation scheme has been improved and the SWIR bands from the MSI and OLCI sensors onboard Sentinel-2 and Sentinel-3 have been added, to improve the algorithm stability over complex waters.
    - An optional scheme for correcting for vegetation adjacency effects, to which the Polymer algorithm is more sensitive than to other types of adjacency effects, has been implemented.
    - These updates have been released in the public version of Polymer.
- A method for detecting the areas affected by bathymetry effects, based on timeseries of Sentinel-2 images with varying tides, has been implemented. This method uses, as external information, the high-frequency water level at the considered site. This allows identification of the areas where bathymetry effects can have an impact on the atmospheric correction, where the estimated water properties can be biased by the seabed visibility.
    - As by-products of this method, the bathymetry and seabed albedo are derived.
- A validation of different AC algorithms has been carried out, using the in-situ database collected in the CERTO campaigns (WP3) and historical data over the case study sites. This validation was performed for the OLCI and MSI sensors, respectively onboard the Sentinel-3 (A and B) and Sentinel-2 (A and B) platforms. This validation showed improved performance of the modified Polymer algorithm, compared with the legacy Polymer. The best performance was obtained by this modified version of Polymer compared with the other AC, with close results from C2RCC/C2X.
- Further analysis of images allowed the characterisation of the results for even more complex cases, in particular extremely turbid waters, which can be better handled by image-based algorithms such as ACOLITE, at the expends of a higher sensitivity to variations of the atmospheric properties across the image.
    - Based on these observations, an approach is proposed for merging the Polymer and ACOLITE algorithms, to optimise the results from clear to extremely turbid waters.

2 Introduction

Atmospheric Correction (AC) is a critical step in the monitoring of transitional waters. The water colour is a weak signal compared to the Rayleigh, aerosol and other contaminating signals, and is complex to estimate accurately; in coastal environments, lagoons and estuaries, this estimation is even more challenging because of the complexity of the water types, but also because of additional perturbations, in particular the adjacency effects due to the light scattered by bright adjacency land surfaces, but also due to the seabed visibility in presence of bathymetry effects.

WP5 has focused on addressing these challenges by studying and improving the AC algorithm Polymer, in view of harmonising the approaches implemented in different Copernicus services (C3S, CMEMS and CLMS). The modifications implemented in the Polymer algorithm are presented in the section 3.1 of this report; they have been based on theoretical studies using the radiative transfer simulations that were carried out in the first year of the project, but also made use of the in-situ data gathered in CERTO WP3 to improve the adequacy of the water reflectance model implemented in Polymer to the actual water properties of the CERTO case study sites. Various aspects of Polymer were adjusted to improve the algorithm behaviour over turbid waters and the algorithm stability in presence of complex waters. A method for propagating radiometric uncertainties from top-of-atmosphere to the final water reflectance has also been implemented in Polymer.

A dedicated method to mitigate the adjacency effects due to vegetation was also implemented in Polymer and was evaluated based on the processing of images and radiative transfer simulations. These developments are described in section 3.3.

Attempts were made to take the bathymetry effects into account in the AC scheme, to retrieve the water reflectance as if the seabed was not visible (thus, as if all pixels were optically deep). However, this scheme involved many unknowns, on the atmospheric properties, water optical properties, depth and seabed albedo. Therefore, it is extremely challenging to retrieve all these parameters and conclusive minimisation could not be achieved. We have, however, made a significant step towards the estimation of the bathymetry effects, by first identifying the pixels affected by the seabed visibility, and then retrieving the bathymetry and seabed albedo based on a series of assumptions (spatial homogeneity of the water, temporal averaging). This work is presented in section 3.2.

An important part of WP5 was to study and compare various AC schemes, to identify the most appropriate ones for transitional waters. The extensive in-situ database gathered in WP3 was used to validate several AC algorithms and identify their characteristics and limitations. Major features due to the design of the various algorithms (pixel-based or image-based) were identified, and the improvements to the Polymer atmospheric correction verified in the validation exercise (section 4.4). In addition to the analysis using in-situ data, sample scenes were visualised and studied over the case study sites, also in view of the work carried out in WP4 regarding the Optical Water classification.

Finally, as a result of this analysis, a method is proposed to merge two AC algorithms to optimise their performance and propose a state-of-the-art demonstration CERTO processor.

3 Algorithm improvements

3.1 Optimisation of Polymer for transitional waters

3.1.1 Objective

The Polymer atmospheric correction relies on a model of water reflectance, based on Park and Ruddick (2005). Due to numerical inversion reasons, the number of variables used in this model are limited to two: the chlorophyll concentration and a backscattering coefficient which is the factor f_b in (Park and Ruddick, 2005). Additional parameters could be considered, such as a factor of CDOM absorption or an independent concentration of sediments. However, the introduction of such parameters make it extremely challenging to perform a numerical inversion; we have observed that the spectra of most clear and moderately turbid waters could be accurately represented by this 2-parameter model (Tan et al., 2019). However, this adequacy tends to get lower in presence of very turbid waters: discrepancies between the model and actual turbid reflectance spectra tend to get counterbalanced by the atmospheric correction scheme and result in over-corrections, as noted in Bi et al., (2018).

To minimise this overcorrection, we proposed a modification of the Polymer model to better account for extremely turbid waters, and several other modifications which essentially aim at stabilising the algorithm.

3.1.2 Water reflectance model

3.1.2.1 Update of the model

The modification of the model relies on the introduction of mass-specific absorption coefficients of mineral particles $a^*(\lambda)$ (Röttgers et al., 2014). Ideally, the concentration of mineral particles should be added as an independent parameter but, for reasons of stability of the numerical inversion, this model was not retained. Instead, the first parameter of the model, previously log10(chl), is split into two segments. Let us refer to this parameter as "x". The inherent optical properties are as described in Steinmetz and Ramon (2018), except that an absorption term is added concerning the non-algal particles: $a_{NAP}(\lambda) = f_{NAP} \cdot a^*(\lambda) * SPM$, with $SPM = 100.* b_{bp}(650)$. After x=1, f_{NAP} starts to increase instead of $\log_{10} chl$, as summarised in the following table:

	Chlorophyll	f_{NAP}
Clear mode $\boldsymbol{x \in [-2, 1]}$	$\log_{10} chl = x$	$f_{NAP} = 0$
Turbid mode $\boldsymbol{x \in [1, 2]}$	$\log_{10} chl = 1$	$f_{NAP} = x - 1$

The second parameter of the model, f_b (a factor of backscattering due to phytoplankton and covarying particles), remains as described in Steinmetz and Ramon (2018). This modification results in the following changes, illustrated in "natural colours" (RGB composite) on Figure 1. A difference is visible for x axis values greater than 1, where the updated model is able to reproduce brown (turbid) waters.

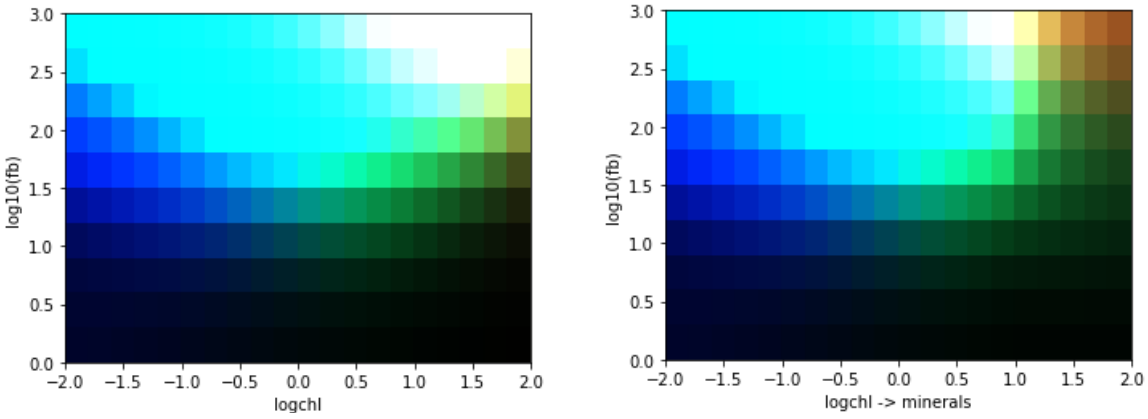

Figure 1: Illustration of the difference between the legacy Polymer water reflectance model (left) and the updated model (right) in « natural colour » (RGB composite).

3.1.2.2 Improvement of the adequacy to CERTO case study sites

The adequacy of the water reflectance model to the in-situ data has been verified, with the objective of improving the capacity of reproducing the in-situ spectra with the updated model, for turbid waters.

To do that, a spectral matching is applied to the in-situ spectra, in a similar way as done in the Polymer scheme but without involving a model for the atmospheric reflectance: in this scheme, the mean squared difference between the in-situ spectral reflectance and the model, is minimised with respect to the two model variables. The resulting points can be plotted in the two-dimensional plane of the model variables (Figure 2). This allows visualisation of how the in-situ points cover this space, with, for example, the Danube points covering a chlorophyll-rich region and the Tamar points covering a region of clearer waters (lower chlorophyll, lower backscattering).

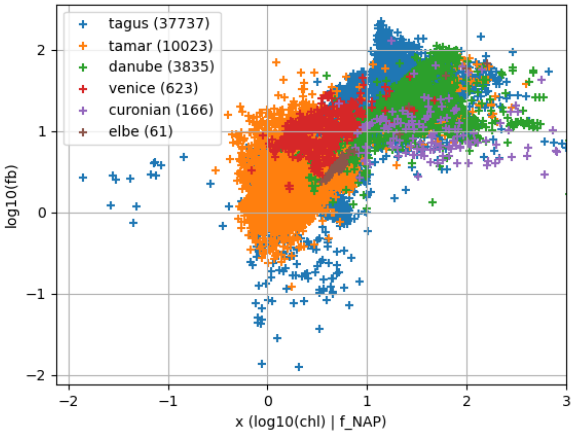

Figure 2: Map of the CERTO in-situ measurements, in the plane of the Polymer model coordinates. Each spectrum is represented as a point in this plane.

The objective is to minimise the residual mean squared difference between the model and measurement, to improve the adequacy of the model. We can compare, for each spectrum, the difference between the residual mean squared difference using the legacy model and using the updated model. A reduction of this quantify means that the updated model gives a better spectral representation of the spectrum than the legacy model. We can indeed see that, for the values of x greater than 1, the updated model is more adequate to the vast majority of the in-situ spectra (Figure 3).

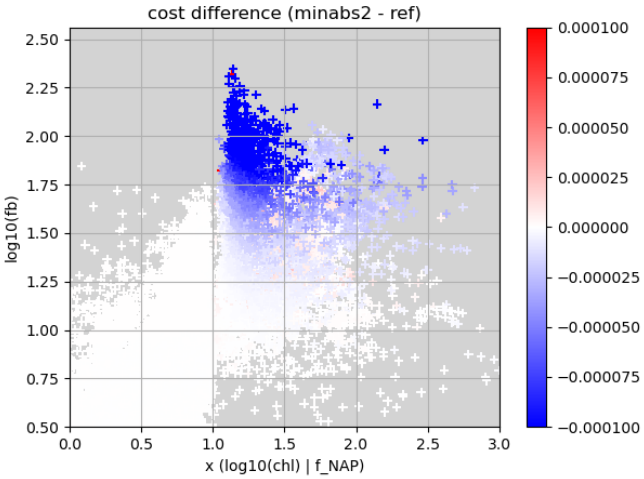

Figure 3: Difference, for each in-situ spectrum represented in the 2-dimensional space of the model parameters, between the residual mean squared difference using the legacy model, and using the updated model. Negative values (blue) indicate a better adequacy of the updated model.

3.1.3 Algorithm stability

In addition to the modification of the water reflectance model, other modifications have been implemented to improve the algorithm stability over complex waters.

3.1.3.1 Use of SWIR bands

SWIR bands have been included to extend the spectral range of the bands considered for atmospheric correction, which allows to better constrain the algorithm. Thus, the band 1020 is now used for OLCI and band 1610 for MSI. The bands used for each sensor are the following:

1) **OLCI**: 443,490,510,560,620,665,754,779,865,1020
2) **MSI**: 443,490,560,665,705,740,783,865,1610

3.1.3.2 Updated first guess

In the standard version of Polymer (Steinmetz and Ramon, 2018), the default point for initialisation is (-1, 0). In case of optimisation failure, a second iteration is attempted starting on point (1, 1). In addition to this, the final point for each pixel is reused as the first guess to minimise processing time. However, this scheme has several drawbacks:

- Inability to converge to the global minimum in some cases (complex waters).
- Possible appearance of “streaks” of bad pixels in case of unstable algorithm behaviour.
- As the processing may depend on the result of previous pixels, there can be a difference between the processing of single points, and images.

Therefore, an alternative first guess has been implemented, by exploring 10 fixed initial points that cover the possible area of solutions. These points are illustrated in Figure 4. The point with minimal value of the cost function is used for the initialisation of the main Nelder-Mead minimisation.

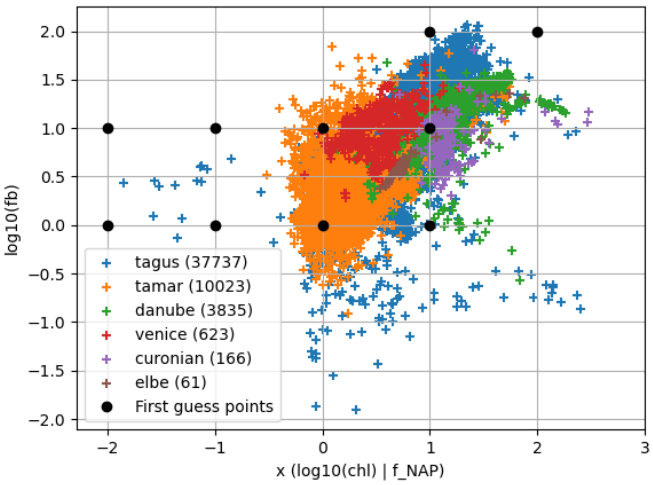

Figure 4: Illustration of the first guess points (in black) in the plane of the water model parameters. The in-situ points are also plotted, as per Figure 2.

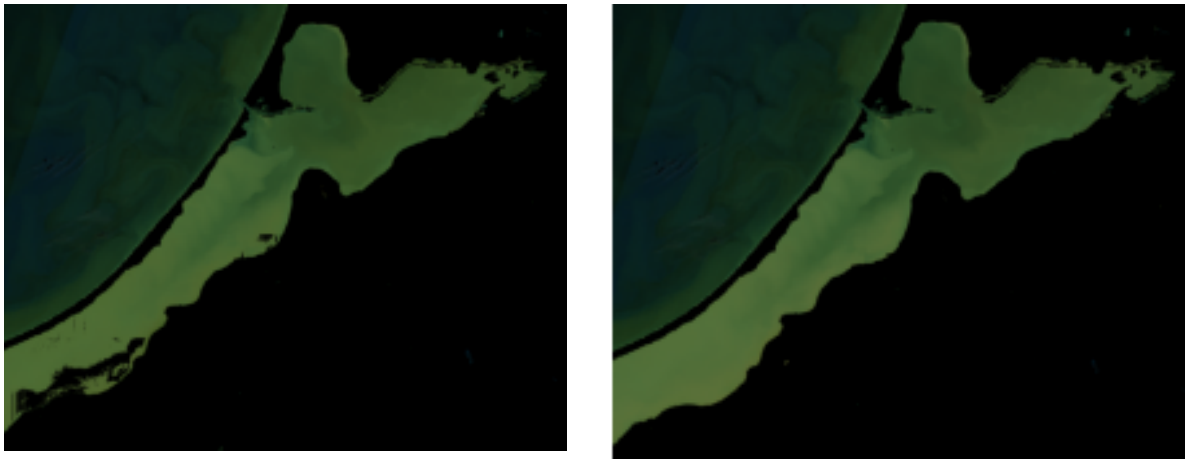

Figure 5: Illustration of the Polymer stability improvement over the Vistula Lagoon with Sentinel-2 MSI (S2B_MSIL1C_20200410T100029_N0209_R122_T34UDF). A region (bottom left of the lagoon) could not be retrieved with standard Polymer (left image), and can be retrieved with the updated Polymer.

These modifications result in an improvement of the algorithm stability, observed on a sample scene over the Vistula lagoon (Figure 5) but also on other scenes.

3.1.3.3 MSI bands weighting

A last modification was introduced to improve the algorithm stability. It aims at avoiding an anomalous behaviour such as illustrated in Figure 6 (MSI). Our interpretation of the issue is that the introduction of the 1610 band increases the algorithm sensitivity to vegetation adjacency effects (in presence of aerosols, because pure Rayleigh scattering would not produce significant adjacency effect at 1610 nm) which can lead to algorithm instability. The position of the 1610 band, far in the SWIR, induces a strong constraint on the spectral optimisation, which is less the case for the 1020 band of OLCI.

To reduce this effect, we have introduced a change in the weighting of the MSI bands in the inversion. Initially, all bands are associated with a weight of unity. The proposed modification leaves all weights to unity, except for MSI band 1610 which takes a weight of 0.01. In the Polymer scheme (Steinmetz et al., 2011; Steinmetz and Ramon, 2018), this weight is not only applied in the cost function to be minimised but also in the inversion of the atmospheric parameters by a linear least square method.

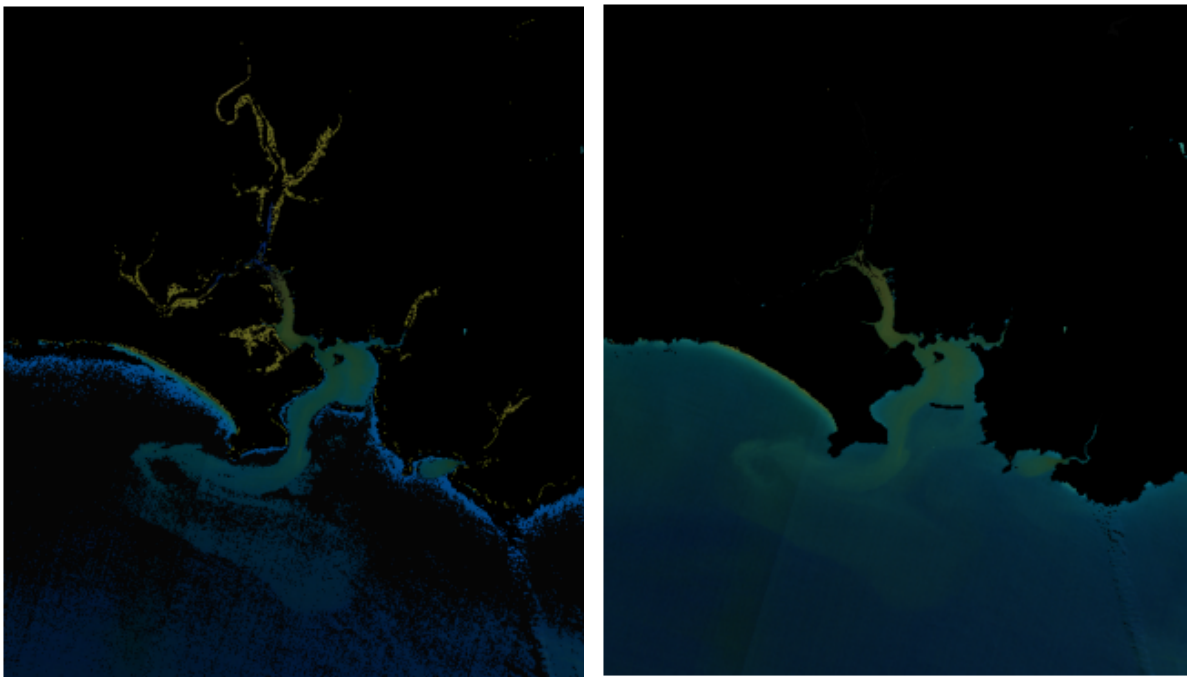

Figure 6: RGB composite of the water reflectance retrieved by Polymer for a MSI image (S2A_MSIL1C_20200409T112111_N0209_R037_T30UVA) over the Tamar estuary, where the updated Polymer configuration (minabs2) is applied without (left) and with (right) adjusted weighting.

3.1.4 Uncertainty estimation

In the past, notably in the ESA Ocean Colour Climate Change Initiative project, uncertainties have been associated to water reflectances based on the validation using in-situ data and through an optical water type classification. However, this scheme only considers the bulk performance of the atmospheric correction, and, therefore, is not tied to the inner mechanisms of error propagation in the atmospheric correction scheme, nor on the atmospheric properties (like observation geometry, aerosol quantity, contamination by sun glint…). It is, therefore, of interest to implement a scheme for providing the errors propagated from the measurements at top-of-atmosphere to the final products by a methodology expressed in the guide to expression of uncertainty of measurements (Fox, 2010; GUM, 2008).

Two sources of uncertainties are considered in the calculation of uncertainties associated with the output parameters:

1. Radiometric uncertainties on the TOA radiances $L_t(\lambda_i)$:

$$u\big(L_t(\lambda_i)\big) = \sigma_{typ}(\lambda_i)\sqrt{\frac{L_t(\lambda_i)}{L_{typ}(\lambda_i)}} \quad (1)$$

where $\sigma_{typ}(\lambda_i)$ is the uncertainty at a typical radiance $L_{typ}(\lambda_i)$, both being provided as characteristics of the OLCI instrument and MSI instruments.
When converted in units of reflectance, the variance-covariance associated with the TOA reflectance ρ_t is:

$$\boldsymbol{C}_{\rho_t} = \begin{pmatrix} \left(\frac{\pi}{\mu_s F_0(\lambda_1)}\right)^2 \sigma_{typ}^2(\lambda_1) \frac{L_t(\lambda_1)}{L_{typ}(\lambda_1)} & \cdots & 0 \\ \vdots & \ddots & \vdots \\ 0 & \cdots & \left(\frac{\pi}{\mu_s F_0(\lambda_n)}\right)^2 \sigma_{typ}^2(\lambda_n) \frac{L_t(\lambda_n)}{L_{typ}(\lambda_n)} \end{pmatrix} \quad (2)$$

2. Uncertainties associated with the model inversion, through the Nelder-Mead inversion. The method used for estimating the error covariance matrix associated with the Nelder-Mead minimisation has been used, and is described in the appendix of their paper (Nelder and Mead, 1965). This method allows to obtain the uncertainties C_x on the parameters associated with the iterative minimisation, which are logchl and logfb. By calculating the sensitivity of the water reflectance $\left[\frac{\partial \rho_{wmod}(\lambda)}{\partial x}\right]$ to the model parameters $x = \begin{bmatrix} \log(chl) \\ \log(f_b) \end{bmatrix}$, one can propagate the uncertainties C_x to the spectral reflectances, by:

$$C_{\rho_w} = \left[\frac{\partial \rho_{wmod}(\lambda)}{\partial x}\right] \cdot C_x \cdot \left[\frac{\partial \rho_{wmod}(\lambda)}{\partial x}\right]' \quad (3)$$

This implementation addresses the major sources of uncertainties (radiometric uncertainties propagated through the main minimisation scheme), and can be used to **assess the uncertainties on the output products**. However, many other sources of uncertainties (either weaker or complex to quantify) could be added to refine the error estimation, such as the uncertainties on the Rayleigh scattering, atmospheric transmittance, gaseous correction, radiometric calibration and atmospheric reflectance model.

3.2 Detection and inversion of bathymetry effect

3.2.1 Method and data

In this section, we present an original and generic method for identifying optically shallow water areas and deriving near-shore bathymetry and seabed albedo from Sentinel-2 observations. We aim to publish this method in a peer-reviewed journal. The baseline for this method is the detection of the areas contaminated by bathymetry effects, for purposes of masking. Its extension to bathymetry and seabed albedo estimation differs from most Satellite-Derived Bathymetry (SDB) methods which generally focus on clear waters or use empirical methods (Ashphaq et al., 2021).

The current method is based on the variation of the apparent reflectance (in presence of optically shallow waters) with the water level; therefore, it is applicable to coastal areas with relatively high tidal amplitude. It uses the following data:

1) Timeseries of Sentinel-2 data over a region of interest. The time range is typically one year. The water reflectance is retrieved by using the ACOLITE atmospheric correction algorithm (Vanhellemont, 2019; Vanhellemont and Ruddick, 2018). This algorithm is chosen because it is by construction unaffected by bathymetry effects (seabed visibility), unlike other alternatives such as Polymer or C2RCC.
2) The timeseries of water level over this region of interest. The measurement period must be sufficiently short for an accurate interpolation of the water level at the time of measurement. The region of interest must be sufficiently small for considering that the

water level is homogeneous over the whole region of interest. The mains source of water level data considered here is European Commission. Joint Research Centre. (2018).

The method uses a model of shallow water reflectance from Lee et al (1998).

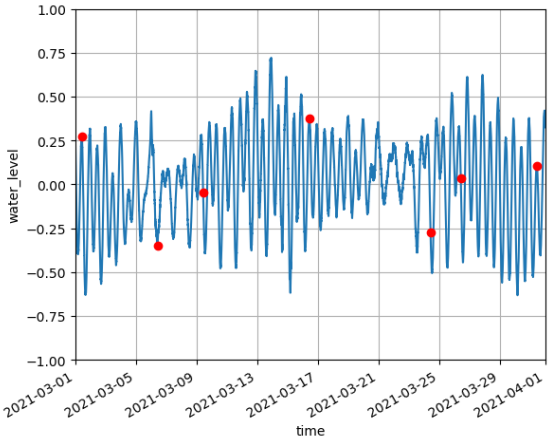

Figure 7: Illustration of the water level timeseries for the Venice lagoon over a month. The red dots represent Sentinel-2 cloud-free images.

To illustrate this method, let us consider an optically shallow region nearby Venice (see Figure 8).

Figure 8: The region of interest (south of Venice) used as an example in this section.

3.2.2 Overall scheme

The overall algorithmic scheme of the bathymetry effect characterisation method is presented in Figure 9. We emphasise that only the first algorithmic step (correlation calculation) is required to identify and mask the pixels affected by bathymetry effects. The other steps are further steps allowing to characterise the bathymetry and seabed albedos, i.e., additional outputs beyond that planned in CERTO.

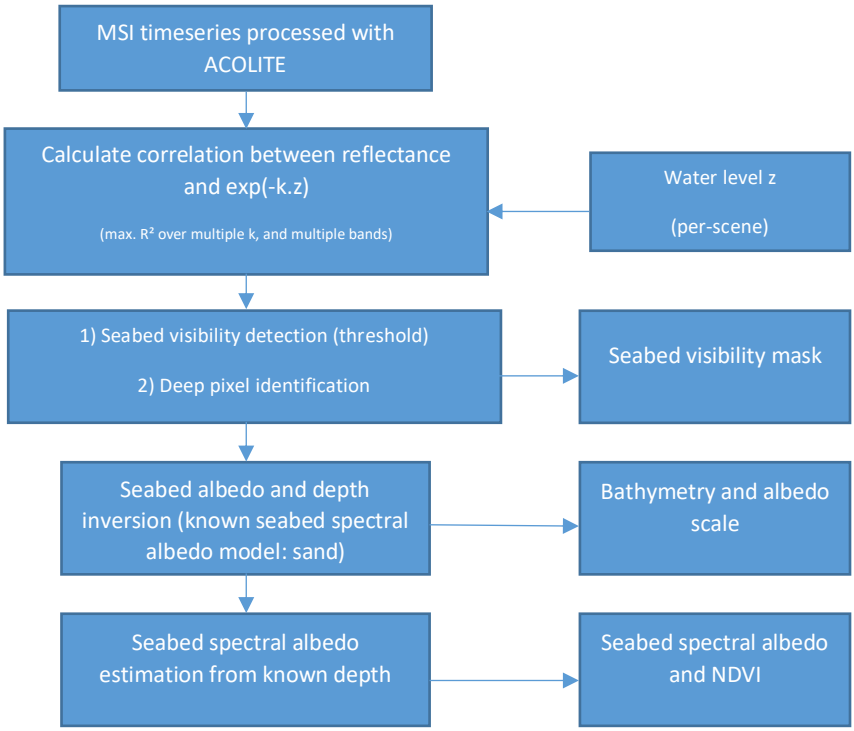

Figure 9: Algorithmic scheme of the bathymetry and seabed estimation.

3.2.3 Bathymetry effects detection

The first step consists of identifying the optically deep and optically shallow pixels. This step is performed by considering the following approximation, derived from eq. 3 of Lee et al. (1999) by approximating both exponentials to be equal to $\exp(-k \cdot z)$, where z represents the depth, which varies pixel by pixel and over time. The spatial variability can be decoupled from the temporal variability:

$$z(i,j,t) = Z(i,j) + H(t)$$

Where $Z(i,j)$ is the pixel-by-pixel bathymetry that we want to retrieve, and $H(t)$ is the water level, assumed to be homogeneous over the image and known from external information.

By approximating the two exponentials to be equal in eq. (9) of Lee et al. (1999), the total (apparent) under-water remote sensing reflectance can then be written as:

$$r_{rs} = r_{rs}^{dp} + (\frac{\rho}{\pi} - r_{rs}^{dp}) * \exp(-k \cdot z)$$

This relationship translates into a correlation between the observed remote sensing reflectance r_{rs} and the coefficient $\exp(-k \cdot z)$. More importantly, the resulting correlation coefficient is insensitive to an offset on z. Therefore, the knowledge of $Z(i,j)$ is not mandatory, and the regression can as well be computed between $r_{rs}(i,j,t)$ and $\exp(-k \cdot H(t))$. This correlation is performed pixel by pixel and results in a correlation coefficient $r^2(i,j)$. Since the coefficient k in the previous equation is not known, the regression is performed for several typical values of k: 0.5, 1 and 2. It is also performed at several wavelengths: 560, 665 and 705nm. The maximal r^2 value over these multiple values of k and spectral band is selected. The result of this process is illustrated on Figure 10.

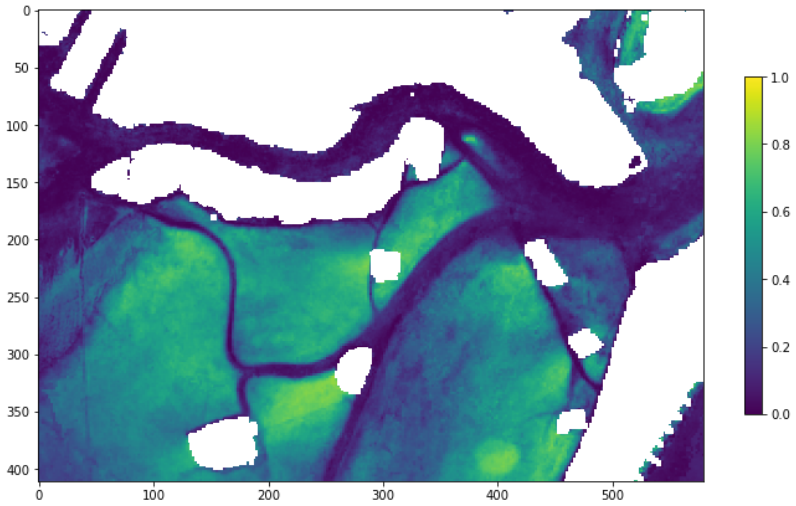

Figure 10: Estimation of the tidal correlation coefficient $r^2(i,j)$ which quantifies the impact of bathymetry effects. Low values indicate optically deep pixels. Significant bathymetry effects can be detected with $r^2(i,j) > 0.2$.

3.2.4 Water inherent optical properties inversion

This map of $r^2(i,j)$ is used to identify optically deep pixels: the pixel with the lowest value of r^2 is selected: its coordinates are (i_0, j_0). The next assumption is that **the optical properties of this optically deep pixel can be extrapolated to the whole area of interest** (assumption of spatial homogeneity). It is a strong assumption, but it avoids the complex and error-prone pixel-by-pixel estimation of the water inherent optical properties, which in presence of bathymetry effects is a very complex task.

Then, for this optically deep pixel (i_0, j_0), with reflectance $\rho_{w,deep}(\lambda, t)$ the model used in Polymer (Steinmetz and Ramon, 2018) is used to determine the absorption ($a_{tot}(\lambda, t)$) and backscattering ($b_{btot}(\lambda, t)$) properties of the water, for each image. This is done in a similar scheme as in Polymer, by minimising for each time slot t, the difference between the observed spectrum $r_{rs}(\lambda, t)$, which is converted into above-surface reflectance, and a model of water reflectance based on Park and Ruddick (2005). As in Polymer, a simplex minimisation scheme (Nelder and Mead, 1965) is applied, but in this case without a model for the atmospheric reflectance.

Finally, this minimisation provides for each area at time t, the spectral absorption and backscattering properties $a_{tot}(\lambda, t)$ and $b_{btot}(\lambda, t)$.

3.2.5 Bathymetry inversion

Two parameters are determined pixel-by-pixel, by iterative minimisation:

1) The bathymetry, Z
2) The seabed albedo amplitude expressed in log to ensure positivity, $\alpha_0 = \log a_0$, assuming a spectral model. The spectral albedo is then $a(\lambda) = \exp \alpha_0 \cdot a_{model}(\lambda)$. In a first step, the sand model is used.

$$cost(Z, \alpha_0) = \sum_{\lambda,t} \left(\rho_{w,obs}(\lambda, t) - \rho_{w,model}(\lambda, Z, \alpha_0, t) \right)^2$$

The sum considers the 1-year Sentinel-2 timeseries (t) and the spectral bands λ: 443, 490, 560, 665nm.

In this function, the mean square difference between the observed water reflectance ($\rho_{w,obs}$) and a model ($\rho_{w,model}(\lambda, Z, \alpha_0, t)$) is minimised. This model uses Lee et al. (1998) to account for the seabed albedo and uses the following inputs:

- The seabed albedo is $a(\lambda) = \exp \alpha_0 \cdot a_{sand}(\lambda)$
- The absorption and backscattering spectra series are used as determined at previous stage: $a_{tot}(\lambda, t)$ and $b_{btot}(\lambda, t)$.
- The total depth is Z+H(t)

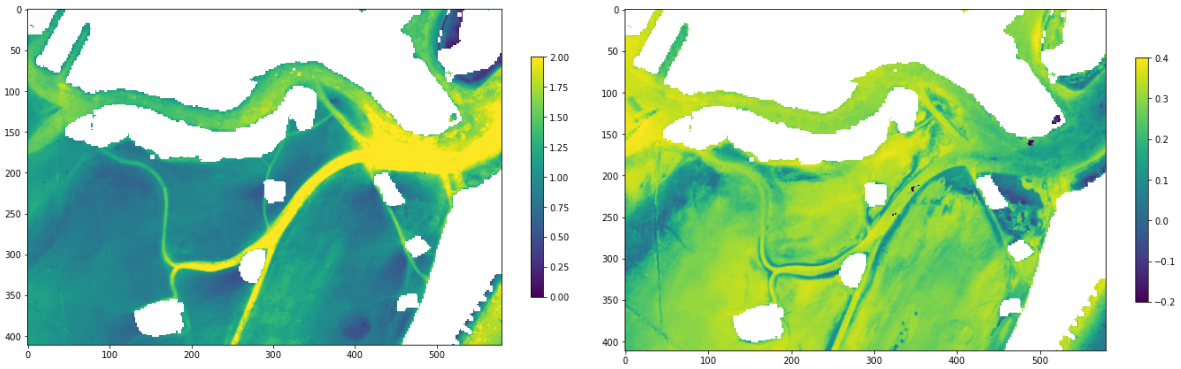

Figure 11: Sample results of the bathymetry inversion: Z in m (left), and α_0 (right)

The Nelder-Mead method (Nelder and Mead, 1965) is applied to optimise the parameters Z and α_0. The resulting values of Z were compared with published maps, showing a good consistency (Figure 12). A density map was generated to compare these products (Figure 13); a good consistency appears for depths lower than 1.6m. However, these results should be taken with caution, due to the time difference between the map retrieved by the current algorithm (2020) and the published historical data (2002).

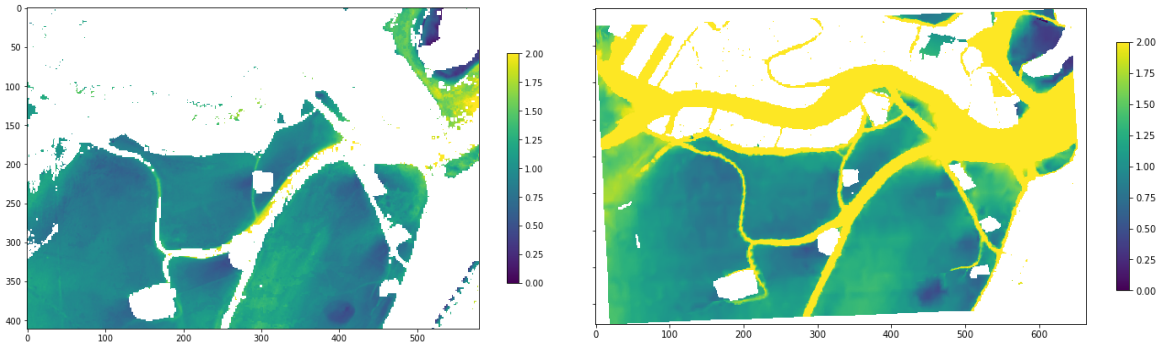

Figure 12: Comparison between the bathymetry retrieved by the current algorithm (left) and a bathymetry map of the Venice lagoon (right) from Zaggia et al. (2017)

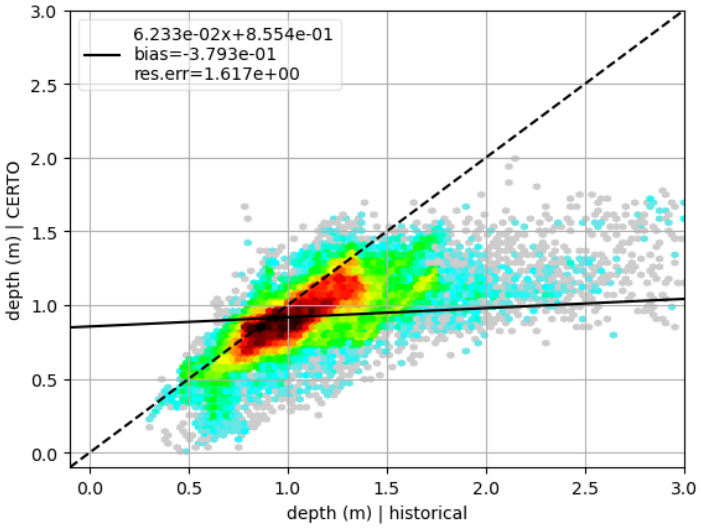

Figure 13: Comparison of the depth estimated on the region of interest in the Venice lagoon, compared with historical data (Zaggia et al., 2017).

The bathymetry model from Lee et al. (1998) was also verified using the radiative transfer simulations carried out in the first year of the project (D5.2): Figure 14 shows the results from this comparison, for different albedo models (from top to bottom, Seagrass, Sand and Rock) and different types of water (from left to right, clear waters, mesotrophic waters and turbid waters). A very good consistency is achieved between the model and the radiative transfer simulations. Significant differences appear for turbid waters, in which case the seabed albedo is almost not visible from a depth of 0.5m (minor difference between depths of 0.5 and 2m).

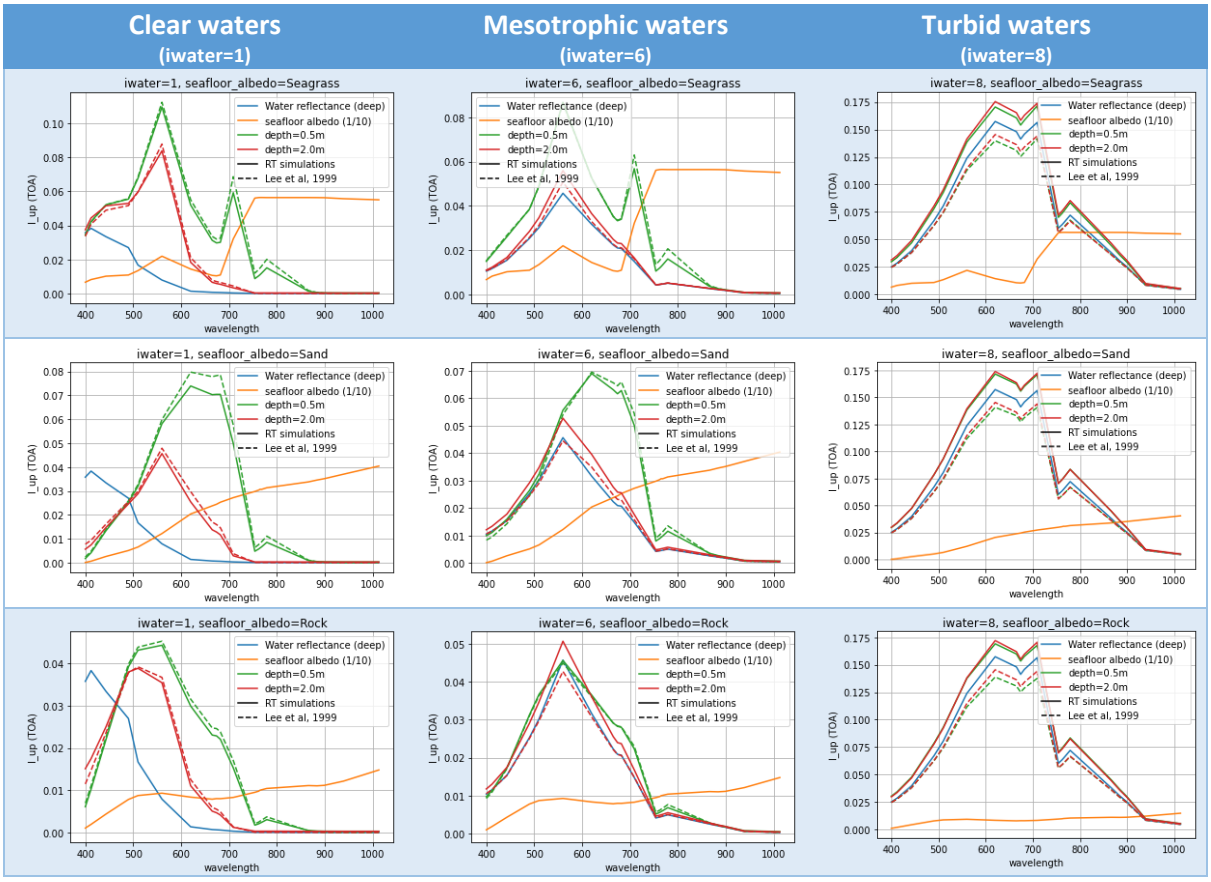

Figure 14: Comparison of the bathymetry model of (Lee et al., 1998) to the radiative transfer simulations carried out in WP5 (D5.2), for different types of water (columns) and different models of seabed albedo (rows). Each plot shows the seabed albedo in orange, the deep water reflectance in blue, and the comparison of the model to the radiative transfer simulations for two depths, 0.5m and 2m.

3.2.6 Seabed mapping

With a known bathymetry Z, it is possible to use the Lee et al. (1998) model to derive the spectral albedo $a(\lambda)$ from the observations $\rho_{w,obs}(\lambda)$, all other parameters being known:

$$a(\lambda) = \frac{\rho_{w,obs}(\lambda,t) - \rho_{w,deep}(\lambda,t) \cdot (1 - \exp(-k_1(Z + H(t))))}{\exp(-k_2(Z + H(t)))}$$

This inversion allows to obtain an estimation of the spectral seabed albedo, independently from the model used previously.

These values of spectral albedo are then used to calculate a vegetation index ($NDVI = \frac{a(705)-a(665)}{a(705)+a(665)}$), as illustrated on Figure 15.

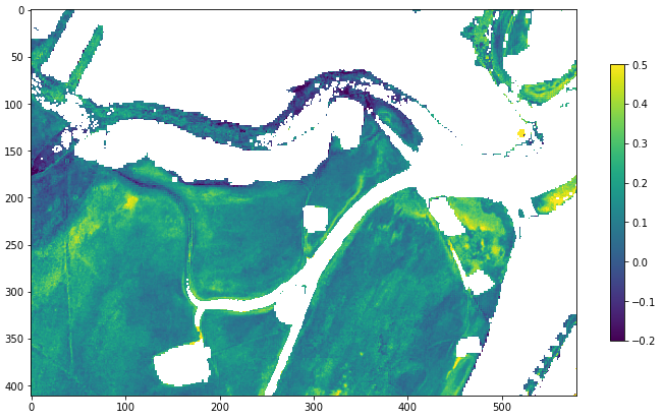

Figure 15: NDVI of the seabed albedo, using the bands 665 and 705 nm. Increased values are seen in the seagrass areas, at the south of the western part of the Giudecca Island, the Island immediately at the south of the central Island (see the patch corresponding to this seagrass area on Figure 8).

3.3 Adjacency effects: impact and mitigation

3.3.1 Adjacency effect: impact on different types of atmospheric correction

The adjacency effects are caused by the reflection by adjacent surfaces, of photons which are then scattered in the sensor direction. This effect can significantly impact atmospheric correction, and reduce the capacity to observe coastal waters, especially with dense land surroundings as is frequently the case for transitional waters. The impact varies depending on the type of atmospheric correction, due to their different designs:

1) **Image-based** atmospheric correction such as ACOLITE (Vanhellemont, 2019; Vanhellemont and Ruddick, 2018): these algorithms assume a spatial homogeneity of the atmosphere over a region of interest, typically a satellite image. With this assumption, the adjacency signal is **directly propagated** to the water reflectance. Therefore, the impact is maximum for bright albedos such as snow/ice. This type of atmospheric correction can still benefit from dedicated

adjacency correction methods such as SIMEC, applied to the iCOR atmospheric correction (Keukelaere et al., 2018).

2) **"Standard"** atmospheric correction, as initially developed for SeaWiFS by (Gordon and Wang, 1994), then adapted to other sensors (e.g., for MERIS: (Antoine and Morel, 1999)). In this scheme, the aerosol optical thickness and model are estimated in the red and near infrared bands and extrapolated to the visible bands. In this scheme, the adjacency signal is generally amplified by the atmospheric correction. This scheme **is very sensitive to** bright albedos such as **snow/ice but also vegetation** adjacency because of its strong impact on near infrared bands.
3) **Coupled** atmospheric corrections such as C2RCC/C2X (Doerffer and Schiller, 2007) or Polymer (Steinmetz et al., 2011; Steinmetz and Ramon, 2018): these algorithms rely on a model of water reflectance and, therefore, can use the blue and green bands to perform atmospheric correction. These algorithms have **the highest capacity to compensate the adjacency effects**.

3.3.2 Impact of adjacency effects on Polymer

It is well known that Polymer is very **robust to the adjacency effects** (Alikas et al., 2020; Pan et al., 2022). This is due to the fact that the adjacency signal is being fitted and corrected by the atmospheric reflectance model through Polymer's minimisation scheme; the possibility to rely on a model of water reflectance greatly improves the possibility of mitigating adjacency signal. However, the **spectral shape** of the adjacent albedo may have an impact on the capability of Polymer to correct for the adjacency signal. While it is clear that spectrally smooth albedo (e.g. sand, snow) can be corrected by Polymer's atmospheric reflectance model because it is by construction able to correct for spectrally smooth signals (it has been shown for snow and ice adjacency in the Arctic region in König et al. (2019)), the behaviour in presence of **vegetation adjacency**, which presents a strong spectral signature in the red (the "red edge"), is not obvious.

To answer this question, the radiative transfer simulations (D5.2) have been used to study the behaviour of Polymer in the presence of different types of adjacency effects, considering various cases for the atmosphere (aerosol optical thickness and aerosol model), for the water reflectance (from clear to turbid waters) and adjacency effects (4 albedo models; several distances to the linear shoreline). Examples of spectra with adjacency effects at top of atmosphere, and at bottom of atmosphere after atmospheric correction by Polymer, are shown in Figure 16. These examples show the good consistency of the retrieved water reflectance, despite large impacts on the TOA reflectance (up to 5% reflectance for the snow adjacency); they also show how the vegetation (grass) adjacency affects differently the retrieved water reflectance, leading to an artefact around 700nm, but also a stronger effect in the blue for the shortest distance (250m).

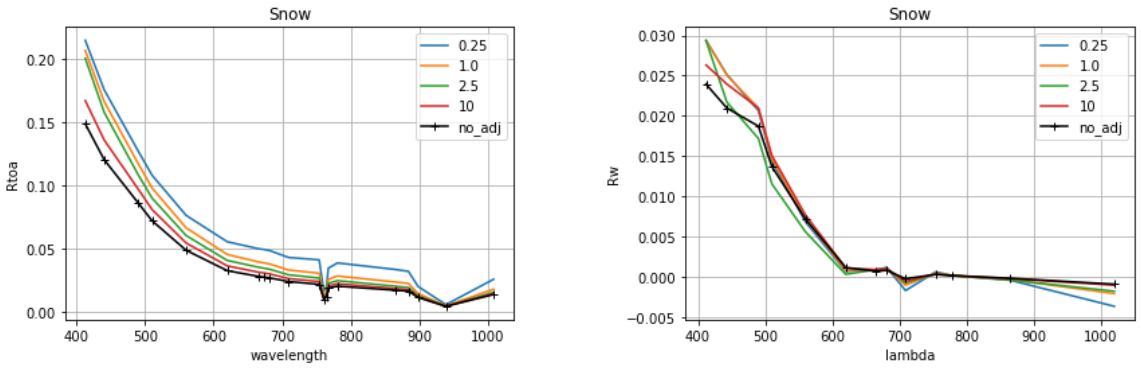

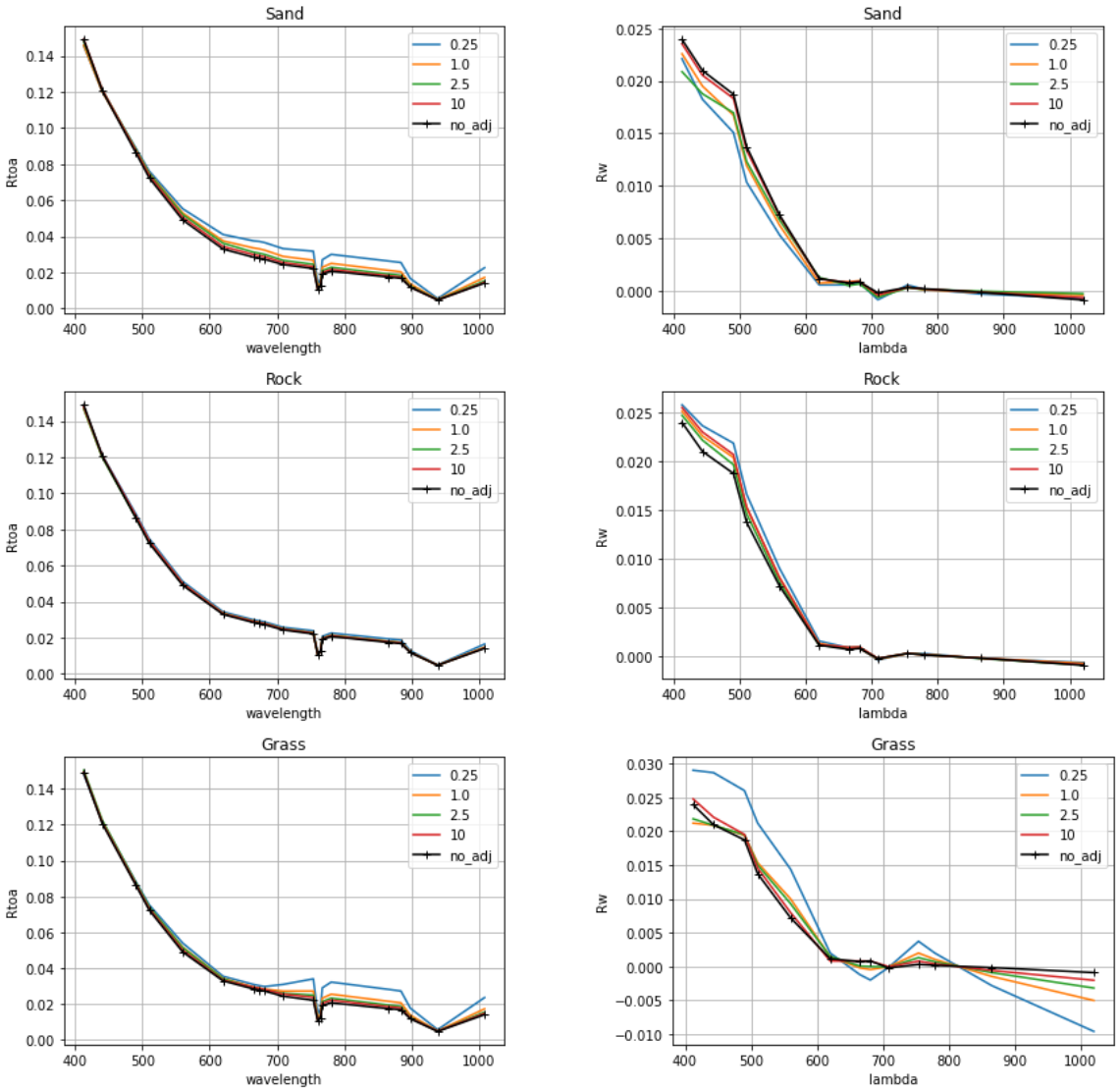

Figure 16: Impact of adjacency effect on top-of-atmosphere (TOA) sample OLCI simulated spectra (left column), with different albedo models (from top to bottom: snow, sand, rock and grass). Multiple distances to the linear coastline from 250m to 10km are shown on each plot, as well as the reference spectrum without adjacency effect. The corresponding spectra of water reflectance after atmospheric correction by Polymer are shown in the right column.

With additional spectra (multiple atmospheric conditions, multiple water reflectances), and considering all spectral bands altogether, we can plot the relative or the retrieved water reflectance as a function of the relative error on the TOA signal (Figure 17). This plot confirms that the **vegetation adjacency has the strongest relative impact on Polymer**, because low relative errors at TOA result in high relative errors at bottom of atmosphere. On the contrary, snow adjacency has a strong relative impact at TOA, but a lower impact at BOA.

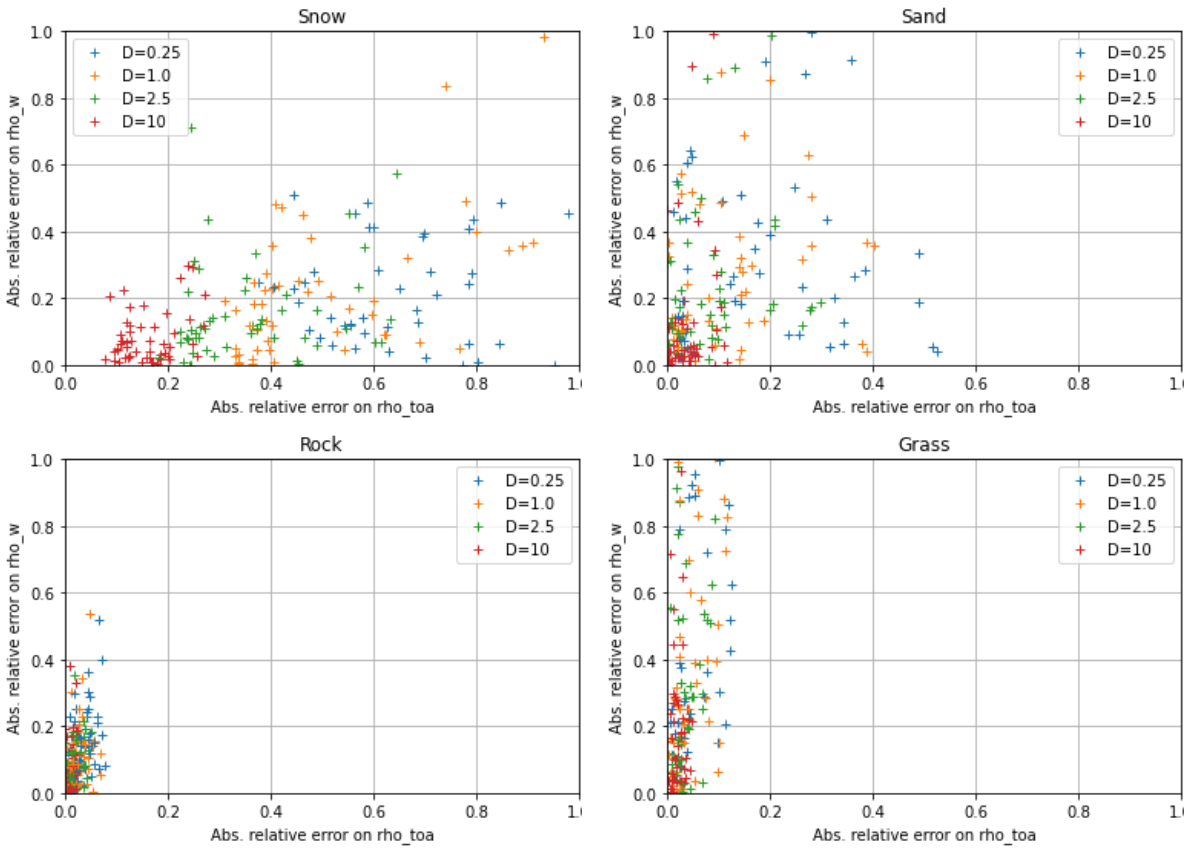

Figure 17: Relative error on water reflectance due to adjacency, as a function of relative amplitude of adjacency signal on TOA reflectance. The reference is the case without adjacency signal. Each plot shows a different albedo model and various distances are shown in colour, from 250m to 10km.

3.3.3 Mitigation of vegetation adjacency on Polymer

3.3.3.1 Method

Based on these observations, it is interesting to implement a method to mitigate the vegetation adjacency in Polymer. To do that, we proposed to add a fourth component to the atmospheric reflectance model used in Polymer (Steinmetz et al., 2011). This component is designed to fit a vegetation adjacency signal, which can be modelled as the vegetation reflectance $\rho_{veg}(\lambda)$, multiplied by λ^{-4} to account for the Rayleigh transmission. The vegetation reflectance (see Figure 18) is taken from the ECOSTRESS spectral library (Meerdink et al., 2019).

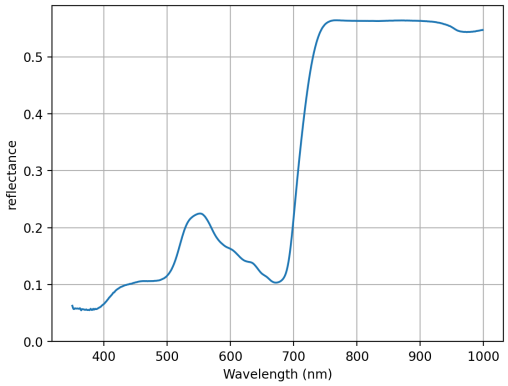

Figure 18: Vegetation reflectance (grass) from the ECOSTRESS spectral library (Meerdink et al., 2019), implemented in the vegetation adjacency correction

The resulting atmospheric model then is:

$$\rho_{atm}(\lambda) = T_0(\lambda)c_0 + c_1\lambda^{-1} + c_2\rho_{mol}(\lambda) + c_3\rho_{veg}(\lambda)\lambda^{-4}$$

In this expression, the new unknown associated with the vegetation adjacency signal is c_3. Due to the design of the Polymer atmospheric correction, in which the c_i coefficients are not derived iteratively but analytically by matrix multiplication (Steinmetz et al., 2011), the additional processing time is minimal. However, there is a risk to create instabilities in the inversion by introducing this new parameter.

3.3.3.2 Results

The stability of the inversion with the new parameter was checked on an OLCI sample scene over the black sea (S3A_OL_1_EFR____20170913T080543) which exhibits a coastline with dense forests (see Figure 19). We can see that the retrieval is stable (no anomalous sharp pixel-to-pixel transition – see the discussion in section 3.1.3). This stability is good news, because the Polymer atmospheric model was never tested with 4 parameters, and the stability of inversion is a critical aspect of the inversion by Polymer.

We can also see that the changes introduced by the vegetation adjacency correction are limited to the coastline; this correction reduces the underestimation of rho_w(665). This underestimation is visible on the map but also expected from the simulations (section 3.3.2). The reflectance at 412nm is also slightly reduced by the vegetation adjacency correction at the shoreline. Finally, the coefficient c_3 clearly increases at the shoreline. These observations are not validations, rather observations of sane behaviour. The evaluation of this option is further developed in the following sections.

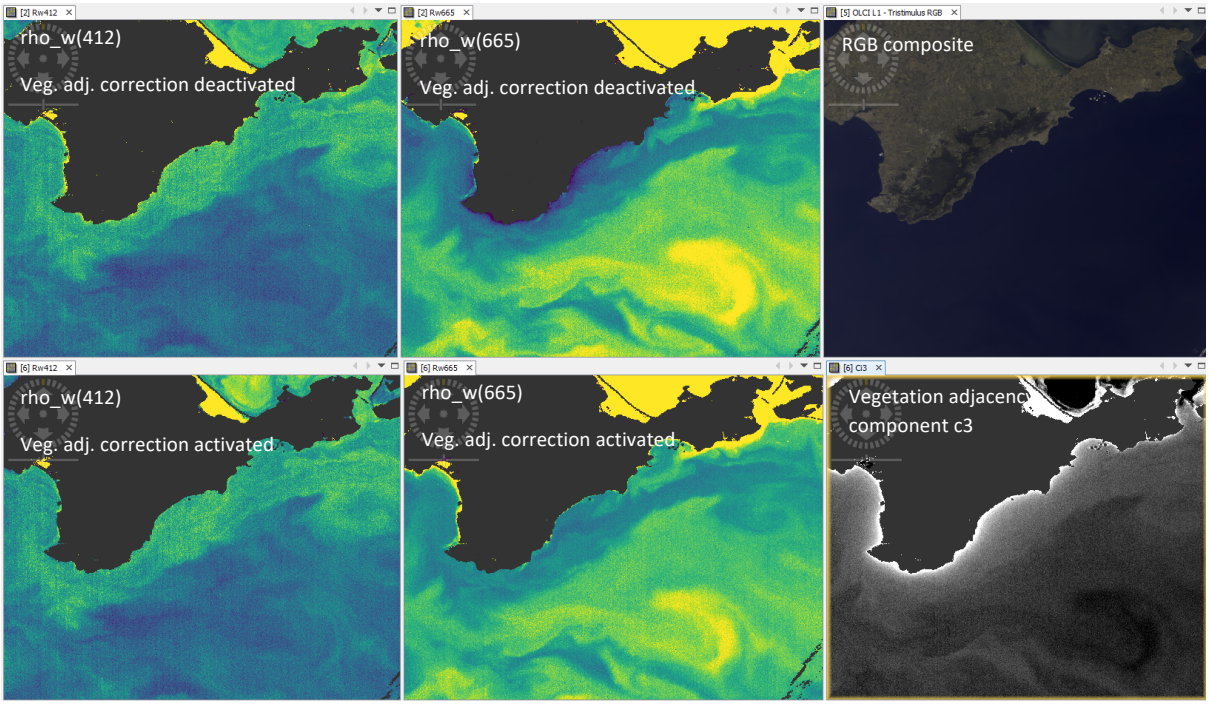

Figure 19: Polymer estimated water reflectance at 412 (left) and 665nm (right) without (top) and (with) the correction for vegetation adjacency. A RGB composite of the Rayleigh-corrected signal is shown in the top-right plot, and the vegetation adjacency component is shown in the bottom-right.

To further validate the sensitivity of the algorithms to the adjacency effects, the difference between satellite water reflectance estimation and in-situ measurement was compared with an index of the adjacency effect, obtained by convolving the top of atmosphere reflectance with the atmospheric point spread function (Santer and Schmechtig, 2000). This convolution was performed by applying a cloud mask, since clouds do not contribute to adjacency effects to the same extent as emerged land. However, the results, not presented in this document, were not conclusive and no significant correlation with this adjacency effect index could be observed. This lack of correlation indicates that the errors observed by validation, are not dominated by errors due to adjacency effects, or that the points affected by adjacency effects are not sufficiently statistically represented.

4 Evaluation of atmospheric correction

4.1 Considered AC algorithms

The following atmospheric correction algorithms have been considered:

1) **Polymer** (Steinmetz et al., 2011; Steinmetz and Ramon, 2018) is an iterative spectral matching algorithm, relying on a simple polynomial-like model for the atmospheric path reflectance, and a semi-analytic model for the water reflectance. It has been designed to work in presence of sun glint, and has been first applied to MERIS, then to various other sensors.
2) **C2RCC/C2X** (Brockmann et al., 2016; Doerffer and Schiller, 2007) use a neural network approach, trained on radiative transfer simulations. It has several similarities with Polymer: (1) it is a pixel-by-pixel algorithm, (2) it uses the full sensor spectrum for atmospheric correction, and (3) it relies on a model of reflectance for the water component.

3) **ACOLITE** (Vanhellemont, 2019; Vanhellemont and Ruddick, 2021) is an image-based algorithm which evaluates the aerosol properties in the NIR and SWIR. This evaluation is based on the dark spectrum fitting (DSF) which uses multiple dark targets in the subscene to construct a "dark spectrum" which is then propagated towards the visible bands.
4) **iCOR** (Keukelaere et al., 2018) is also image-based, but instead of relying on dark pixel assumption, it inverts the aerosol properties from the spectral variability within a land subset of the product (or can use the aerosol optical thickness as ancillary information). Therefore, iCOR cannot be applied to water-only products.

Due to the assumption of spatial homogeneity across the image, iCOR and Acolite are sensitive to small-scale atmospheric perturbations, like cloud edges, haze, or sun glint (this will be verified later in this report). To avoid outliers, these algorithms are often validated on cloud-free images (Pereira-Sandoval et al., 2019; Renosh et al., 2020).

All these algorithms can be applied to both Sentinel-2 MSI and Sentinel-3 OLCI. We note that at the time of writing D5.1 (Initial product evaluation), ACOLITE could not be applied to OLCI, but started supporting OLCI in 2021 (Vanhellemont and Ruddick, 2021), allowing for a more complete evaluation.

For MSI, all processing is performed at 60m spatial resolution.

4.2 Cloud masking

The IdePIX cloud mask (Wevers et al., 2021) was used as a common cloud mask across all processors. The following IdePix flags are considered for each sensor:

OLCI	MSI
IDEPIX_CLOUD	IDEPIX_CLOUD
IDEPIX_INVALID	IDEPIX_INVALID
IDEPIX_CLOUD_BUFFER	IDEPIX_CLOUD_AMBIGUOUS
IDEPIX_CLOUD_SHADOW	IDEPIX_CLOUD_BUFFER
IDEPIX_SNOW_ICE	IDEPIX_VEG_RISK
	IDEPIX_CLOUD_SHADOW
	IDEPIX_SNOW_ICE
	IDEPIX_MOUNTAIN_SHADOW
	IDEPIX_CIRRUS_SURE

4.3 Algorithms configurations

4.3.1 Polymer

Three configurations are considered for Polymer:

1) **"Polymer"**: the default Polymer configuration
2) **"Polymer_minabs2"**: the updated Polymer configuration for CERTO, as described in section 3.1.
3) **"Polymer_veg"**: the updated Polymer configuration for CERTO as per **"Polymer_minabs2"**, also including the vegetation adjacency correction described in section 3.3.3.

The masking expression (which identifies valid pixels) associated with Polymer outputs is:

```
(bitmask & 1023 = 0) & (rho_w < 0.12 at all spectral bands)
```

4.3.2 C2RCC/C2X

The default C2RCC configuration was used for processing OLCI products. For MSI, two different neural networks are considered: “C2RCC-Nets” and “C2X-COMPLEX-Nets”. We refer to these configurations as C2RCC and C2X in the rest of this document.

The masking expression (which identifies valid pixels) associated with C2RCC for OLCI outputs is:

```
not (Rtosa_OOS and (conc_chl < 1.0))
& (not Rtosa_OOR)
& (not Rhow_OOR)
& (not Cloud_risk)
& (conc_chl > 0.01)
```

For MSI, the use of the quality flag “cloud_risk” leads to excessive loss of valid matchups, thus no pixel mask was used in addition to the cloud mask.

4.3.3 ACOLITE

ACOLITE v20221114 was applied to OLCI and MSI with its default parameters, thus using the Dark Spectrum Fitting method. No quality flag is associated with the level2 products, thus only the common cloud mask is used.

4.3.4 iCOR

iCOR v2.0 was used with its default configuration, including SIMEC activation (adjacency effect correction). No quality flag is associated with the level2 products, thus only the common cloud mask is used.

In addition, some scenes could not be processed with iCOR due to the incapacity of the algorithm to estimate aerosol optical thickness when no land pixel is available.

4.4 Validation using in-situ data

4.4.1 Data and method

A validation of MSI (Sentinel-2A and Sentinel-2B) and OLCI (Sentinel-3A and Sentinel-3B) was performed using the CERTO in-situ database and covering all 6 CERTO case study sites. This validation was initially conducted with the 2021 data campaigns only which were insufficient to obtain conclusive results (insufficient number of satellite matchups). Therefore, the analysis was delayed until the in-situ data from 2022, and the historical data, were available (only in December 2022 resulting in the delay to this Deliverable). The results presented in this section are based on this update which resulted in a major increase of the number of matchups. The locations of the in-situ measurements are shown for each case study site in Figure 20. Among the total number of matchups included in section 4.4.3 (Common Best Quality), the historical data represent almost half of the matchups (see Figure 21).

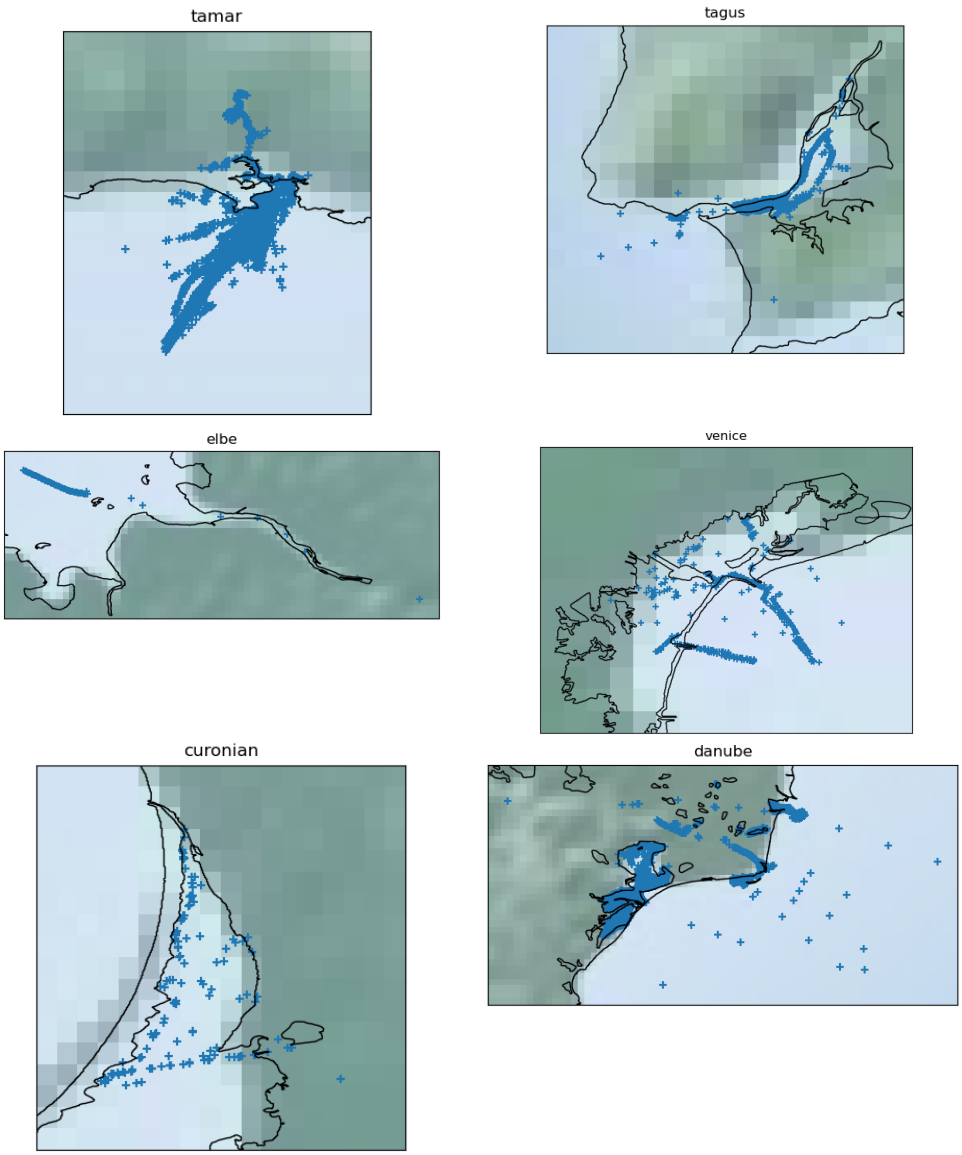

Figure 20: Location of the in-situ measurements for each case study site.

	Historic data	Campaigns	Total
OLCI	55	64	119
MSI	43	48	91

Figure 21: Number of historical and campaign matchups in CBQ mode (Common Best Quality)

For each possible satellite matchup, the closest in-situ measurement within **one hour** was selected, and the closest point of the satellite image was extracted. Each satellite matchup can be invalidated, either by the cloud mask which is common across all considered AC algorithm (see section 4.2) or by the quality flags provided by each algorithm (section 4.3).

The following statistical variables were then computed:

- Mean difference: $MD = \frac{1}{n}\sum \rho_{w,OLCI}(\lambda) - \rho_{w,insitu}(\lambda)$

- Mean absolute difference: $MAD = \frac{1}{n}\sum |\rho_{w,OLCI}(\lambda) - \rho_{w,insitu}(\lambda)|$
- Correlation coefficient of the regression

Two sets of validation results were considered, following the approach used in the Ocean Colour Climate Change Initiative (OC-CCI) (Müller et al., 2015):

- **Individual Best Quality** (IBQ): the flags were applied per-processor, leading to a different number of validation points for each processor.
- **Common Best Quality** (CBQ): the flags were shared, and only the **pixels valid for all processors** are considered. This configuration allows for an optimal comparison of the **statistical quantities** because the same matchups are considered.

Even though all AC processors (ACOLITE, iCOR, Polymer, C2RCC) are included in the IBQ validation (which is presented on section 4.4.2), iCOR failed to process some MSI scenes that can be processed with other processors because of its inability to estimate the aerosol optical thickness in absence of land pixels, even though the corresponding matchup areas are non-cloudy and with a clear atmosphere. Therefore, taking the common matchups across all AC algorithms (CBQ validation, presented on section 4.4.3) leads to a significant loss of matchups.

Bearing in mind that iCOR is also significantly more computationally intensive than the other processors, thus not as adequate as the other processors for inclusion in an operational processor, we chose to drop iCOR from the CBQ validation, which allowed a higher number of matchups (91 instead of 63 MSI matchups; for OLCI, the number of matchups does not change because iCOR does not fail on OLCI as it does on MSI).

In the two next sections, we present the results of validation in “Individual Best Quality” validation (section 4.4.2), in which the number of matchups differs across algorithms, then the results of validation in the “Common Best Quality” validation (section 4.4.3), in which only the common matchups are selected for all algorithms. Results are presented for OLCI, then MSI. Single plots are shown for each band (412, 490, 560 and 665 for OLCI; 443, 490, 560 and 665 for MSI) and each algorithm configuration, then the summary statistics are shown as a function of the wavelength to allow for a better comparison of the algorithm configurations.

4.4.2 Validation results – Individual Best Quality (IBQ)

4.4.2.1 OLCI

4.4.2.1.1 Validation

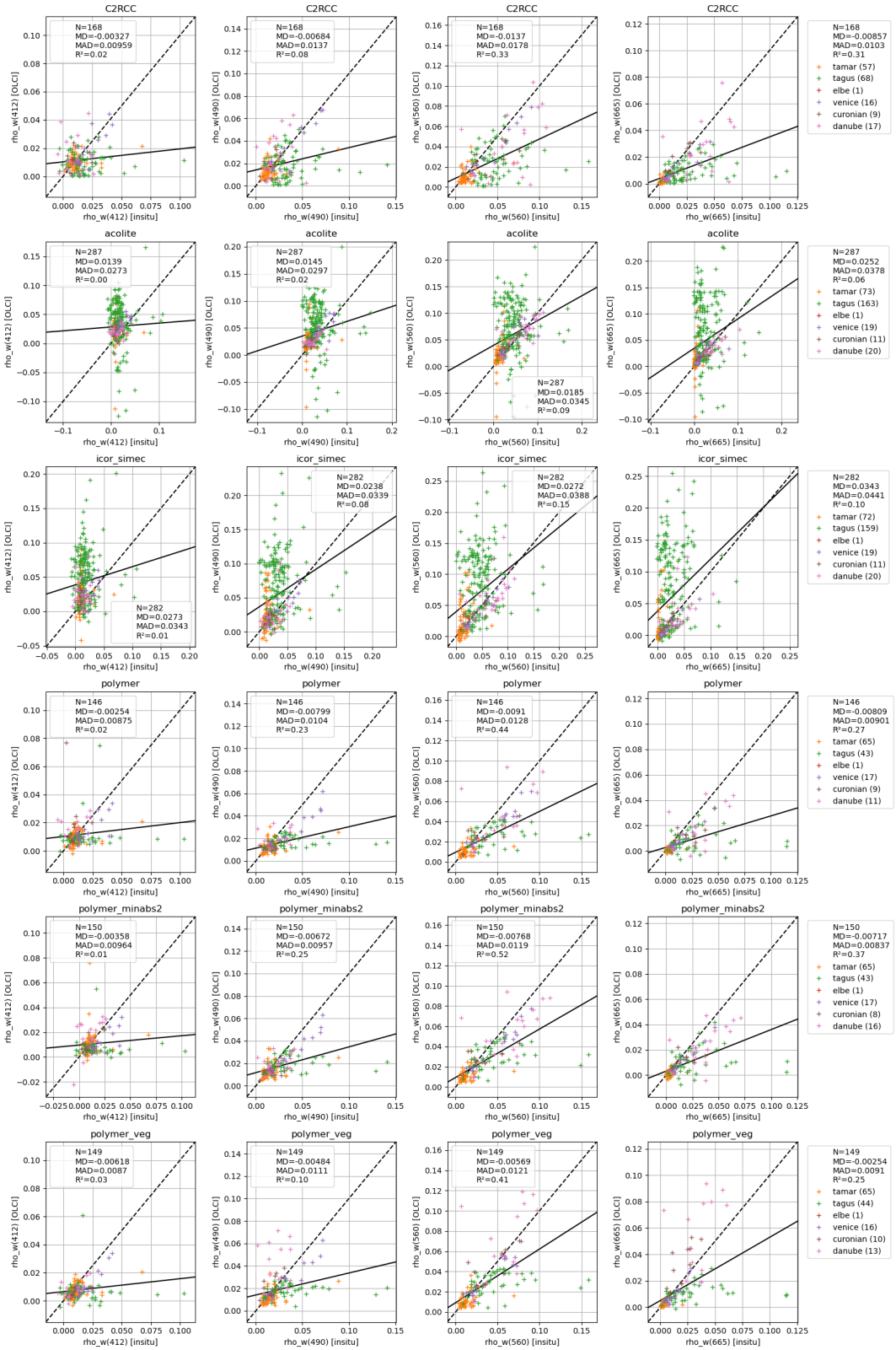

Figure 22: Validation plots for OLCI, in the Individual Best Quality mode. Each column corresponds to a spectral band from 412 to 665 nm, and each row to an AC algorithm.

4.4.2.1.2 Statistics

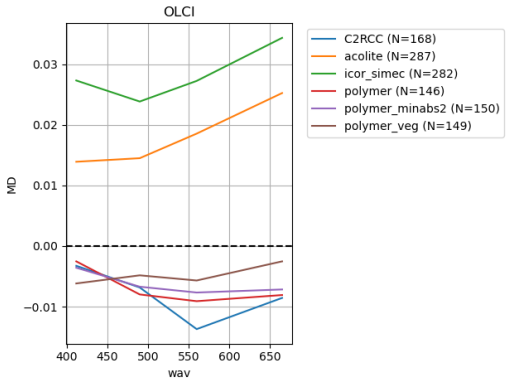

Figure 23: Representation of the mean deviation as a function of the wavelength, for each algorithm configuration.

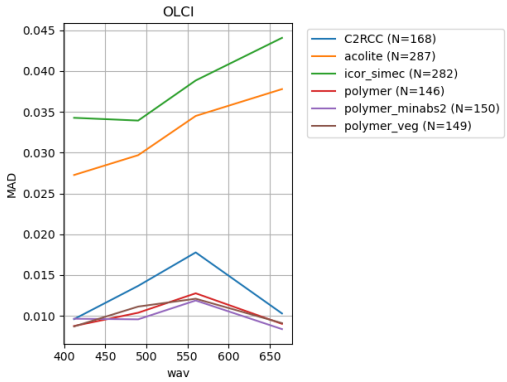

Figure 24: Representation of the mean absolute deviation as a function of the wavelength, for each algorithm configuration.

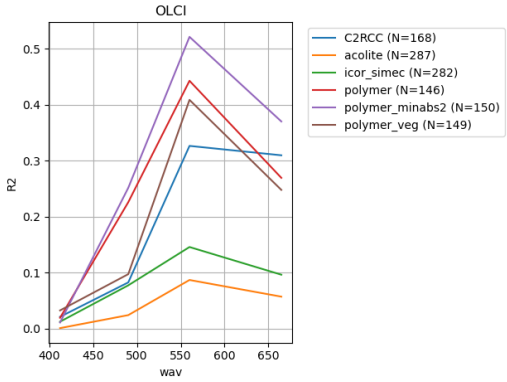

Figure 25: Representation of the correlation coefficient as a function of the wavelength, for each algorithm configuration.

4.4.2.2 MSI

4.4.2.2.1 Validation

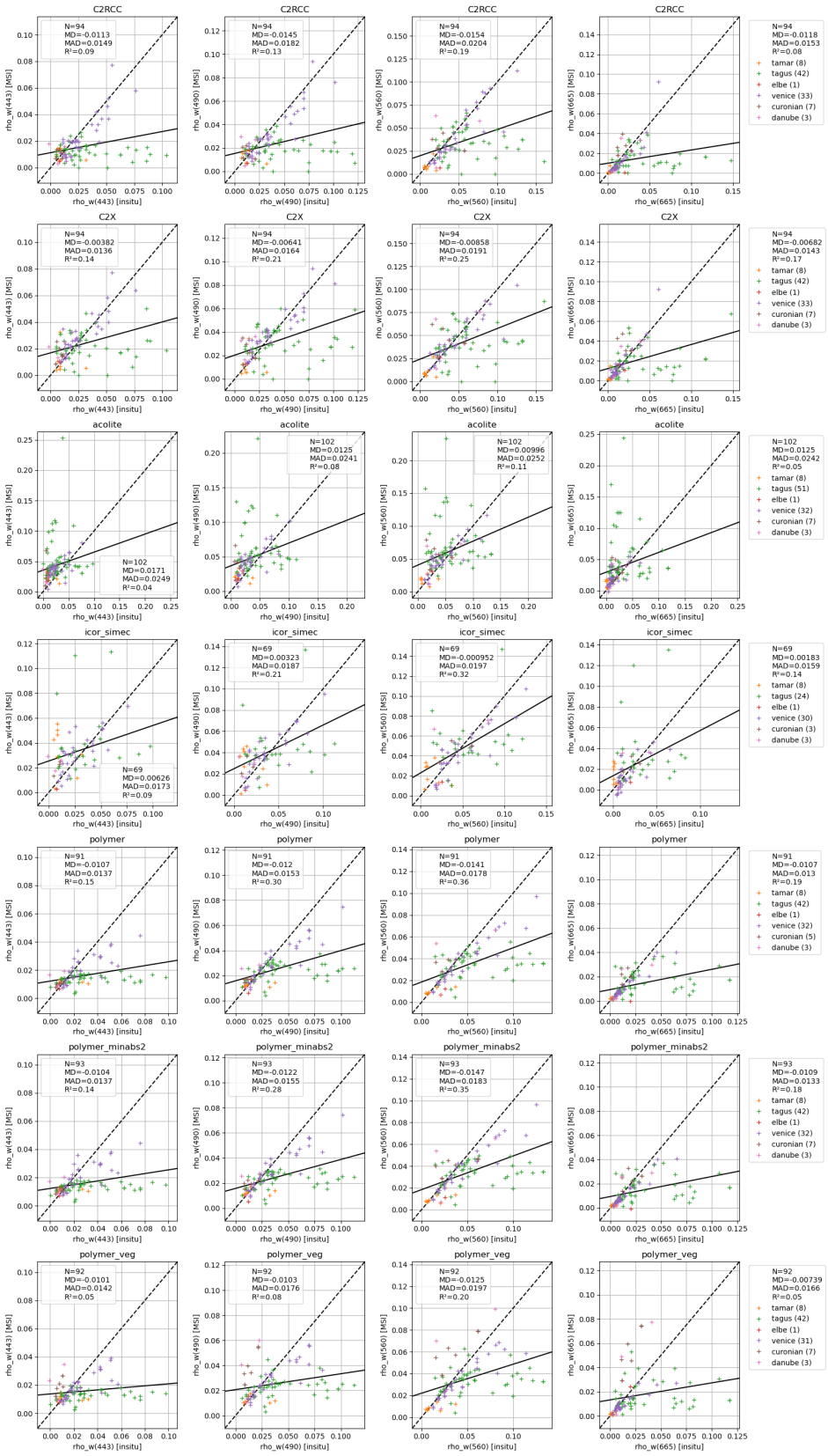

Figure 26: Validation plots for MSI, in the Individual Best Quality mode. Each column corresponds to a spectral band from 412 to 665 nm, and each row to an AC algorithm.

4.4.2.2.2 Statistics

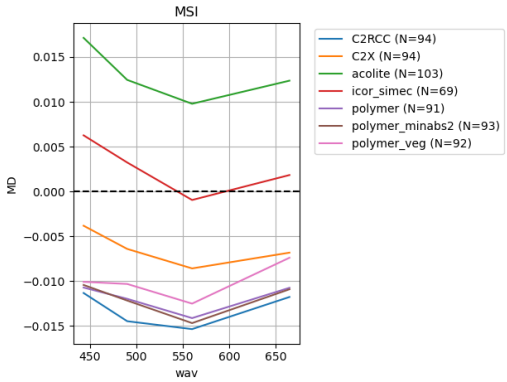

Figure 27: Representation of the mean deviation as a function of the wavelength, for each algorithm configuration.

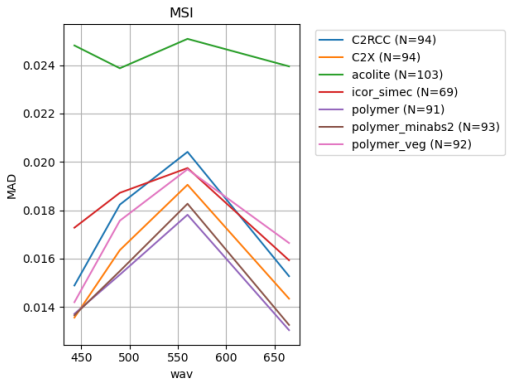

Figure 28: Representation of the mean absolute deviation as a function of the wavelength, for each algorithm configuration.

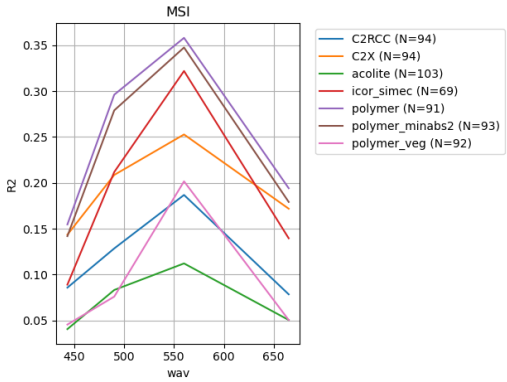

Figure 29: Representation of the correlation coefficient as a function of the wavelength, for each algorithm configuration.

4.4.3 Validation results – Common Best Quality (CBQ)

4.4.3.1 OLCI

4.4.3.1.1 Validation

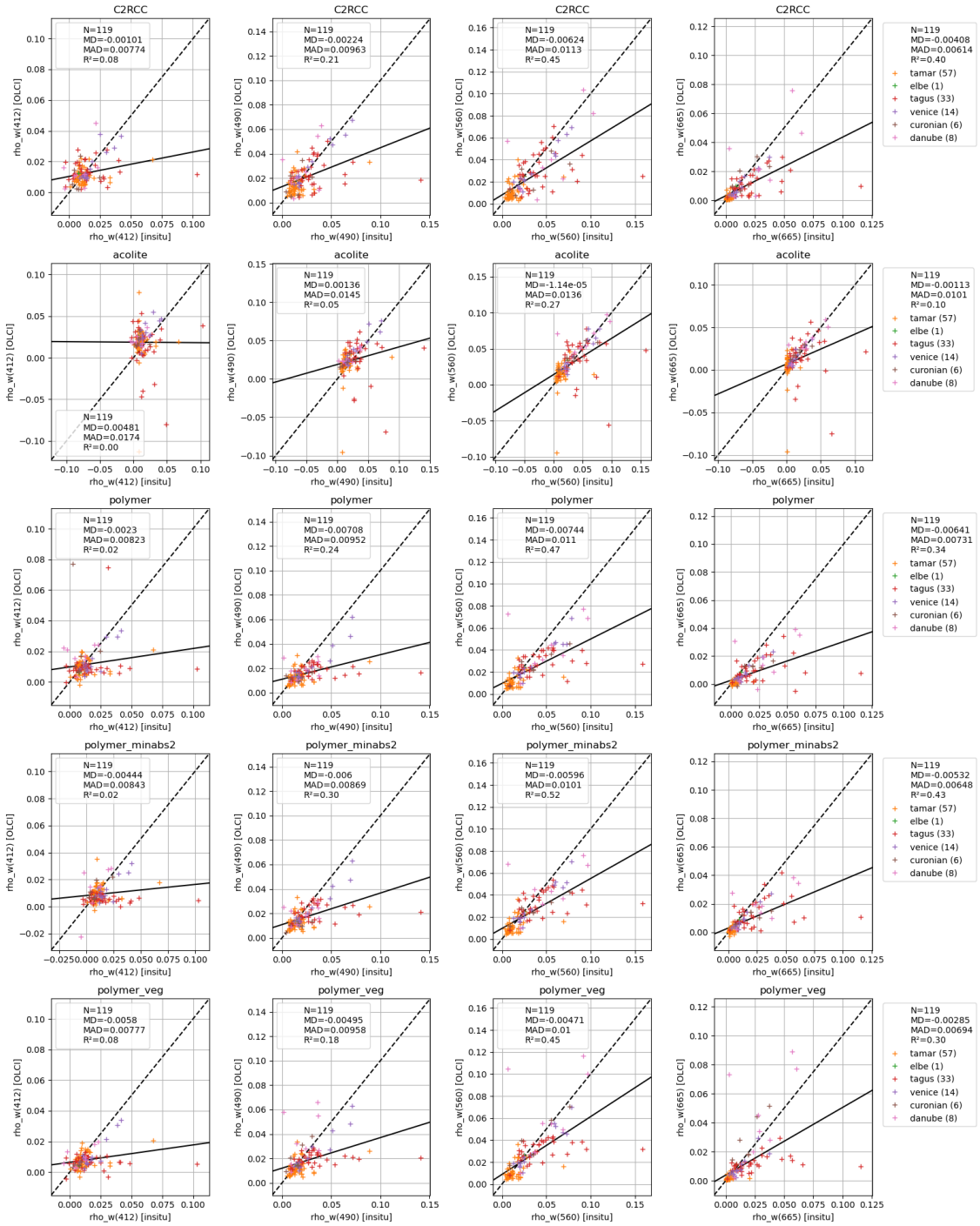

Figure 30: Validation plots for OLCI, in the Common Best Quality mode. Each column corresponds to a spectral band from 412 to 665 nm, and each row to an AC algorithm.

4.4.3.1.2 Statistics

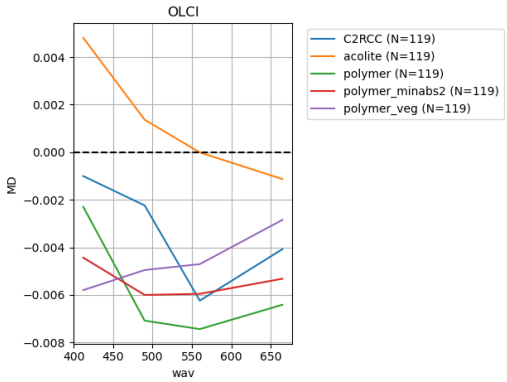

Figure 31: Representation of the mean deviation as a function of the wavelength, for each algorithm configuration.

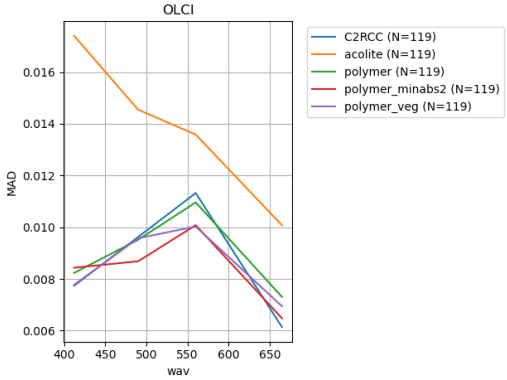

Figure 32: Representation of the mean absolute deviation as a function of the wavelength, for each algorithm configuration.

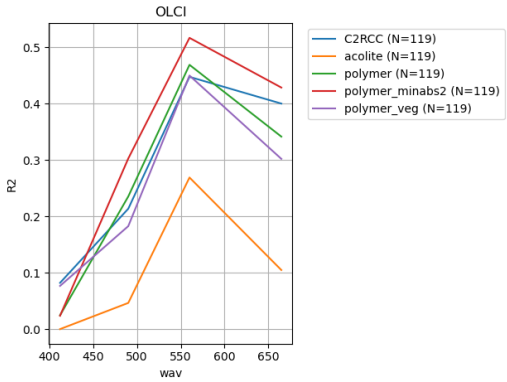

Figure 33: Representation of the correlation coefficient as a function of the wavelength, for each algorithm configuration.

4.4.3.2 MSI

4.4.3.2.1 Validation

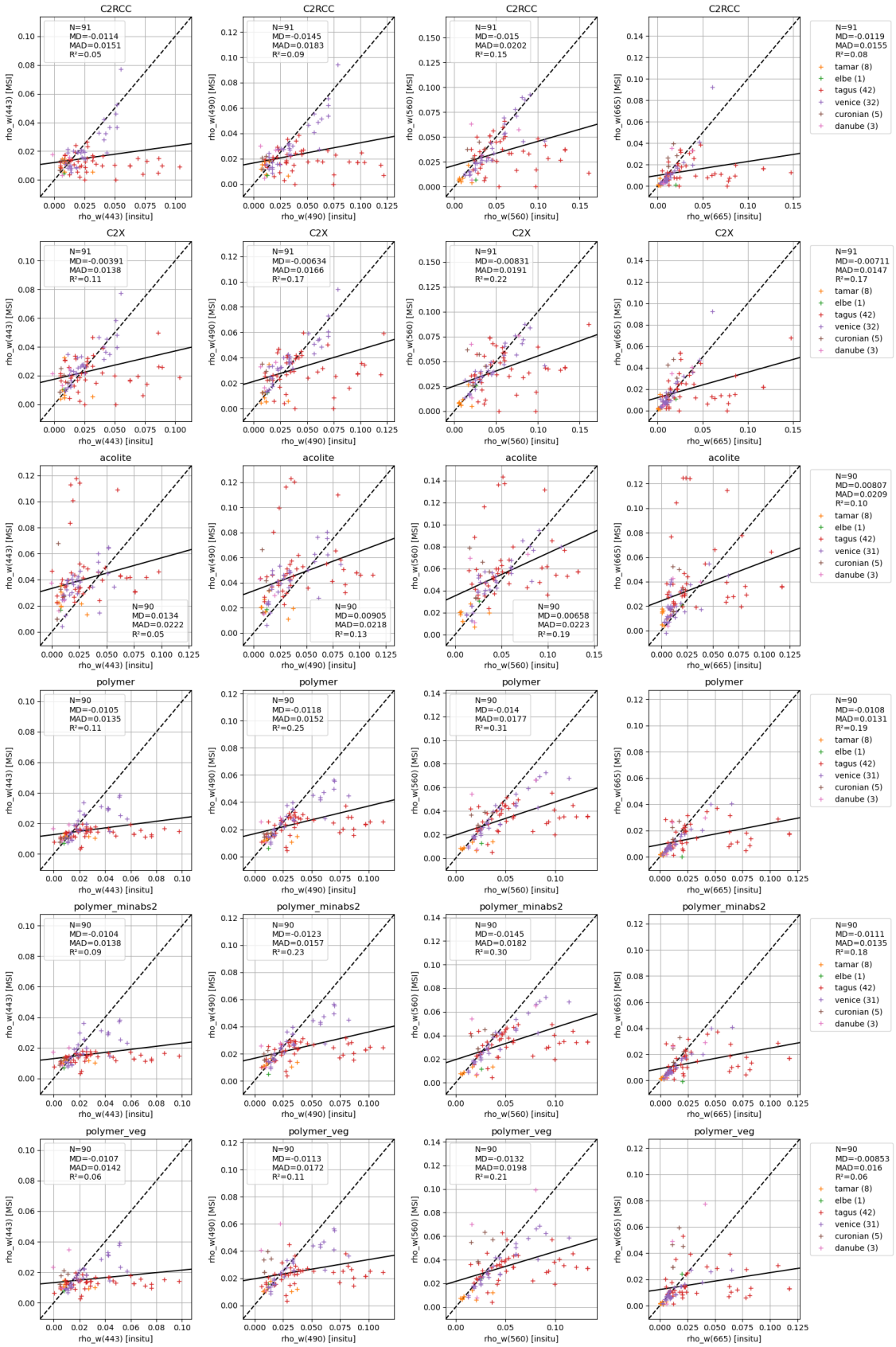

Figure 34: Validation plots for MSI, in the Common Best Quality mode. Each column corresponds to a spectral band from 412 to 665 nm, and each row to an AC algorithm.

4.4.3.2.2 Statistics

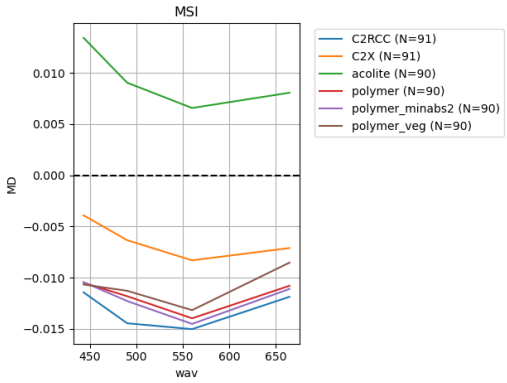

Figure 35: Representation of the mean deviation as a function of the wavelength, for each algorithm configuration.

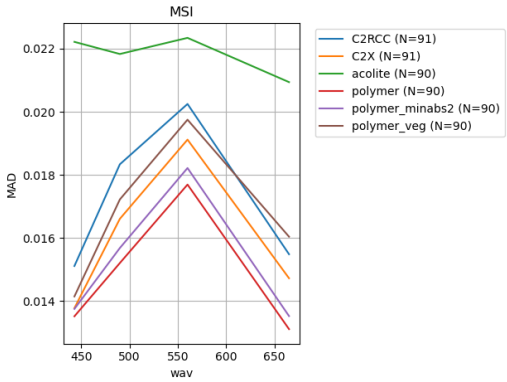

Figure 36: Representation of the mean absolute deviation as a function of the wavelength, for each algorithm configuration.

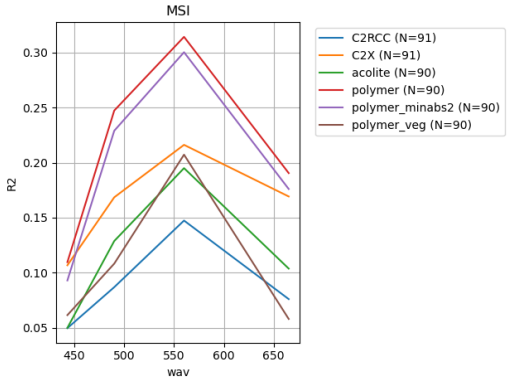

Figure 37: Representation of the correlation coefficient as a function of the wavelength, for each algorithm configuration.

4.4.4 Discussion

First, we can note that the **total number of matchups**, even though statistically significant, **does not equally cover all case study sites**. The Elbe estuary, which provided situations with the most turbid waters is, unfortunately, almost not covered by the matchups. Some cases of very turbid waters

(reflectance at 665 greater than 0.07) are seen for the Tagus estuary but are quite poorly retrieved by all AC algorithms and would require additional investigation.

The image-based algorithms tend to **over-estimate** the water reflectance. This is particularly true for OLCI IBQ, which seems to be affected by residual cloud contamination or glint contamination. In all cases (both IBQ and CBQ, and both for OLCI and MSI), we see on the statistics that the image-based algorithms (iCOR and ACOLITE) have a positive bias whereas the pixel-based (C2RCC and Polymer) algorithms have a negative bias. This can be explained by the fundamental atmospheric correction mechanisms:

- Since image-based algorithms assume spatial homogeneity of the atmosphere, any deviation from this hypothesis, thus inhomogeneity of the atmospheric properties, results in an over-estimation of the resulting water reflectance.
- Since pixel-based algorithms rely on a water reflectance model, they tend to compensate cases which deviate from this model by over-correcting the atmospheric component, thus providing under-estimation of the water reflectance. This is particularly true for bright waters as we can see on the individual plots.

For this reason, we expect image-based algorithms to better retrieve the reflectance of extremely turbid waters, in presence of a clear atmosphere, but these cases do not have a strong statistical representation in the present set of matchups.

We can see **relatively uniform performance** of the various configurations of the Polymer algorithm. The version including vegetation adjacency correction (polymer_veg) shows slightly less bias in the red bands than the other two versions of Polymer (polymer and polymer_minabs2) but higher mean absolute deviation for MSI (not for OLCI). However, the mean bias should be taken with caution because of the large underestimates that appear for all AC processors for some cases over the Tagus estuary. The significant increase of the mean absolute deviation of polymer_veg on MSI argues against applying this correction in the CERTO prototype. As discussed in section 3.3.3, the correction for vegetation adjacency in Polymer is limited to the red and NIR bands, and this correction is much lower than the correction required for other AC algorithms which are more sensitive to adjacency effects. The validation results lead us to think that this correction introduces an overall degradation of the AC: it remains an optional feature of Polymer but is not recommended for systematic application.

The performance of polymer_minabs2, which includes the improvements for turbid waters described in section 3.1, shows a similar performance as the standard version of polymer, both for OLCI and MSI. Only a very slight reduction of the mean absolute deviation is observed for OLCI (section 4.4.3.1.2). But as stated before, the in-situ matchups cover mostly non-extremely turbid waters (low number of matchups for the Elbe estuary), in which case the improvements of polymer_minabs2 are mostly expected to apply. The associated improvements will be discussed in next section (4.5).

For OLCI, polymer_minabs2 shows a slightly reduced mean absolute deviation compared to C2RCC (section 4.4.3.1.2), which is a sign of better precision. For MSI, a significant reduction of the mean absolute deviation is observed for C2X compared to C2RCC. Polymer/polymer_minabs2 show the lowest mean absolute deviation. We recall that C2X is not available for OLCI. C2X shows the lowest bias over MSI, but again the bias here should be taken with caution.

From these observations, **the best performing configuration is judged to be polymer_minabs2**, recalling the matchups have a low coverage of the extremely turbid waters.

4.5 Product visualisation and scene characterisation

To complement the evaluation based on the validation using the CERTO database, a set of 12 satellite sample products processed by each AC algorithm were visualised: one for each of the 6 case study site and for each sensor (OLCI, MSI).

The products are displayed as RGB composites of water reflectance (respectively at 665, 560 and 443 nm) to allow for a “natural colour” interpretation, and to avoid too many figures, because 3 spectral bands are displayed at the same time. This visualisation is more qualitative than quantitative (absence of colour bar) but is complemented by other quantitative analysis methods.

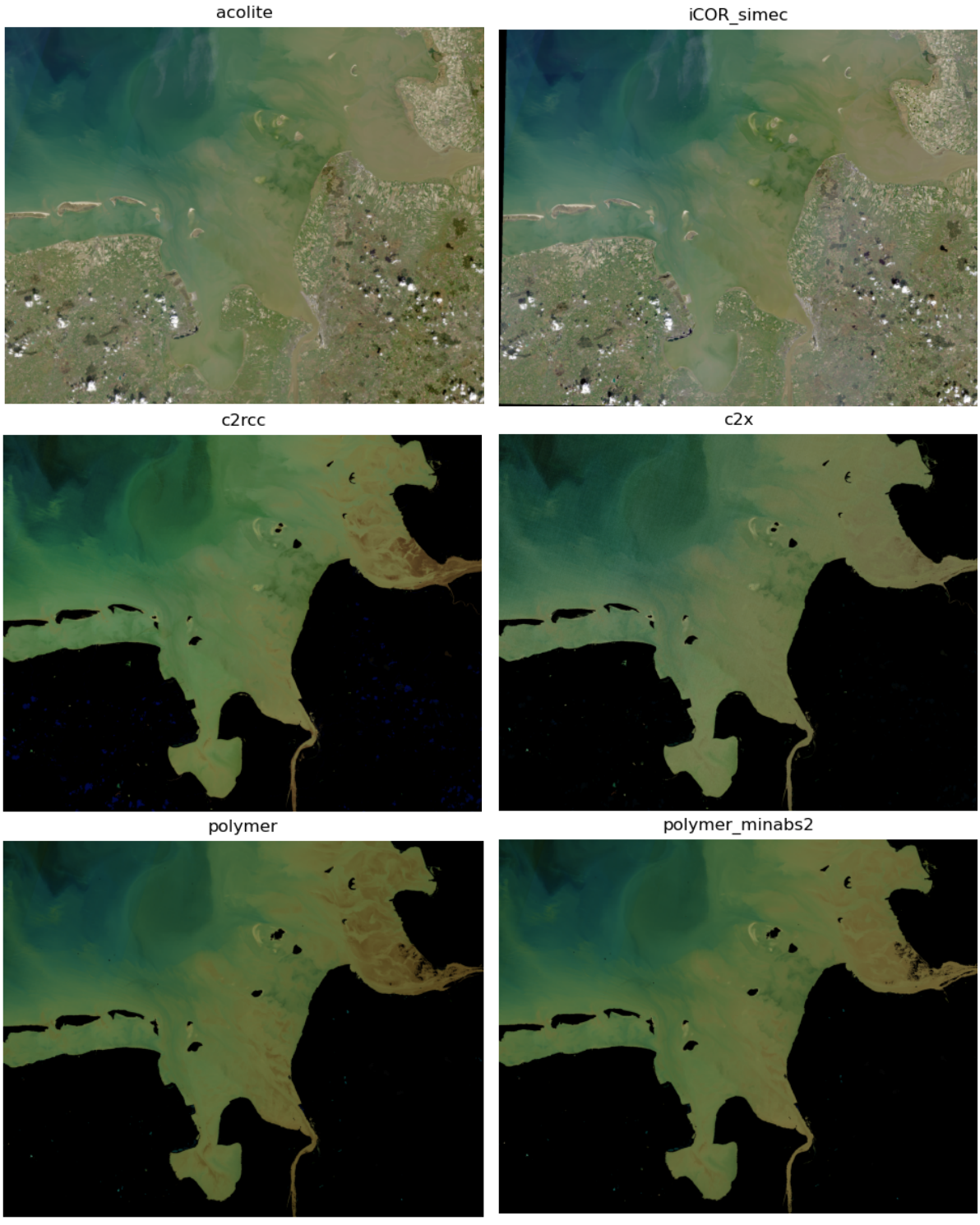

Figure 38: Sample products for the Elbe case study site (MSI: S2A_MSIL1C_20200407T104021_N0209_R008_T32UME_20200407T110356)

The full set of visualised products is provided in Annex 1 (section 8.1), which also includes the polymer products with vegetation adjacency correction for completeness. Some cases of algorithm instability appear with this configuration over the Elbe case (OLCI): see section 8.1.2.

All these scenes are mostly atmospherically clear, except the Tagus (MSI) [section 8.1.1.4]. In case of clear scene, the comparison of pixel-based algorithms with image-based algorithms is interesting since the image-based algorithms are by construction insensitive to the type of water, which is not the case for pixel-based algorithms. Thus, the image-based algorithm, for example ACOLITE, can be chosen as a reference. This allows, for example, assessment of the quality of the water reflectance at 865nm retrieved by Polymer (see Figure 39).

By taking ACOLITE as a reference, we can verify that the polymer_minabs2 is more consistent with ACOLITE than polymer, thus improves the results over turbid waters. Density plots are shown in Figure 39 for three images containing bright waters (Elbe MSI, Elbe OLCI and Danube OLCI). The left column shows the results for the polymer configuration, and the right column corresponds to the Polymer_minabs2 configuration. Each plot shows the density plot between the water reflectance at 865 nm provided by Polymer and the water reflectance at 865 provided by ACOLITE. In these graphs, the points are frequently located under the diagonal (rho_w_polymer(865) $\leq$ rho_w_acolite(865)), either because ACOLITE overestimates the water reflectance due to inhomogeneous atmosphere or because Polymer underestimates the water reflectance due to the difficulty to process extremely turbid waters. We can see that the polymer results are significantly underestimated for very turbid waters (rho_w(865) > 0.01), but it is less the case for polymer_minabs2, in which case the points are much more closer to the diagonal. This is a clear sign of the improvement of the Polymer_minabs2 configuration compared to the standard version of Polymer.

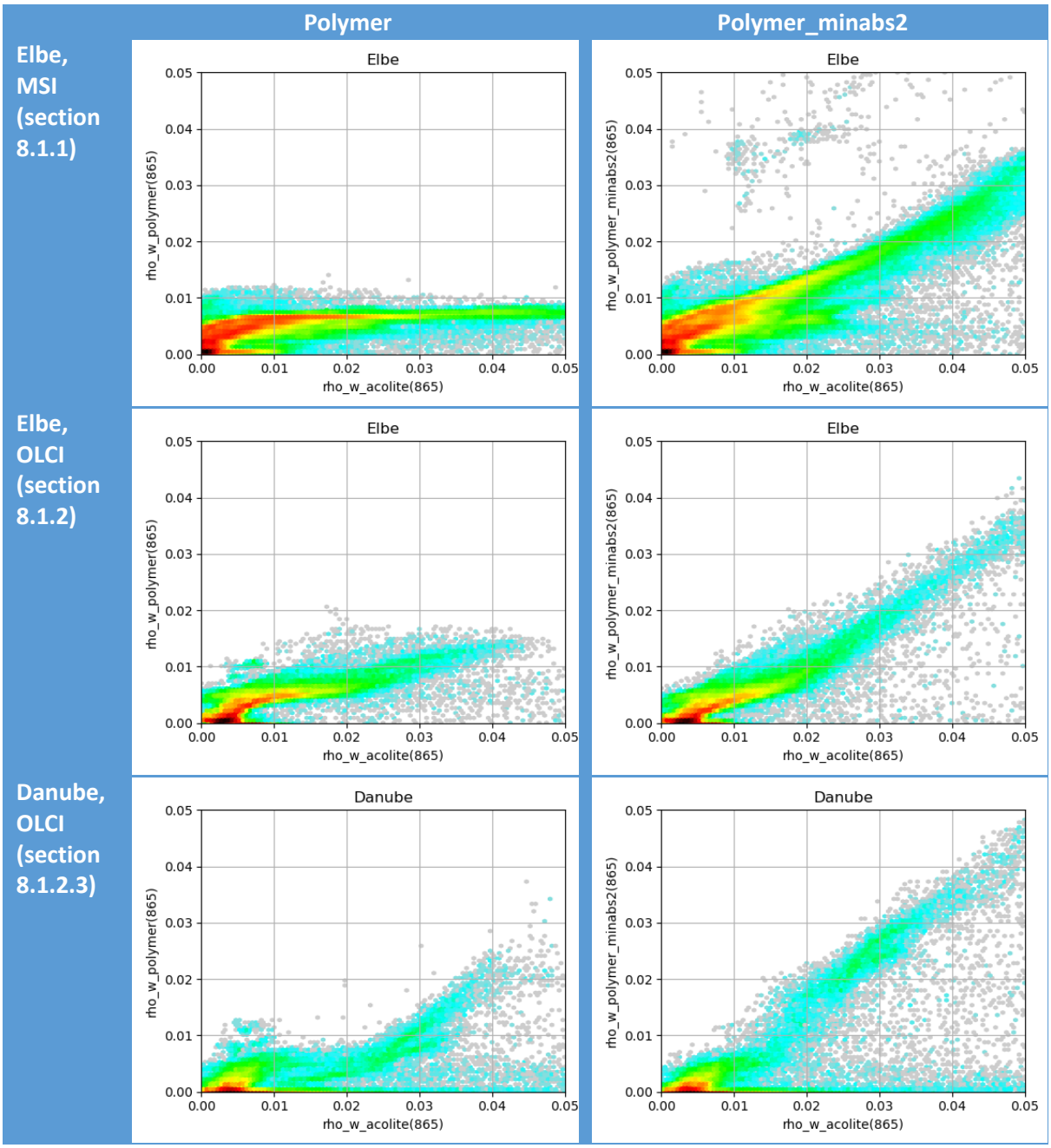

Figure 39: Comparison of the water reflectance retrieved by polymer (standard polymer on the left, polymer_minabs2 on the right), with the water reflectance at 865nm retrieved by ACOLITE, which is by construction insensitive to the type of water.

This improvement is also visible on the RGB composites because polymer shows dark spots over the most turbid parts of the Elbe estuary (Figure 38) which are clear underestimates because ACOLITE does not show such dark spots. In this example, polymer_minabs2 shows brighter reflectances, which is more consistent with ACOLITE. Similar observations can be made between C2RCC and C2X: the former, like polymer, shows a large underestimation of the reflectance of turbid waters, and C2X provides brighter, more consistent reflectances.

4.6 Optical water type analysis

An analysis was carried out, linked with WP4, to characterise the AC algorithms per Optical Water Type (OWT). As described in the previous section, the difference with ACOLITE is used because of the insensitivity of ACOLITE to the type of water. We can see, for all pixel-based algorithms, that the average difference with ACOLITE increases with higher OWT numbers ($OWT \geq 10$). Alternating values are due to the construction of OWTs by clusters, which alternate between bright and darker waters.

For iCOR, this difference remains very consistent across all OWTs because iCOR shares the same image-based design as ACOLITE. Again, these plots show the improvement of the polymer_minabs2 configuration compared to the baseline polymer configuration, with lower differences with ACOLITE.

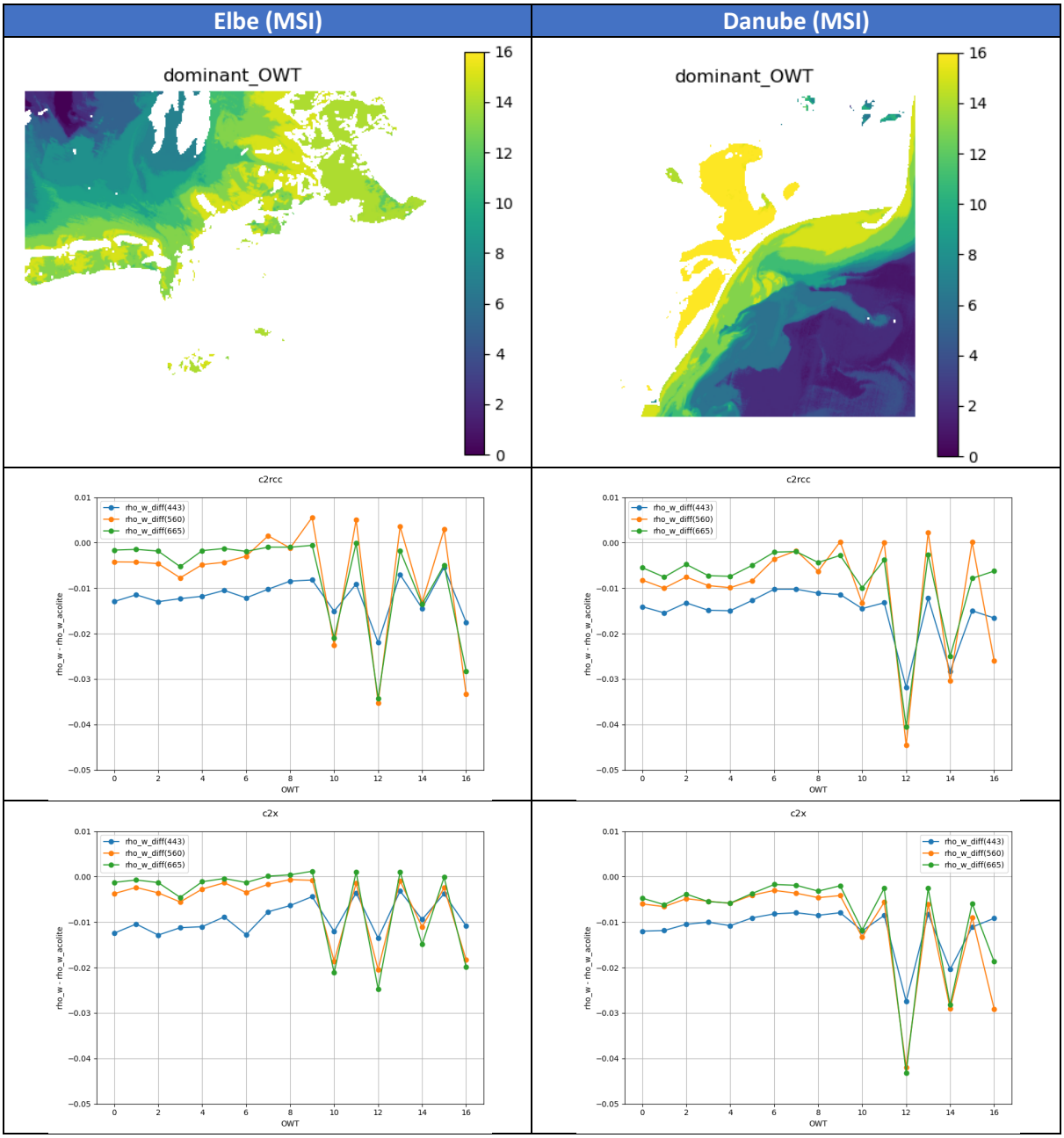

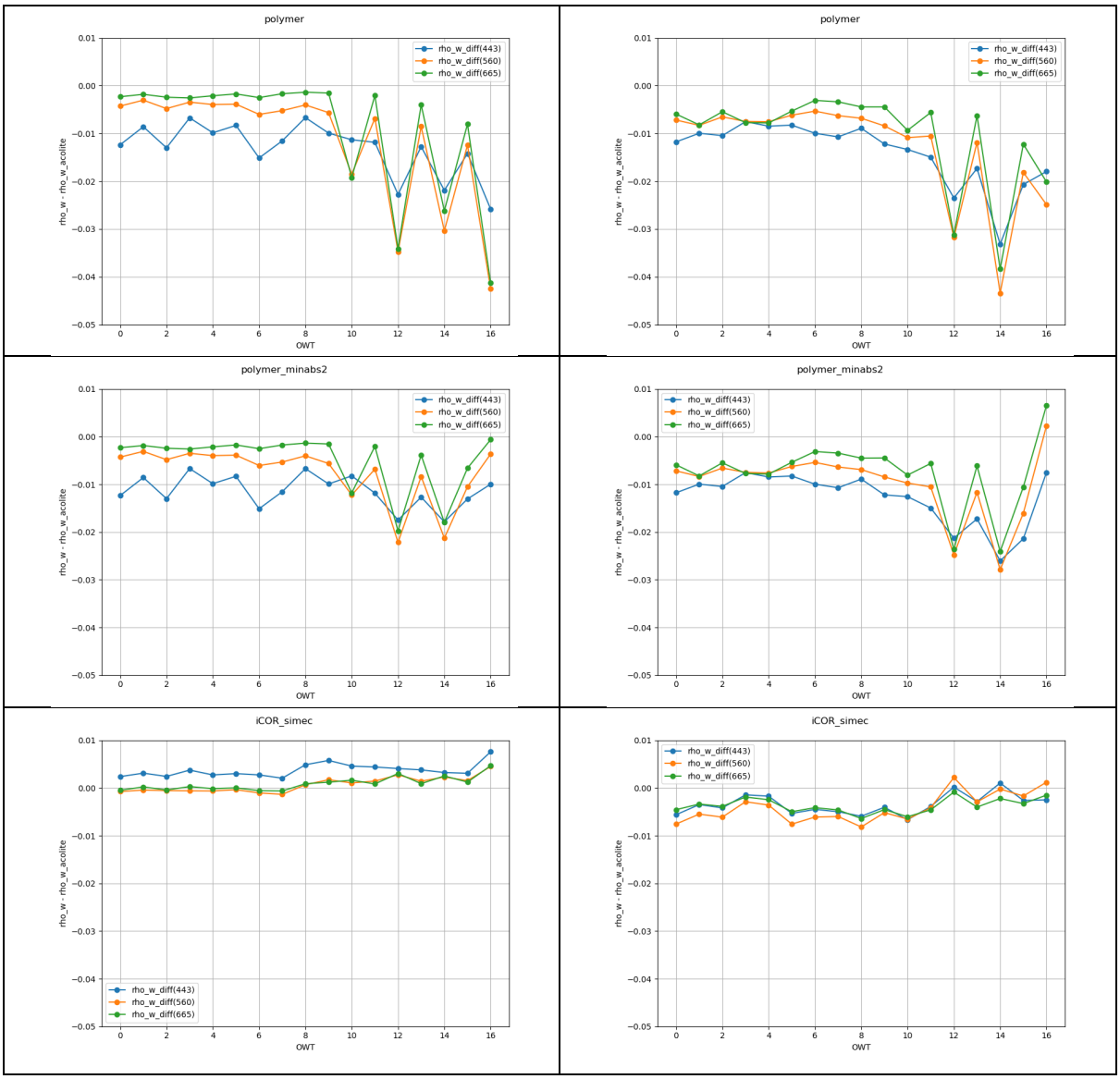

Figure 40: Average difference between the reflectance provided by different processors (C2RCC, C2X, Polymer, Polymer_minabs2 and iCOR) and ACOLITE, plotted as a function of the optical water type number from 0 to 16. The difference is shown at three bands (443, 560 and 665 nm). The map at the top shows the dominant optical water type for each pixel. Higher numbers of OWT corresponds to complex waters. The left column corresponds to the scene Elbe (MSI) and the right column corresponds to the scene Danube (MSI).

5 Merging approach

5.1 Motivation

Despite clear improvements over complex waters, an underestimation of the water reflectance is still observed in such cases. Thus, there is an interest to combine the results from two families of atmospheric correction algorithms:

1) Pixel-based algorithms, like Polymer, which are sensitive to highly reflective waters but highly capable of correcting for complex atmospheric cases

2) Image-based algorithms, like ACOLITE, which, by assuming spatial homogeneity of the atmosphere over a region of interest, are by construction insensitive to the type of water but highly sensitive to spatial variations of the atmosphere

We propose to follow a similar approach as in the Copernicus High-Resolution Ocean Colour Service, which involves merging the results from the C2RCC and ACOLITE algorithms, based on a green-NIR reflectance ratio provided by C2RCC. Here, the Polymer algorithm (with the minabs2 configuration) is merged with ACOLITE, based on the water reflectance at 865 nm provided by Polymer. It is important to use as a merging index a parameter that is the least sensitive to the atmospheric composition, thus derived from Polymer. As we have seen (section 4.5, Figure 39), the water reflectance at 865 nm, even though underestimated by polymer_minabs2 over very turbid waters, increases monotonically with the water reflectance at 865 nm provided by ACOLITE. This monotonicity is significantly improved from polymer to polymer_minabs2. This observation makes the water reflectance at 865 nm a good index for merging with ACOLITE.

Among the pixel-based algorithms, the Polymer algorithm is selected with the minabs2 configuration, for the following reasons:

- The other best-performing algorithm, C2X, is only provided for MSI, not OLCI.
- Polymer has received significant improvements for application to complex waters, as described in section 3.1.

5.2 Method

The water reflectance from Polymer, with the "minabs2" configuration ($\rho_{w,polymer}$) is merged with the water reflectance from ACOLITE ($\rho_{w,acolite}$), at each spectral band, based on a linear transition with a coefficient α which is determined from $\rho_{w,polymer}(865)$ and two thresholds, ρ_{min} and ρ_{max}:

$$\rho_w = \alpha \cdot \rho_{w,polymer} + (1-\alpha) \cdot \rho_{w,acolite}$$

$$\text{With } \begin{cases} \alpha = 1 \text{ if } \rho_{w,polymer}(865) < 0.005 = \rho_{min} \\ \alpha = 0 \text{ if } \rho_{w,polymer}(865) > 0.015 = \rho_{max} \\ otherwise\ \alpha = \frac{\rho_{max} - \rho_{w,polymer}(865)}{\rho_{max} - \rho_{min}} \end{cases}$$

This method allows for a smooth transition from Polymer to ACOLITE without pixel-to-pixel gaps on the resulting images.

Since ACOLITE cannot process sun glint contaminated areas (unlike Polymer), the ACOLITE products are masked for sun glint with $\rho_{gli} < 0.01$, where ρ_{gli} is the sun glint reflectance predicted from the wind speed using Cox and Munk (1954), as implemented in the Polymer algorithm. Polymer is masked with its standard flags (see section 4.3.1). The area where Polymer and ACOLITE are blended ($0 < \alpha < 1$) are masked with both Polymer and ACOLITE masks.

5.3 Results

An example of merged product and the corresponding areas of algorithm blending is shown in Figure 41 for the Elbe estuary (MSI).

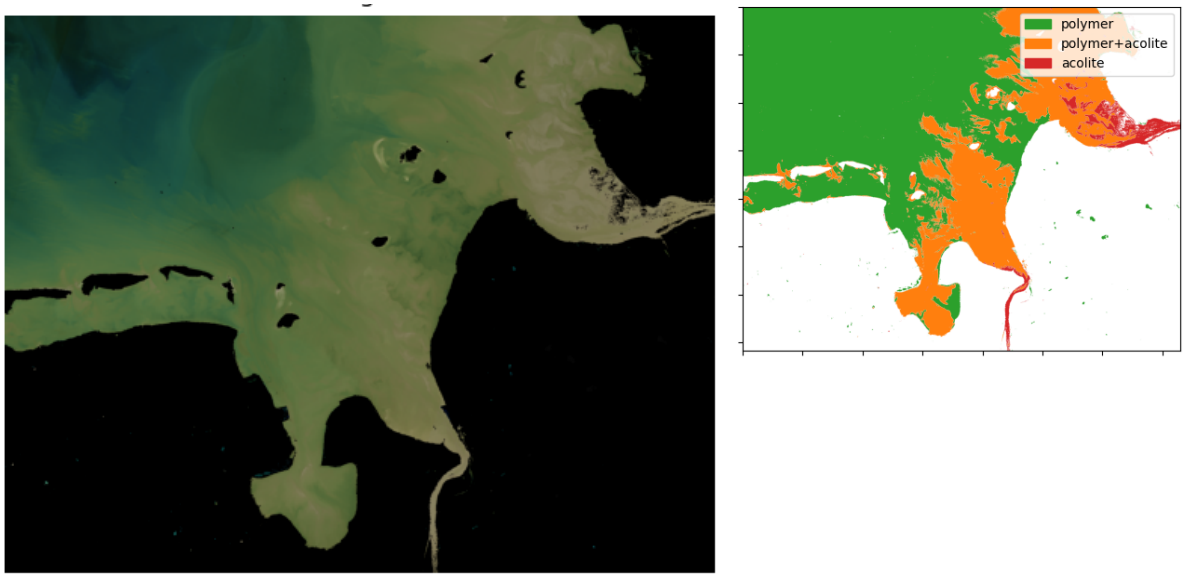

Figure 41: Example of merged product for the Elbe estuary scene (MSI). RGB composite of the water reflectance (left) and corresponding areas for algorithm blending (right: green=polymer, orange=polymer+acolite, red=acolite).

This example shows a good blending across both algorithms. The Elbe estuary shows high turbidity, where a consistent blending is crucial. The other case study sites show less turbidity, thus a lower occurrence of ACOLITE in the blending, except for the Razelm-Sinoe Lagoon (see section 8.2.1.3). The lagoon exhibits bright waters but there is a clear separation between the bright waters in the lagoon and the clearer waters of the Black Sea, thus no continuous blending from clear to bright waters.

The merged products for all test scenes are shown in the Annex 2 (section 8.2).

6 Conclusion

The different AC methods that have been considered in this study have their own strengths and weaknesses, and they are extremely challenged when being applied in the complex situations encountered in transitional waters, due the complexity of the water properties and the perturbating signals from the aerosols, the sun glint, the bathymetry effects, and the adjacency effects. An ideal AC algorithm would be insensitive to the water constituents, as is the case for the image-based algorithms such as ACOLITE, and would also be robust to the atmospheric and surface interaction, as is the case for pixel-based ocean-atmosphere coupled methods such as Polymer or the Neural Network methods. Even though a perfect algorithm still does not exist, significant progress has been made to identify the limits of each algorithm and push them further to improve the AC performance in various conditions.

Based on the rich database gathered in WP3 of CERTO, we have determined that the Polymer algorithm performed particularly well with the modifications implemented in CERTO; however, the ACOLITE algorithm is more appropriate when dealing with extremely turbid or bright waters. Therefore, a merging method was proposed for implementation in the CERTO prototype, as an attempt to combine the strengths of both algorithms.

7 References

Alikas, K., Ansko, I., Vabson, V., Ansper, A., Kangro, K., Uudeberg, K., Ligi, M., 2020. Consistency of Radiometric Satellite Data over Lakes and Coastal Waters with Local Field Measurements. Remote Sensing 12, 616. https://doi.org/10.3390/rs12040616

Antoine, D., Morel, A., 1999. A multiple scattering algorithm for atmospheric correction of remotely sensed ocean colour (MERIS instrument): Principle and implementation for atmospheres carrying various aerosols including absorbing ones. International Journal of Remote Sensing 20, 1875–1916. https://doi.org/10.1080/014311699212533

Ashphaq, M., Srivastava, P.K., Mitra, D., 2021. Review of near-shore satellite derived bathymetry: Classification and account of five decades of coastal bathymetry research. Journal of Ocean Engineering and Science 6, 340–359. https://doi.org/10.1016/j.joes.2021.02.006

Bi, S., Li, Y., Wang, Q., Lyu, H., Liu, G., Zheng, Z., Du, C., Mu, M., Xu, J., Lei, S., Miao, S., 2018. Inland Water Atmospheric Correction Based on Turbidity Classification Using OLCI and SLSTR Synergistic Observations. Remote Sensing 10. https://doi.org/10.3390/rs10071002

Brockmann, C., Doerffer, R., Peters, M., Stelzer, K., Embacher, S., Ruescas, Ana., 2016. Evolution of the C2RCC Neural Network for Sentinel 2 and 3 for the Retrieval of Ocean Colour Products in Normal and Extreme Optically Complex Waters.

Cox, C., Munk, W., 1954. Measurement of the Roughness of the Sea Surface from Photographs of the Sun's Glitter. J. Opt. Soc. Am. 44, 838. https://doi.org/10.1364/JOSA.44.000838

Doerffer, R., Schiller, H., 2007. The MERIS Case 2 water algorithm. International Journal of Remote Sensing 28, 517–535. https://doi.org/10.1080/01431160600821127

European Commission. Joint Research Centre., 2018. JRC sea level database: coastal hazards : the importance of the tides in the JRC storm surge alert systems (GDACS & SSCS). Publications Office, LU.

Fox, N., 2010. A guide to expression of uncertainty of measurements. QA4EO.

Gordon, H.R., Wang, M., 1994. Retrieval of water-leaving radiance and aerosol optical thickness over the oceans with SeaWiFS: a preliminary algorithm. Appl. Opt. 33, 443–452. https://doi.org/10.1364/AO.33.000443

GUM, 2008. Evaluation of measurement data — Guide to the expression of uncertainty in measurement.

Keukelaere, L.D., Sterckx, S., Adriaensen, S., Knaeps, E., Reusen, I., Giardino, C., Bresciani, M., Hunter, P., Neil, C., Zande, D.V. der, Vaiciute, D., 2018. Atmospheric correction of Landsat-8/OLI and Sentinel-2/MSI data using iCOR algorithm: validation for coastal and inland waters. European Journal of Remote Sensing 51, 525–542. https://doi.org/10.1080/22797254.2018.1457937

König, M., Hieronymi, M., Oppelt, N., 2019. Application of Sentinel-2 MSI in Arctic Research: Evaluating the Performance of Atmospheric Correction Approaches Over Arctic Sea Ice. Frontiers in Earth Science 7, 22. https://doi.org/10.3389/feart.2019.00022

Lee, Z., Carder, K.L., Mobley, C.D., Steward, R.G., Patch, J.S., 1999. Hyperspectral Remote Sensing for Shallow Waters. 2. Deriving Bottom Depths and Water Properties by Optimization. Appl. Opt. 38, 3831–3843. https://doi.org/10.1364/AO.38.003831

Lee, Z., Carder, K.L., Mobley, C.D., Steward, R.G., Patch, J.S., 1998. Hyperspectral Remote Sensing for Shallow Waters. I. A Semianalytical Model. Appl. Opt. 37, 6329–6338. https://doi.org/10.1364/AO.37.006329

Meerdink, S.K., Hook, S.J., Roberts, D.A., Abbott, E.A., 2019. The ECOSTRESS spectral library version 1.0. Remote Sensing of Environment 230, 111196. https://doi.org/10.1016/j.rse.2019.05.015

Müller, D., Krasemann, H., Brewin, R.J.W., Brockmann, C., Deschamps, P.-Y., Doerffer, R., Fomferra, N., Franz, B.A., Grant, M.G., Groom, S.B., Mélin, F., Platt, T., Regner, P., Sathyendranath, S., Steinmetz, F., Swinton, J., 2015. The Ocean Colour Climate Change Initiative: I. A methodology for assessing atmospheric correction processors based on in-situ measurements. Remote Sensing of Environment 162, 242–256. http://dx.doi.org/10.1016/j.rse.2013.11.026

Nelder, J.A., Mead, R., 1965. A Simplex Method for Function Minimization. The Computer Journal 7, 308–313. https://doi.org/10.1093/comjnl/7.4.308

Pan, Y., Bélanger, S., Huot, Y., 2022. Evaluation of Atmospheric Correction Algorithms over Lakes for High-Resolution Multispectral Imagery: Implications of Adjacency Effect. Remote Sensing 14, 2979. https://doi.org/10.3390/rs14132979

Park, Y.-J., Ruddick, K., 2005. Model of remote-sensing reflectance including bidirectional effects for case 1 and case 2 waters. Appl. Opt. 44, 1236–1249. https://doi.org/10.1364/AO.44.001236

Pereira-Sandoval, M., Ruescas, A., Urrego, P., Ruiz-Verdú, A., Delegido, J., Tenjo, C., Soria-Perpinyà, X., Vicente, E., Soria, J., Moreno, J., 2019. Evaluation of Atmospheric Correction Algorithms over Spanish Inland Waters for Sentinel-2 Multi Spectral Imagery Data. Remote Sensing 11, 1469. https://doi.org/10.3390/rs11121469

Renosh, P.R., Doxaran, D., Keukelaere, L.D., Gossn, J.I., 2020. Evaluation of Atmospheric Correction Algorithms for Sentinel-2-MSI and Sentinel-3-OLCI in Highly Turbid Estuarine Waters. Remote Sensing 12, 1285. https://doi.org/10.3390/rs12081285

Röttgers, R., DUPOUY, C., Taylor, B.B., Bracher, A., Wozniak, S.B., 2014. Mass-specific light absorption coefficients of natural aquatic particles in the near-infrared spectral region. Limnology and Oceanography 59, 1449–1460. https://doi.org/10.4319/lo.2014.59.5.1449

Santer, R., Schmechtig, C., 2000. Adjacency effects on water surfaces: primary scattering approximation and sensitivity study. Appl. Opt. 39, 361. https://doi.org/10.1364/AO.39.000361

Steinmetz, F., Deschamps, P.-Y., Ramon, D., 2011. Atmospheric correction in presence of sun glint: application to MERIS. Optics Express 19, 9783–9800. https://doi.org/10.1364/OE.19.009783

Steinmetz, F., Ramon, D., 2018. Sentinel-2 MSI and Sentinel-3 OLCI consistent ocean colour products using POLYMER, in: SPIE Asia-Pacific Remote Sensing Proceedings. https://doi.org/10.1117/12.2500232

Tan, J., Frouin, R., Ramon, D., Steinmetz, F., 2019. On the Adequacy of Representing Water Reflectance by Semi-Analytical Models in Ocean Color Remote Sensing. Remote Sensing 11, 2820. https://doi.org/10.3390/rs11232820

Vanhellemont, Q., 2019. Adaptation of the dark spectrum fitting atmospheric correction for aquatic applications of the Landsat and Sentinel-2 archives. Remote Sensing of Environment 225, 175–192. https://doi.org/10.1016/j.rse.2019.03.010

Vanhellemont, Q., Ruddick, K., 2021. Atmospheric correction of Sentinel-3/OLCI data for mapping of suspended particulate matter and chlorophyll-a concentration in Belgian turbid coastal waters. Remote Sensing of Environment 256, 112284. https://doi.org/10.1016/j.rse.2021.112284

Vanhellemont, Q., Ruddick, K., 2018. Atmospheric correction of metre-scale optical satellite data for inland and coastal water applications. Remote Sensing of Environment 216, 586–597. https://doi.org/10.1016/j.rse.2018.07.015

Wevers, J., Müller, D., Scholze, J., Kirches, G., Quast, R., Brockmann, C., 2021. IdePix for Sentinel-2 MSI Algorithm Theoretical Basis Document. https://doi.org/10.5281/ZENODO.5788067

Zaggia, L., Lorenzetti, G., Manfé, G., Scarpa, G.M., Molinaroli, E., Parnell, K.E., Rapaglia, J.P., Gionta, M., Soomere, T., 2017. Fast shoreline erosion induced by ship wakes in a coastal lagoon: Field evidence and remote sensing analysis. PLoS ONE 12, e0187210. https://doi.org/10.1371/journal.pone.0187210

8 Annex

8.1 Annex 1: Product visualisation

8.1.1 MSI

8.1.1.1 Elbe (MSI)

Product name: S2A_MSIL1C_20200407T104021_N0209_R008_T32UME_20200407T110356

Figure 42: RGB composite of the MSI sample scene over Elbe processed by acolite

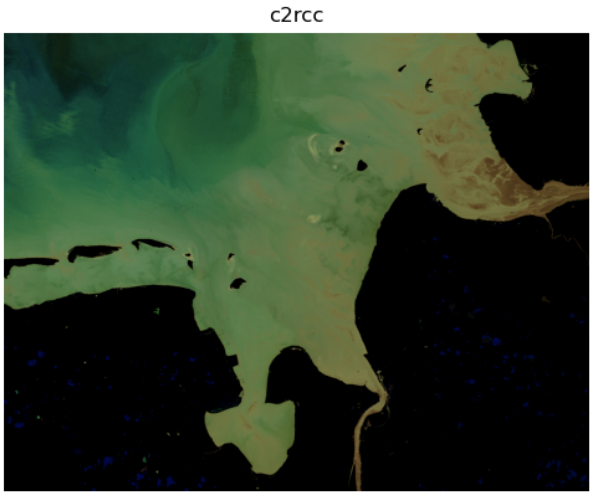

Figure 43: RGB composite of the MSI sample scene over Elbe processed by c2rcc

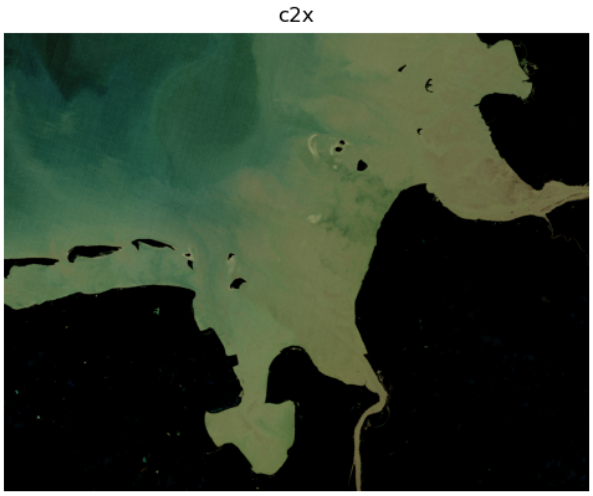

Figure 44: RGB composite of the MSI sample scene over Elbe processed by c2x

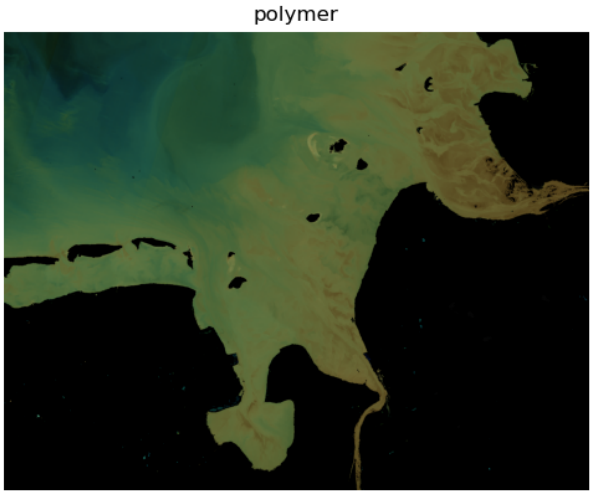

Figure 45: RGB composite of the MSI sample scene over Elbe processed by polymer

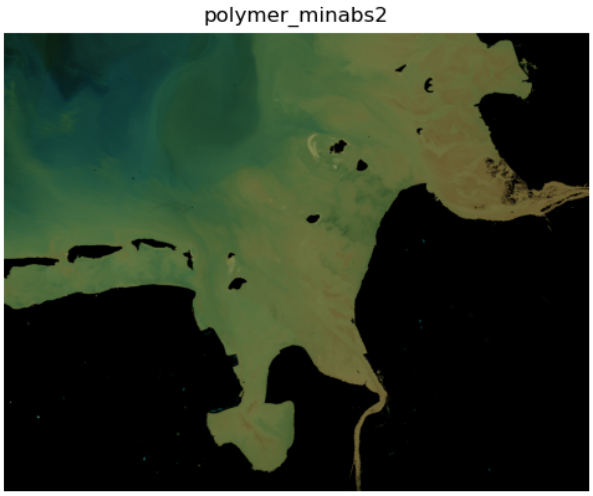

Figure 46: RGB composite of the MSI sample scene over Elbe processed by polymer_minabs2

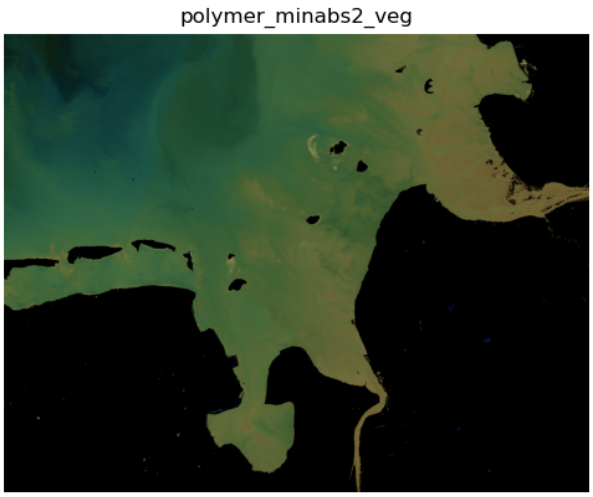

Figure 47: RGB composite of the MSI sample scene over Elbe processed by polymer_minabs2_veg

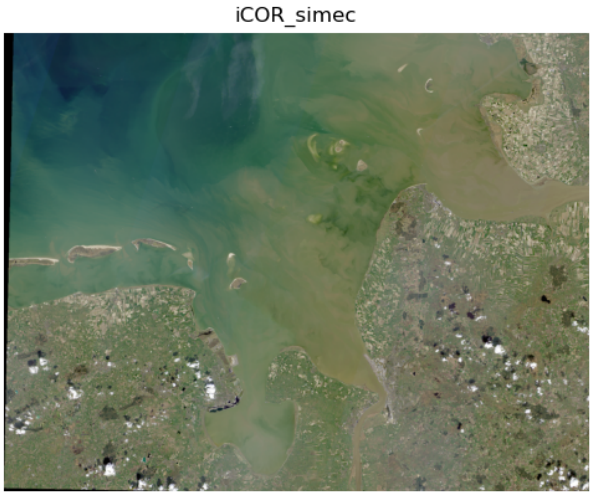

Figure 48: RGB composite of the MSI sample scene over Elbe processed by iCOR_simec

8.1.1.2 Curonian (MSI)

Product name: S2B_MSIL1C_20200410T100029_N0209_R122_T34UDF_20200410T125625

Figure 49: RGB composite of the MSI sample scene over Curonian processed by acolite

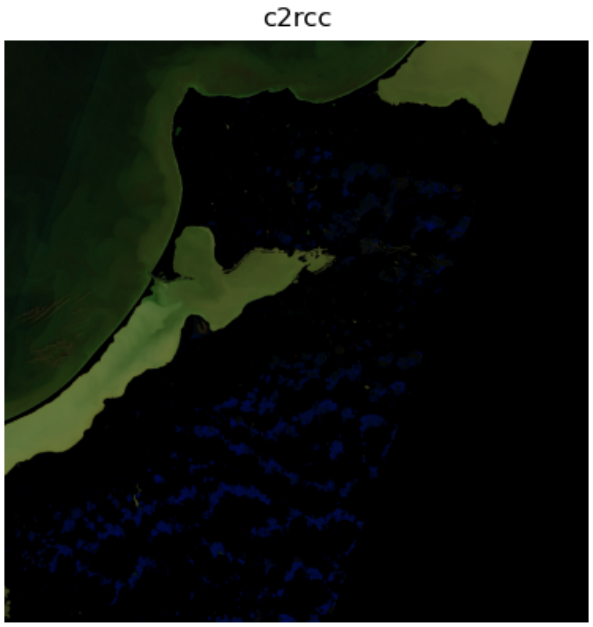

Figure 50: RGB composite of the MSI sample scene over Curonian processed by c2rcc

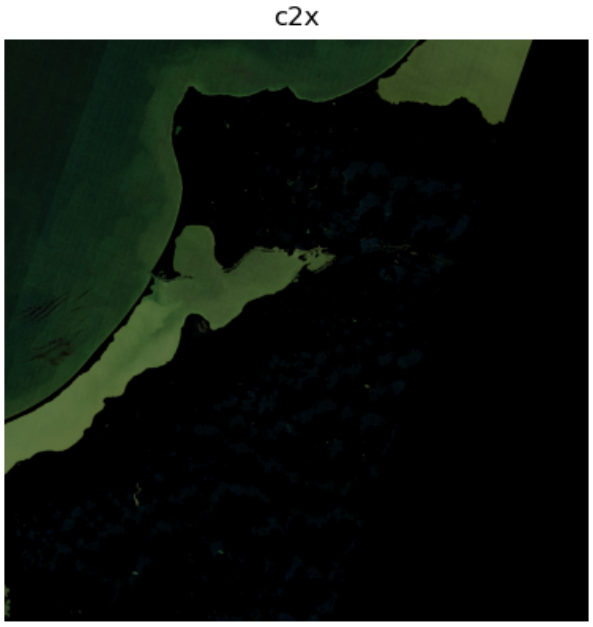

Figure 51: RGB composite of the MSI sample scene over Curonian processed by c2x

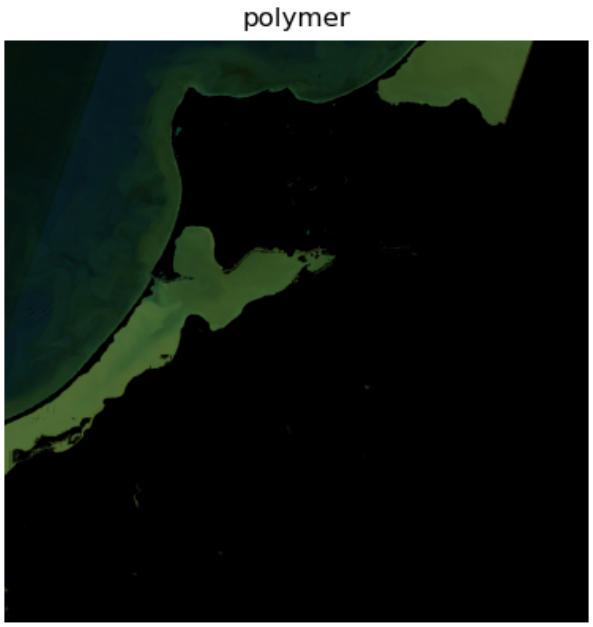

Figure 52: RGB composite of the MSI sample scene over Curonian processed by polymer

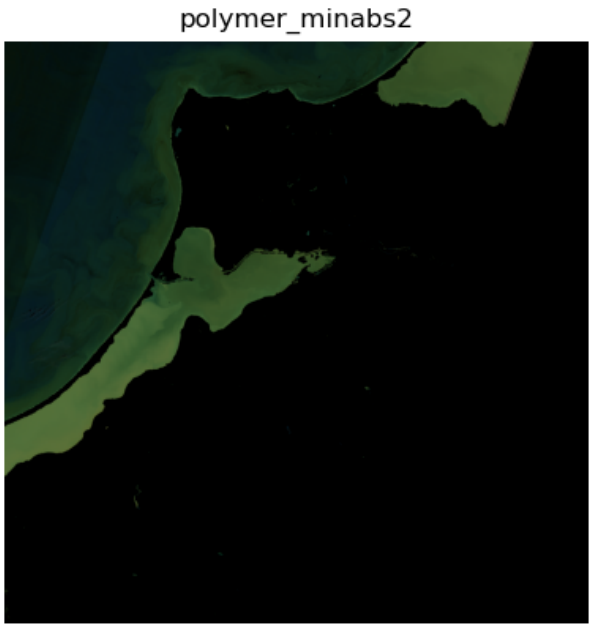

Figure 53: RGB composite of the MSI sample scene over Curonian processed by polymer_minabs2

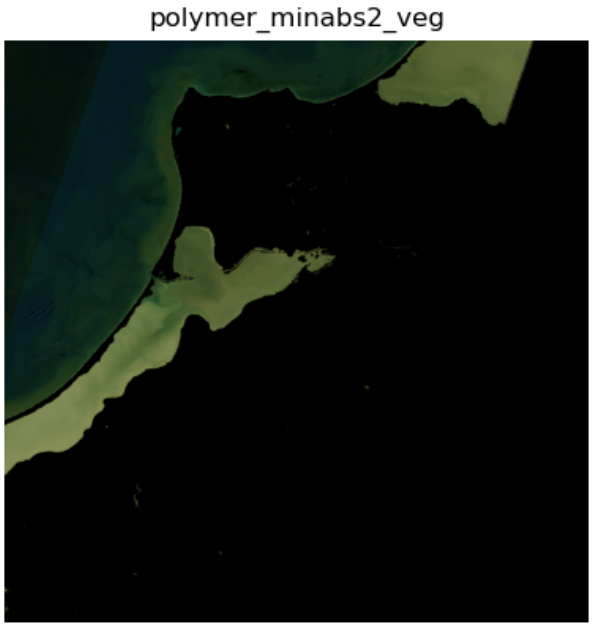

Figure 54: RGB composite of the MSI sample scene over Curonian processed by polymer_minabs2_veg

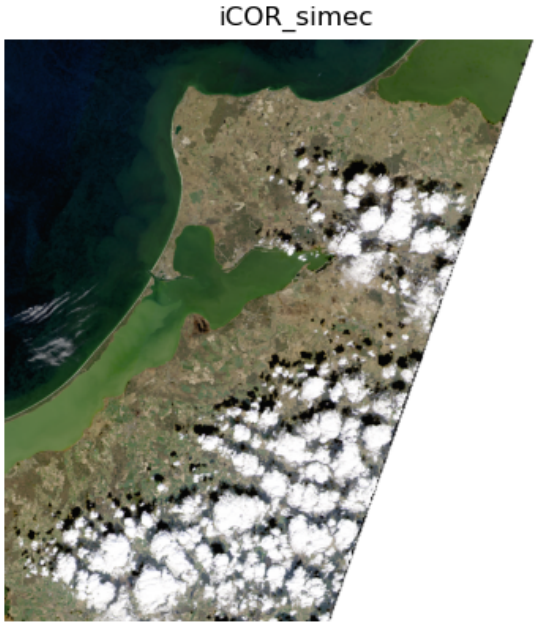

Figure 55: RGB composite of the MSI sample scene over Curonian processed by iCOR_simec

8.1.1.3 Danube (MSI)

Product name: S2A_MSIL1C_20200407T085551_N0209_R007_T35TPK_20200407T103455

Figure 56: RGB composite of the MSI sample scene over Danube processed by acolite

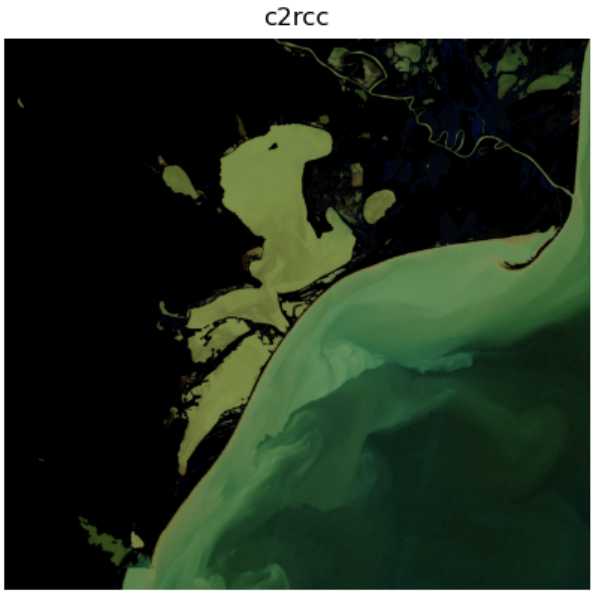

Figure 57: RGB composite of the MSI sample scene over Danube processed by c2rcc

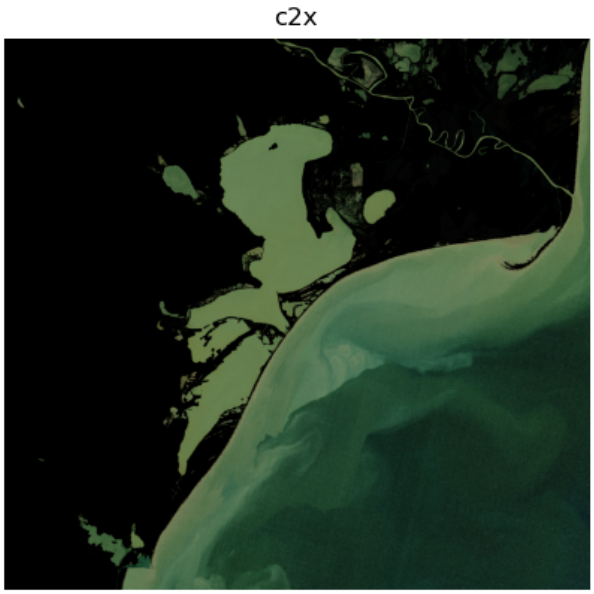

Figure 58: RGB composite of the MSI sample scene over Danube processed by c2x

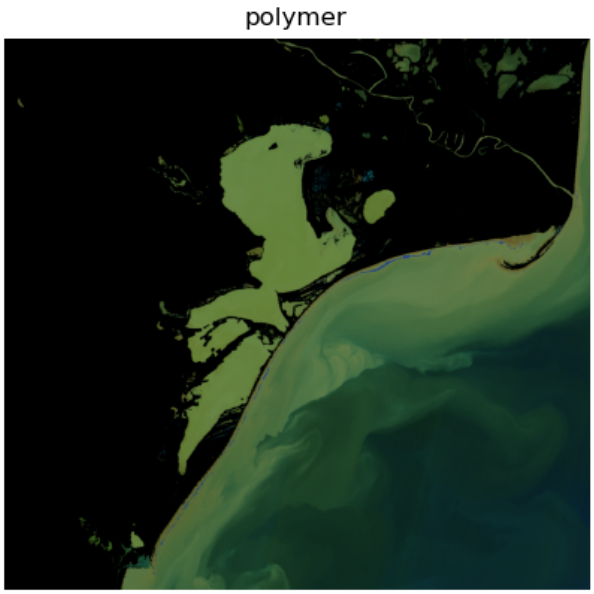

Figure 59: RGB composite of the MSI sample scene over Danube processed by polymer

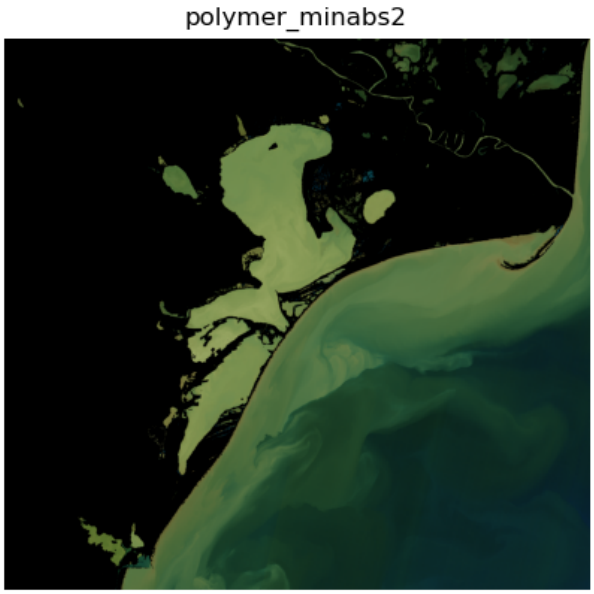

Figure 60: RGB composite of the MSI sample scene over Danube processed by polymer_minabs2

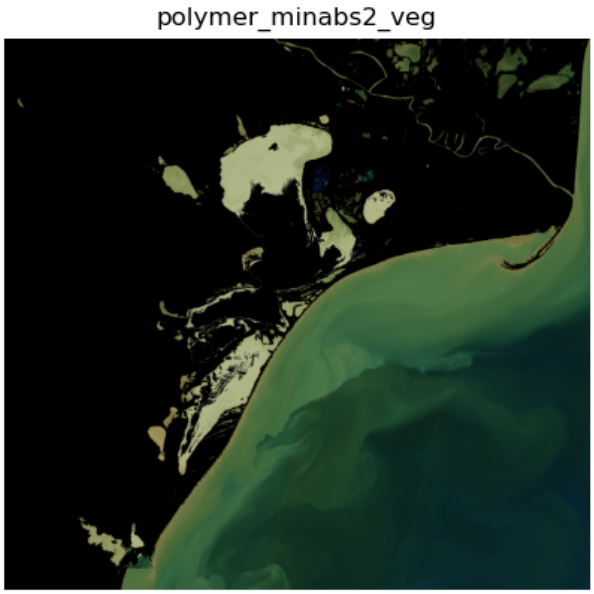

Figure 61: RGB composite of the MSI sample scene over Danube processed by polymer_minabs2_veg

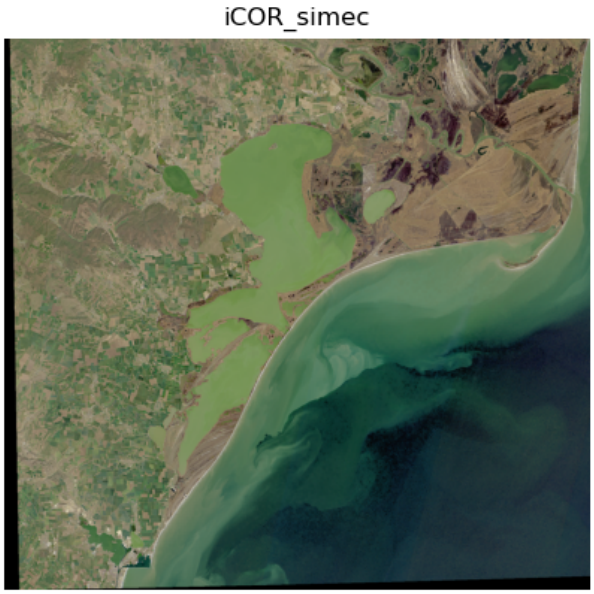

Figure 62: RGB composite of the MSI sample scene over Danube processed by iCOR_simec

8.1.1.4 Tagus (MSI)

Product name: S2B_MSIL1C_20200424T112109_N0209_R037_T29SMC_20200424T123554

Figure 63: RGB composite of the MSI sample scene over Tagus processed by acolite

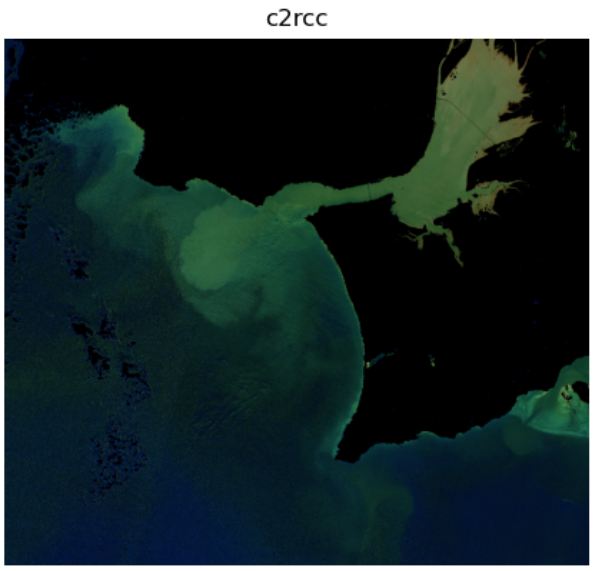

Figure 64: RGB composite of the MSI sample scene over Tagus processed by c2rcc

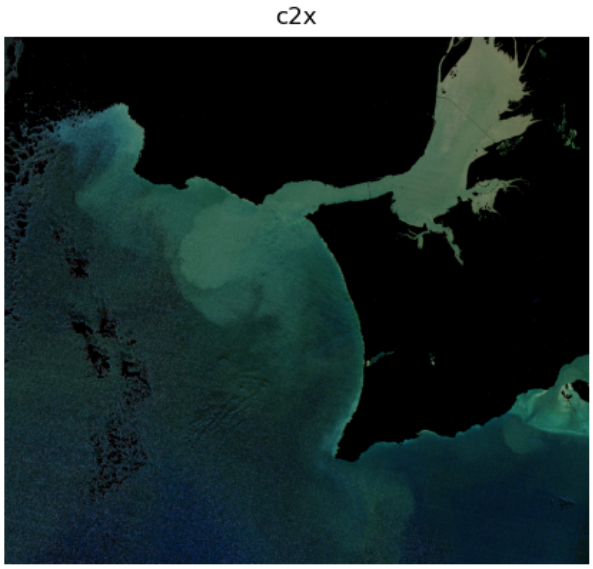

Figure 65: RGB composite of the MSI sample scene over Tagus processed by c2x

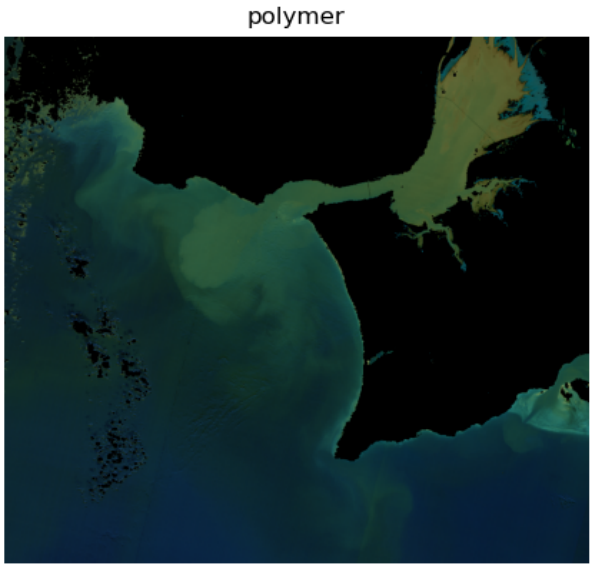

Figure 66: RGB composite of the MSI sample scene over Tagus processed by polymer

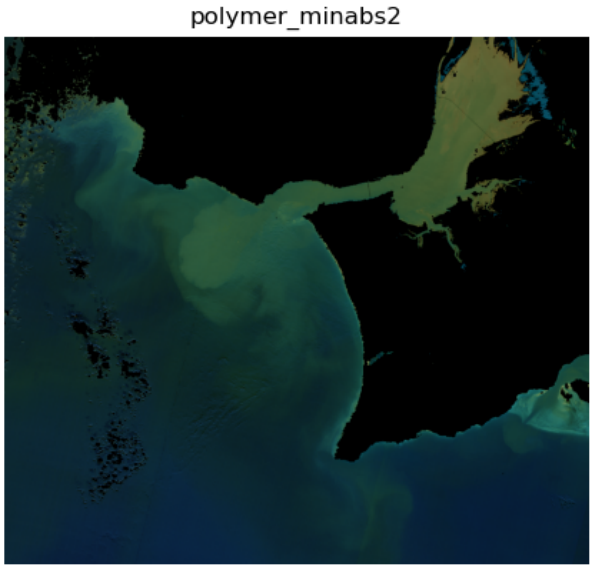

Figure 67: RGB composite of the MSI sample scene over Tagus processed by polymer_minabs2

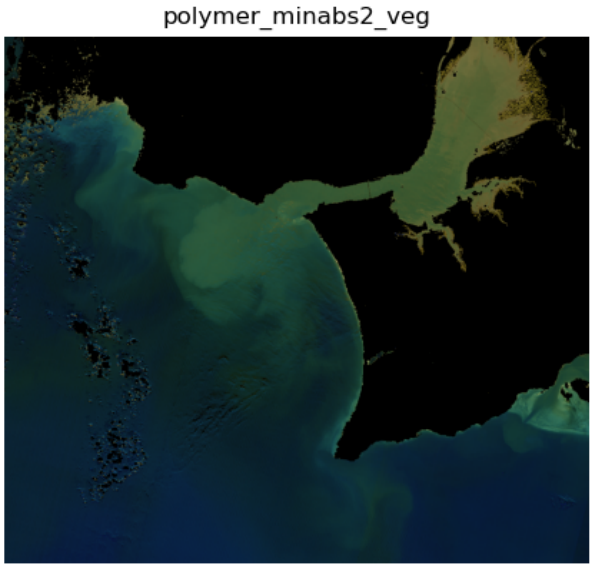

Figure 68: RGB composite of the MSI sample scene over Tagus processed by polymer_minabs2_veg

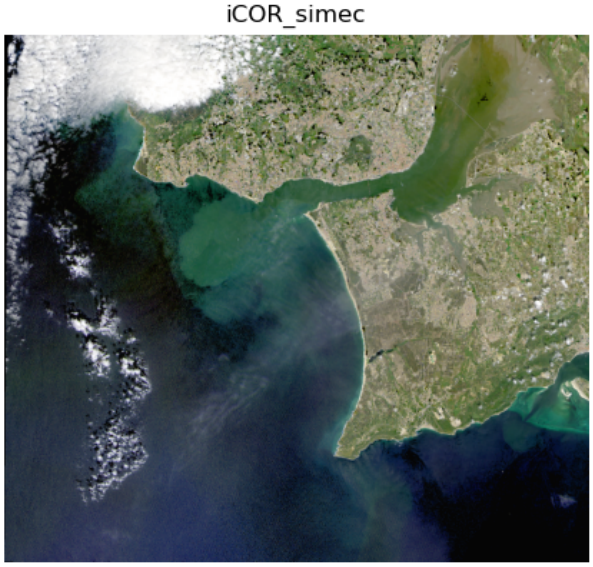

Figure 69: RGB composite of the MSI sample scene over Tagus processed by iCOR_simec

8.1.1.5 Tamar (MSI)

Product name: S2A_MSIL1C_20200409T112111_N0209_R037_T30UVA_20200409T132421

Figure 70: RGB composite of the MSI sample scene over Tamar processed by acolite

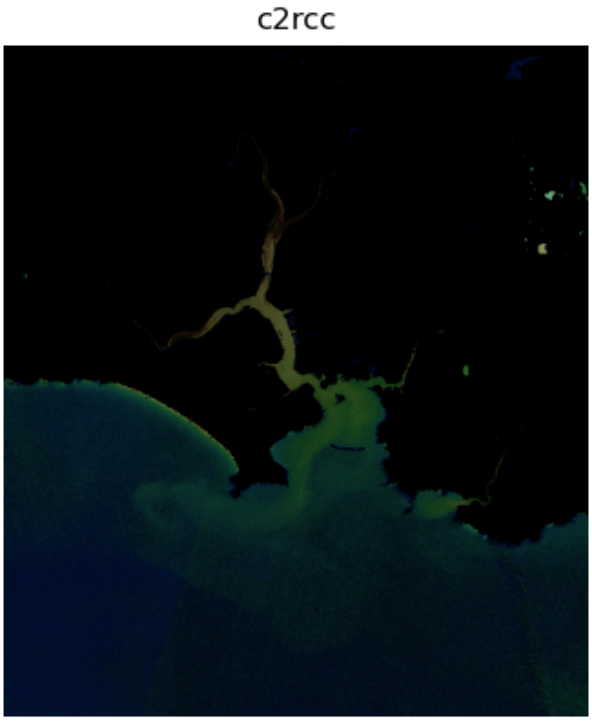

Figure 71: RGB composite of the MSI sample scene over Tamar processed by c2rcc

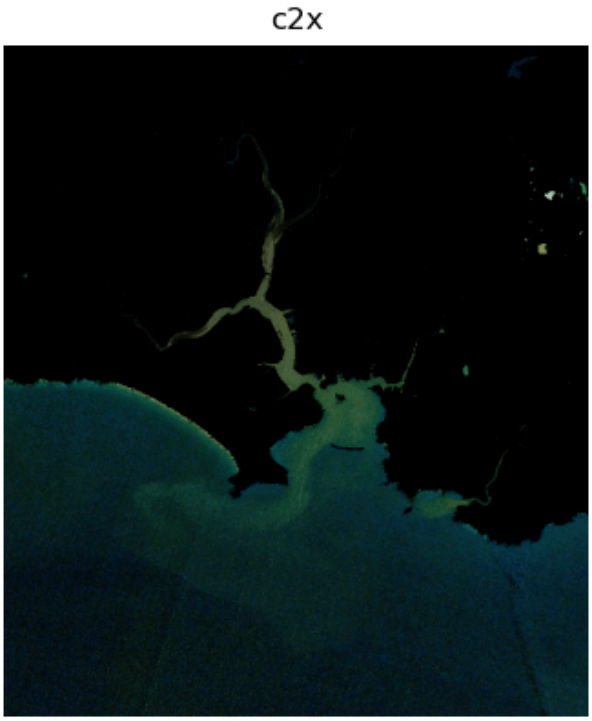

Figure 72: RGB composite of the MSI sample scene over Tamar processed by c2x

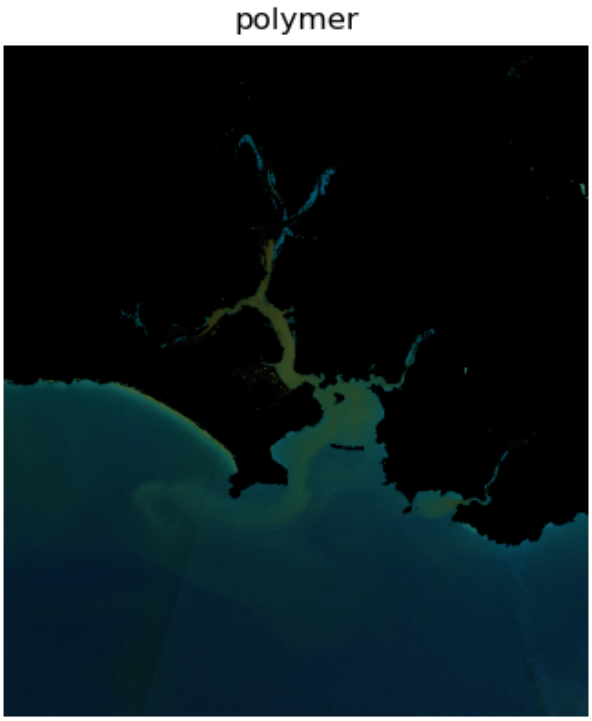

Figure 73: RGB composite of the MSI sample scene over Tamar processed by polymer

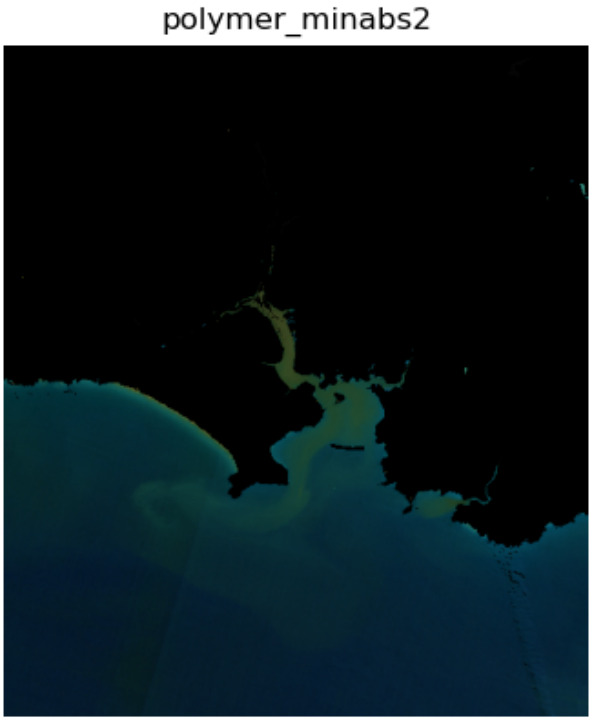

Figure 74: RGB composite of the MSI sample scene over Tamar processed by polymer_minabs2

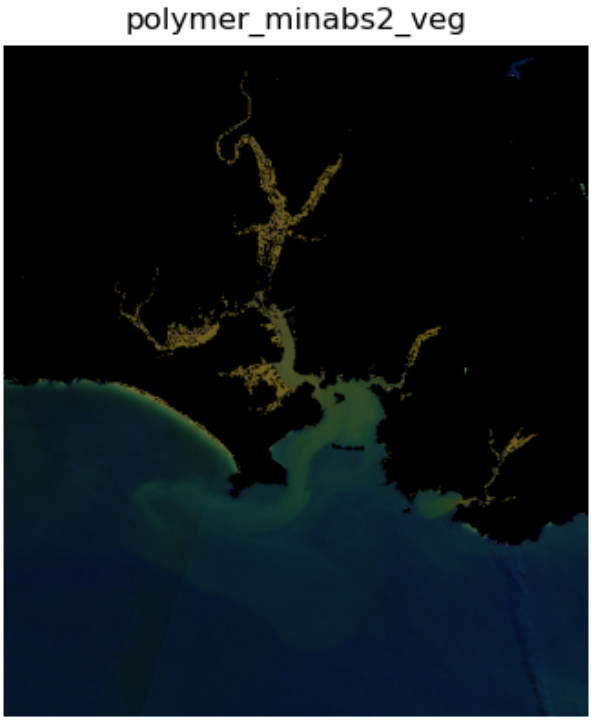

Figure 75: RGB composite of the MSI sample scene over Tamar processed by polymer_minabs2_veg

Figure 76: RGB composite of the MSI sample scene over Tamar processed by iCOR_simec

8.1.1.6 Venice (MSI)

Product name: S2A_MSIL1C_20200408T101021_N0209_R022_T32TQR_20200408T153254

Figure 77: RGB composite of the MSI sample scene over Venice processed by acolite

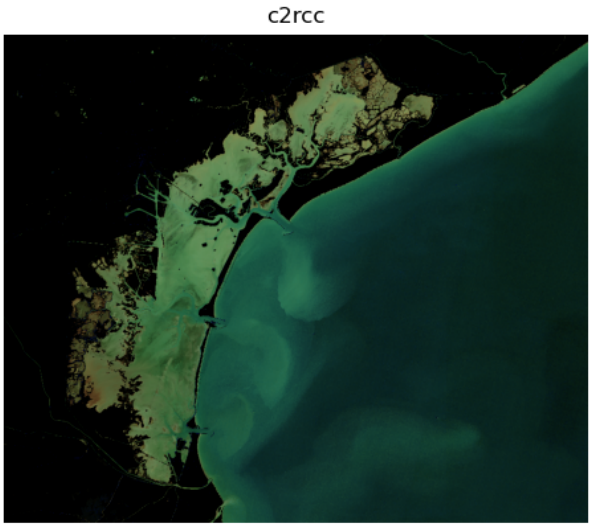

Figure 78: RGB composite of the MSI sample scene over Venice processed by c2rcc

Figure 79: RGB composite of the MSI sample scene over Venice processed by c2x

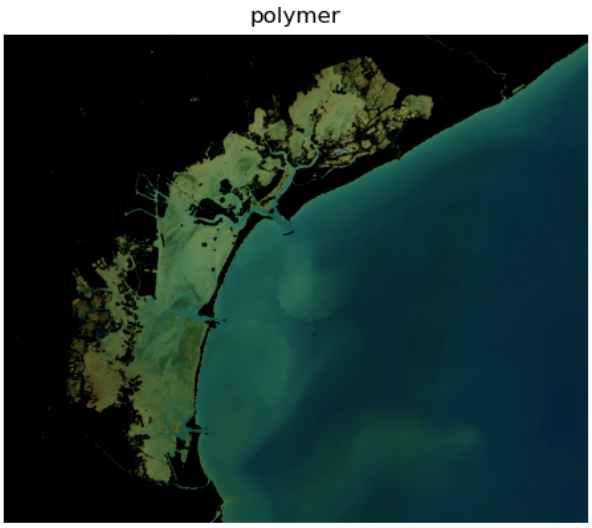

Figure 80: RGB composite of the MSI sample scene over Venice processed by polymer

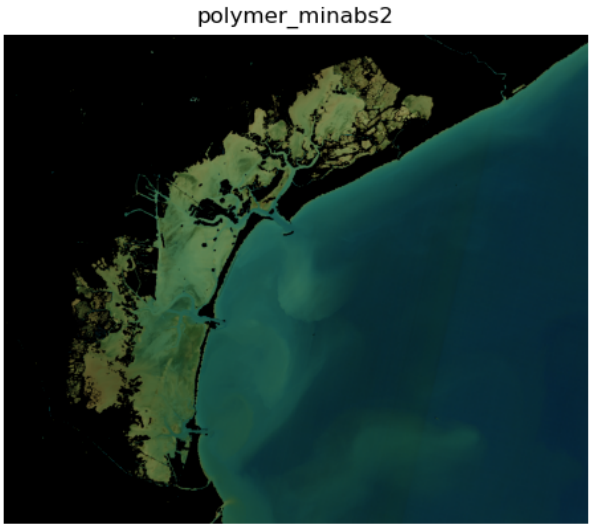

Figure 81: RGB composite of the MSI sample scene over Venice processed by polymer_minabs2

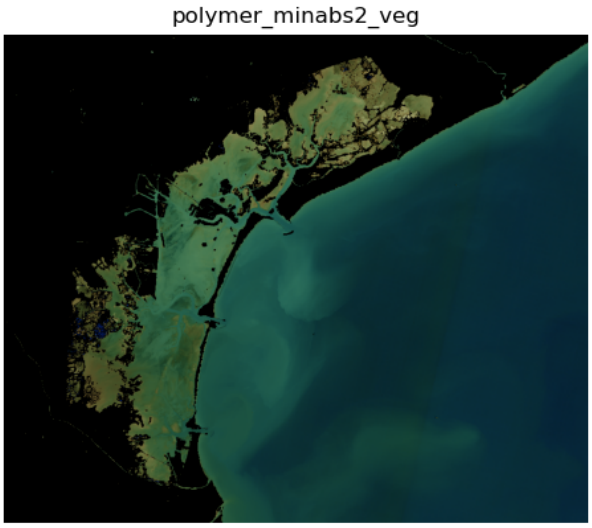

Figure 82: RGB composite of the MSI sample scene over Venice processed by polymer_minabs2_veg

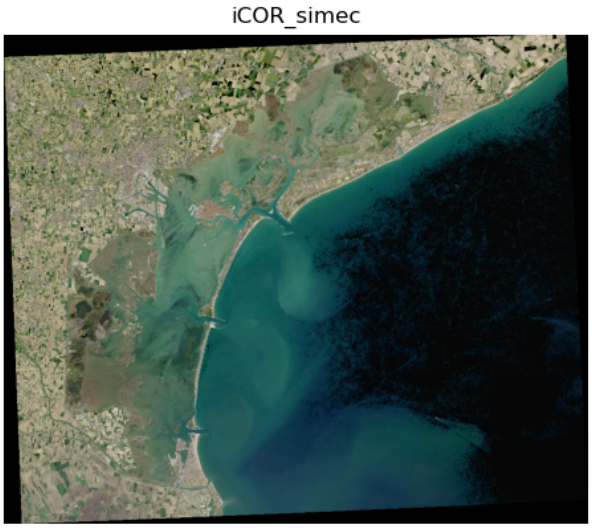

Figure 83: RGB composite of the MSI sample scene over Venice processed by iCOR_simec

8.1.2 OLCI

8.1.2.1 Elbe (OLCI)

Product name: S3A_OL_1_EFR____20200406T101735_20200406T102035_20200407T150905_0179_057_008_1980_LN1_O_NT_002

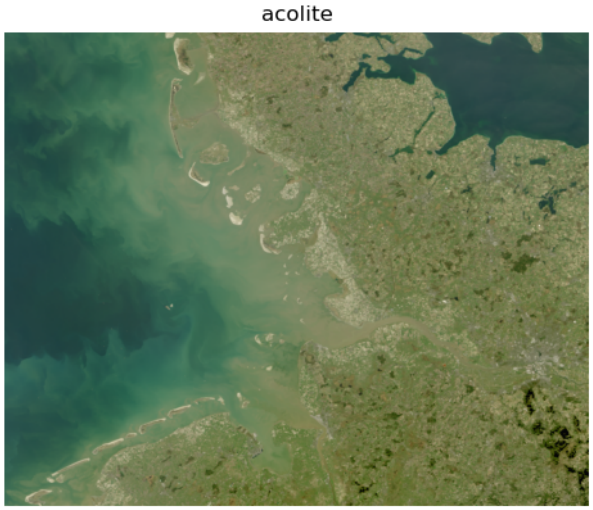

Figure 84: RGB composite of the OLCI sample scene over Elbe processed by acolite

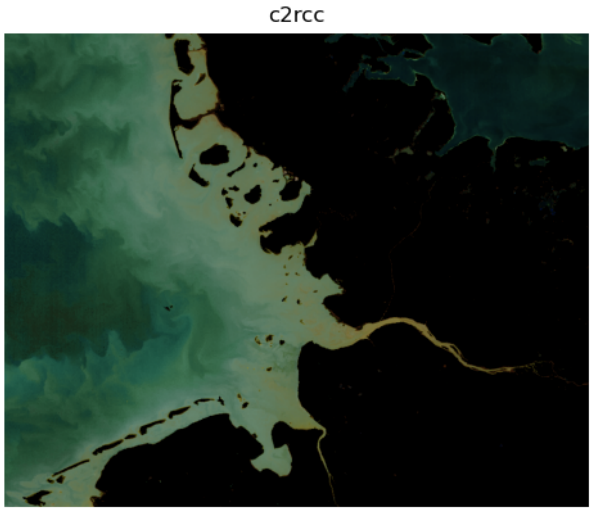

Figure 85: RGB composite of the OLCI sample scene over Elbe processed by c2rcc

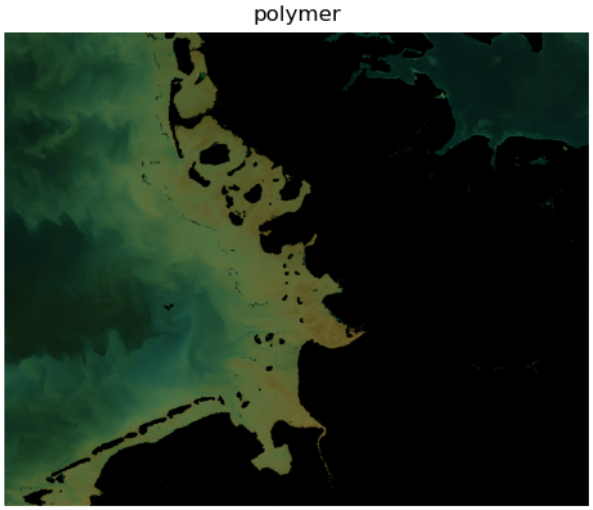

Figure 86: RGB composite of the OLCI sample scene over Elbe processed by polymer

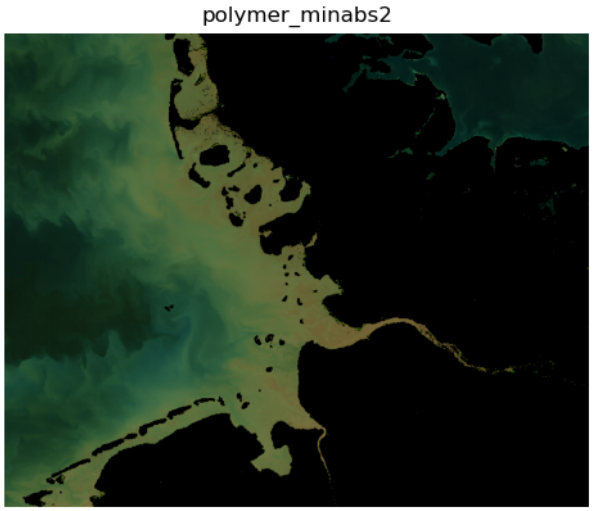

Figure 87: RGB composite of the OLCI sample scene over Elbe processed by polymer_minabs2

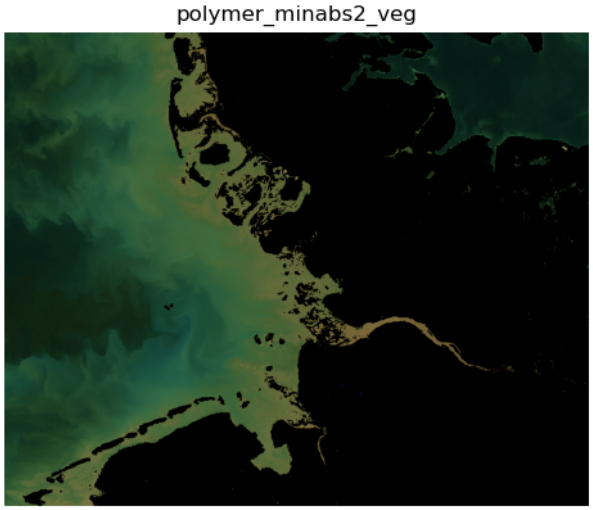

Figure 88: RGB composite of the OLCI sample scene over Elbe processed by polymer_minabs2_veg

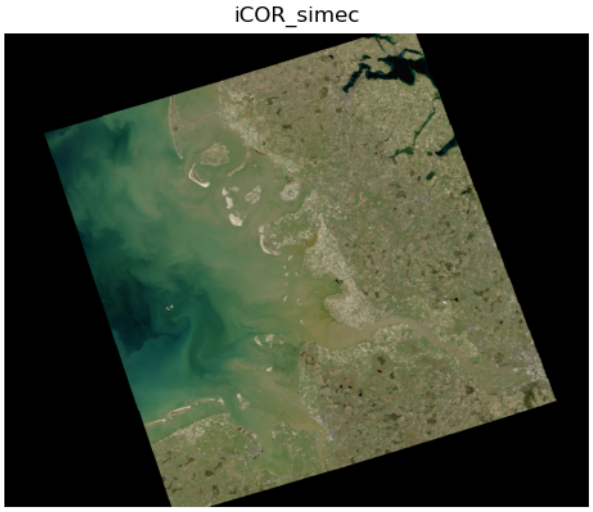

Figure 89: RGB composite of the OLCI sample scene over Elbe processed by iCOR_simec

8.1.2.2 Curonian (OLCI)

Product name: S3B_OL_1_EFR____20200406T093801_20200406T094101_20200407T134625_0179_037_250_1980_LN1_O_NT_002

Figure 90: RGB composite of the OLCI sample scene over Curonian processed by acolite

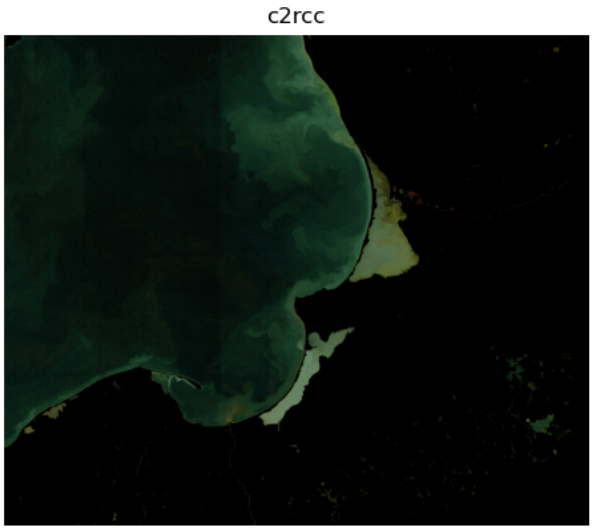

Figure 91: RGB composite of the OLCI sample scene over Curonian processed by c2rcc

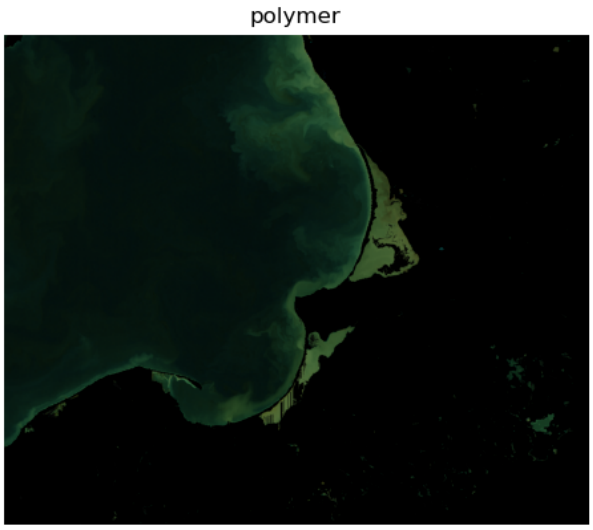

Figure 92: RGB composite of the OLCI sample scene over Curonian processed by polymer

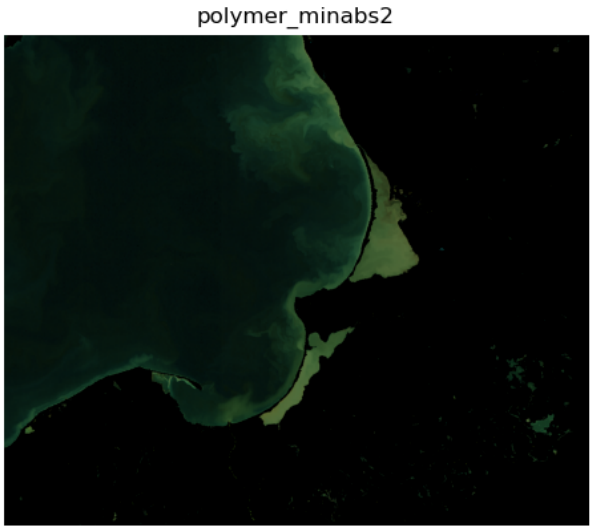

Figure 93: RGB composite of the OLCI sample scene over Curonian processed by polymer_minabs2

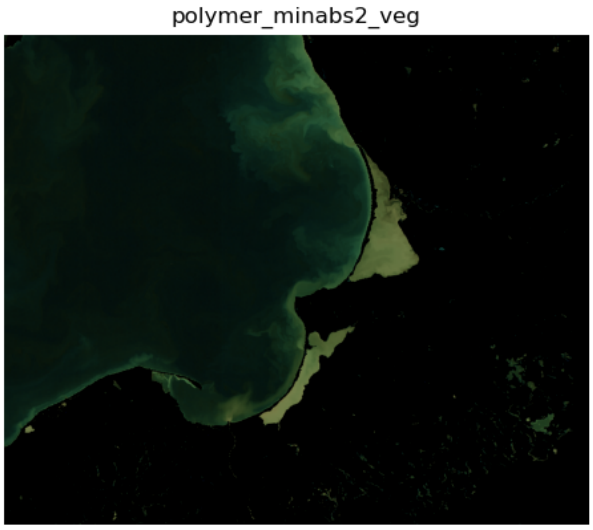

Figure 94: RGB composite of the OLCI sample scene over Curonian processed by polymer_minabs2_veg

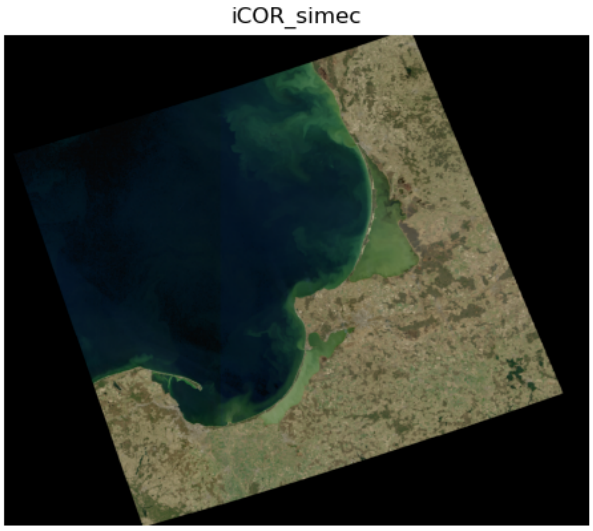

Figure 95: RGB composite of the OLCI sample scene over Curonian processed by iCOR_simec

8.1.2.3 Danube (OLCI)

Product name: S3A_OL_1_EFR____20200402T084320_20200402T084620_20200403T124743_0179_056_335_2160_LN1_O_NT_002

Figure 96: RGB composite of the OLCI sample scene over Danube processed by acolite

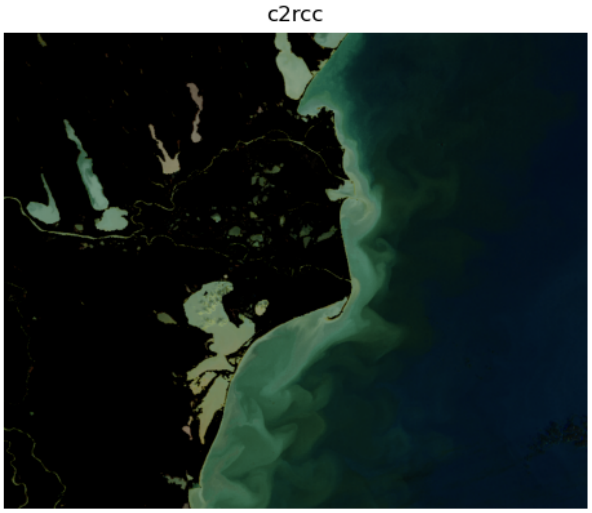

Figure 97: RGB composite of the OLCI sample scene over Danube processed by c2rcc

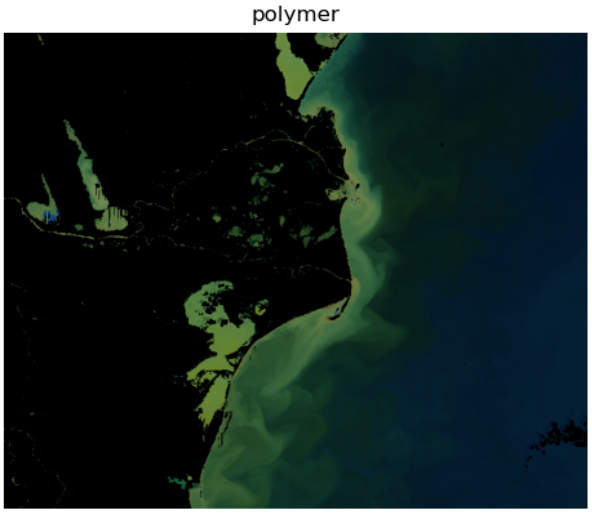

Figure 98: RGB composite of the OLCI sample scene over Danube processed by polymer

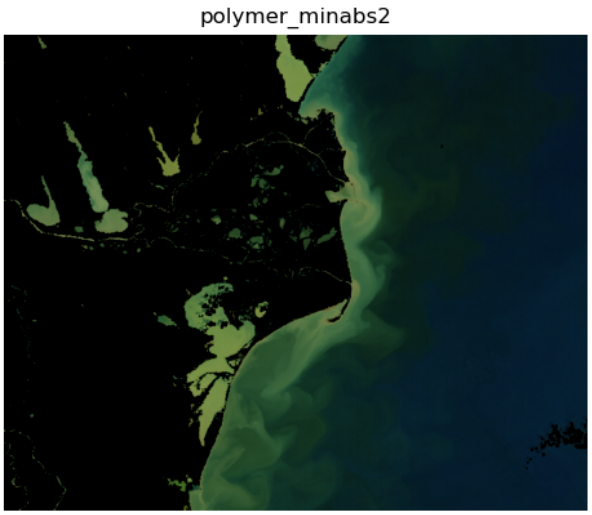

Figure 99: RGB composite of the OLCI sample scene over Danube processed by polymer_minabs2

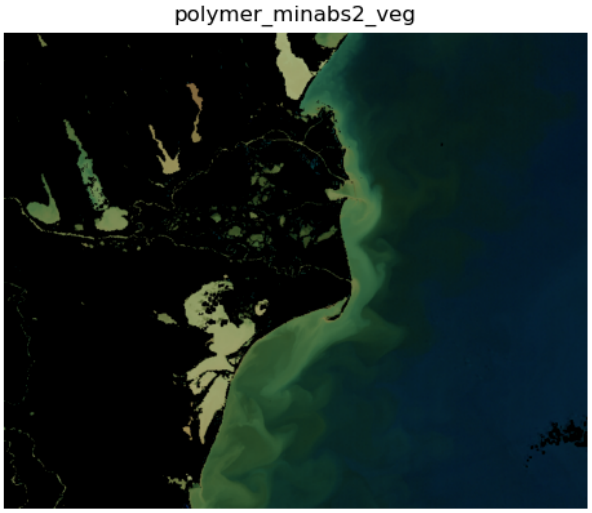

Figure 100: RGB composite of the OLCI sample scene over Danube processed by polymer_minabs2_veg

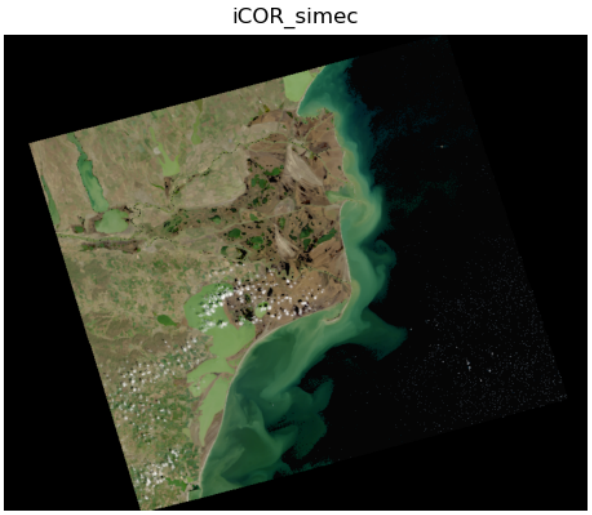

Figure 101: RGB composite of the OLCI sample scene over Danube processed by iCOR_simec

8.1.2.4 Tagus (OLCI)

Product name: S3A_OL_1_EFR____20200402T102719_20200402T103019_20200403T142621_0179_056_336_2340_LN1_O_NT_002

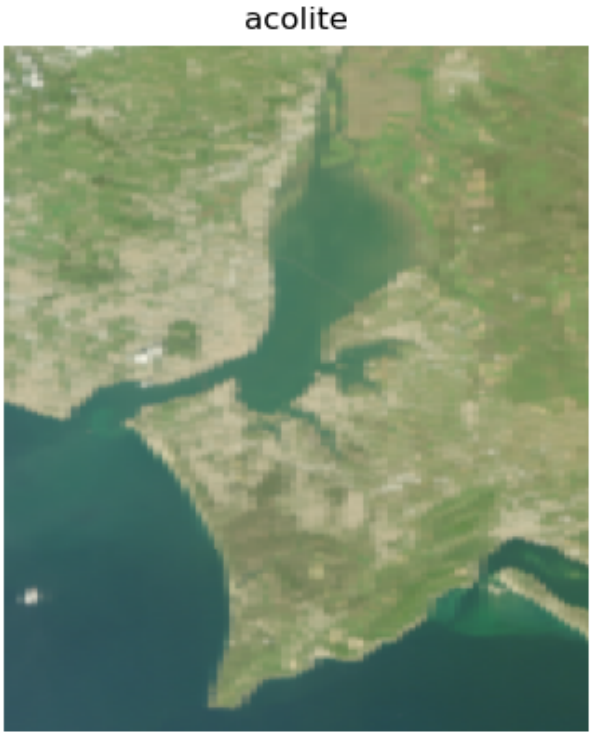

Figure 102: RGB composite of the OLCI sample scene over Tagus processed by acolite

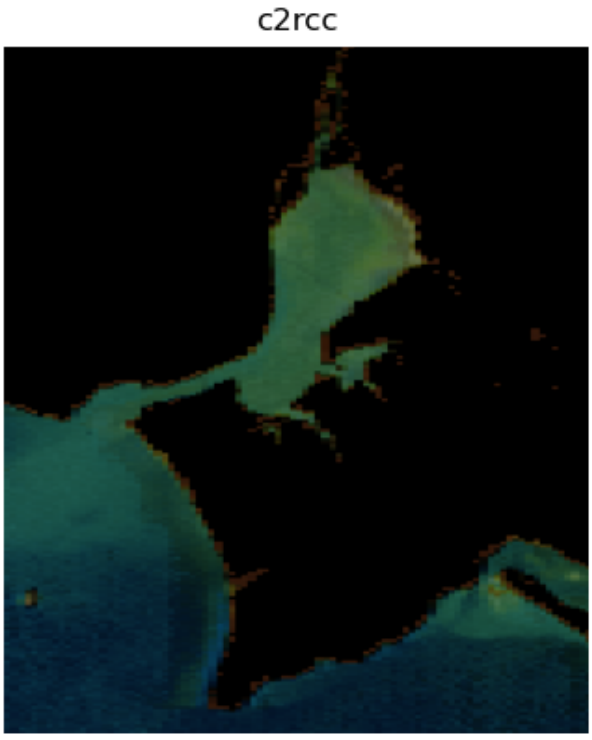

Figure 103: RGB composite of the OLCI sample scene over Tagus processed by c2rcc

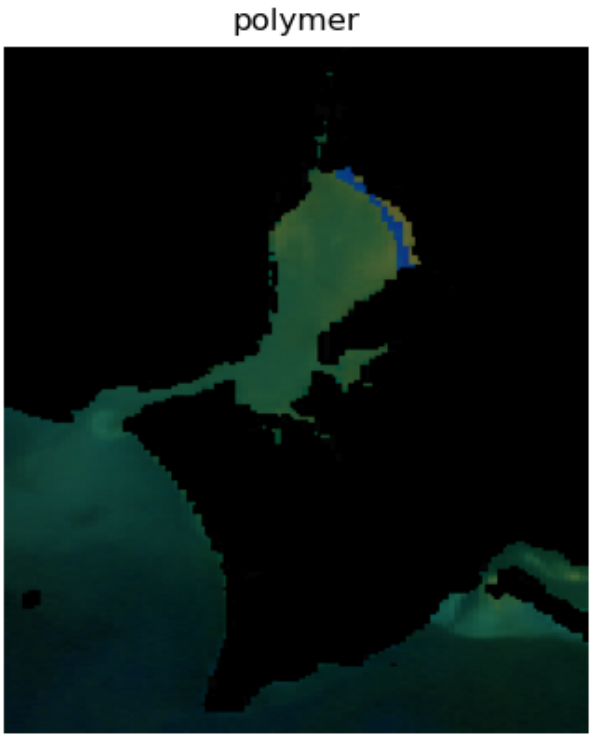

Figure 104: RGB composite of the OLCI sample scene over Tagus processed by polymer

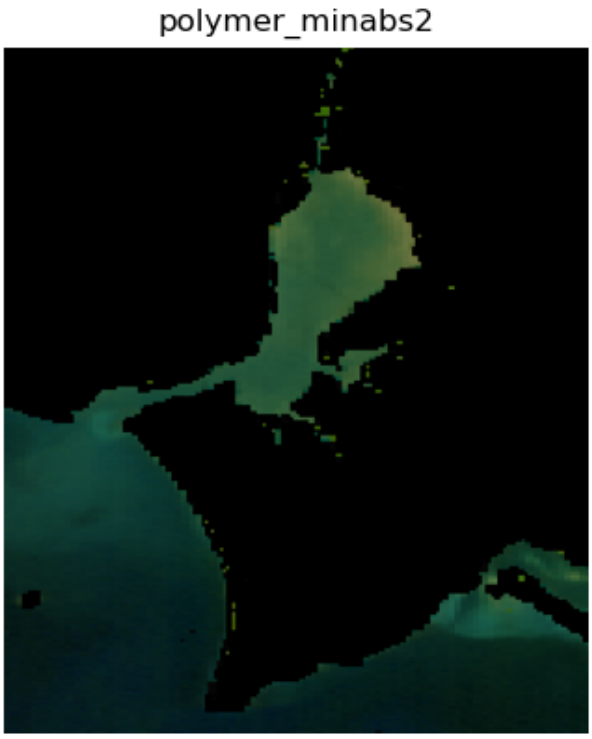

Figure 105: RGB composite of the OLCI sample scene over Tagus processed by polymer_minabs2

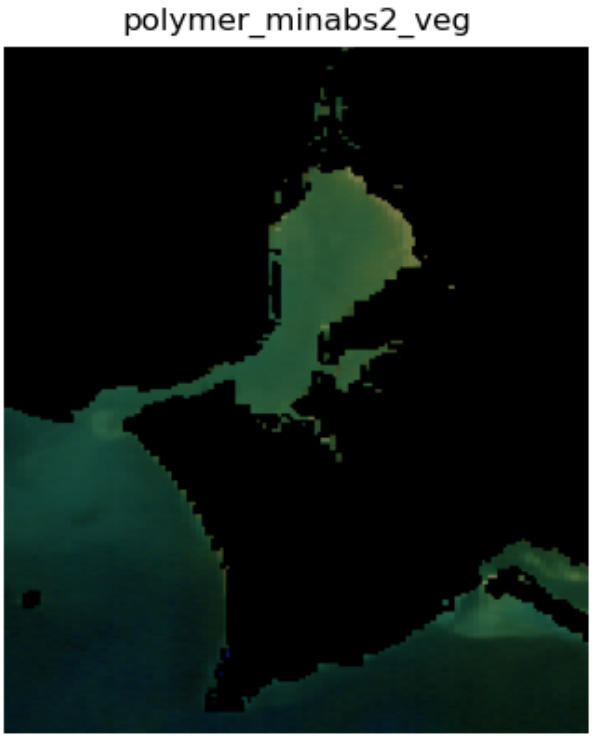

Figure 106: RGB composite of the OLCI sample scene over Tagus processed by polymer_minabs2_veg

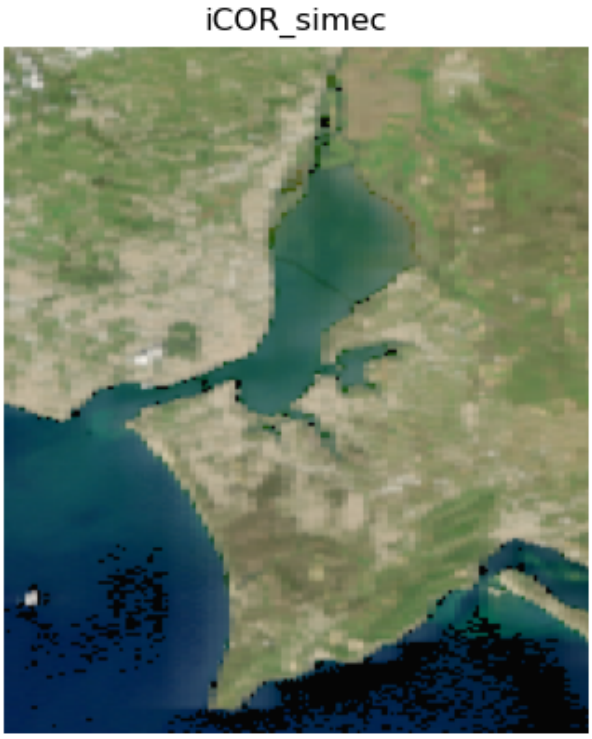

Figure 107: RGB composite of the OLCI sample scene over Tagus processed by iCOR_simec

8.1.2.5 Tamar (OLCI)

Product name: S3A_OL_1_EFR____20200404T110957_20200404T111257_20200405T144706_0179_056_365_1980_LN1_O_NT_002

Figure 108: RGB composite of the OLCI sample scene over Tamar processed by acolite

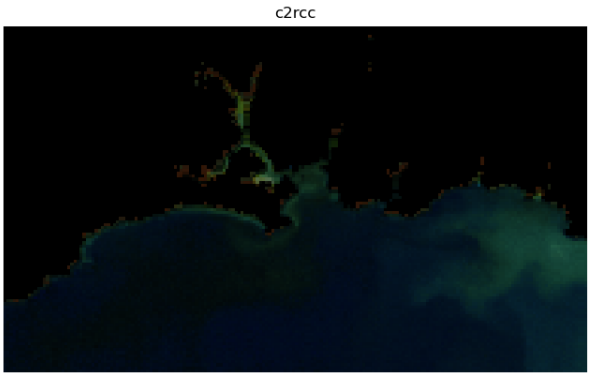

Figure 109: RGB composite of the OLCI sample scene over Tamar processed by c2rcc

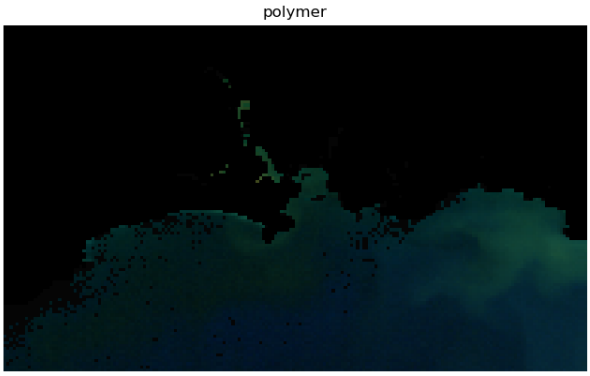

Figure 110: RGB composite of the OLCI sample scene over Tamar processed by polymer

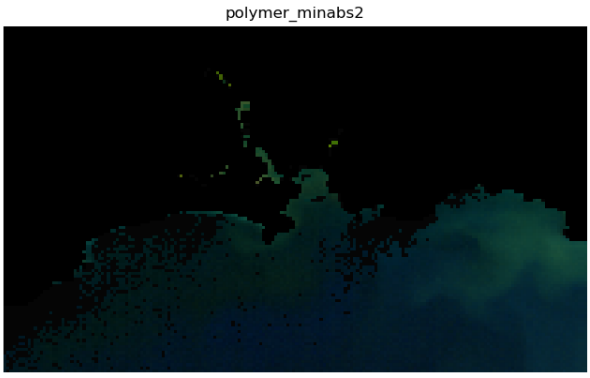

Figure 111: RGB composite of the OLCI sample scene over Tamar processed by polymer_minabs2

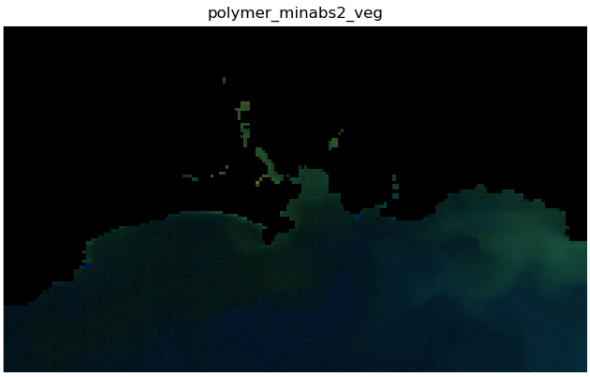

Figure 112: RGB composite of the OLCI sample scene over Tamar processed by polymer_minabs2_veg

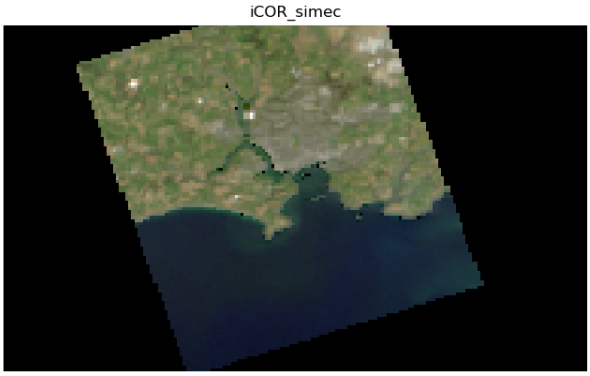

Figure 113: RGB composite of the OLCI sample scene over Tamar processed by iCOR_simec

8.1.2.6 Venice (OLCI)

Product name: S3A_OL_1_EFR____20170420T093144_20170420T093444_20180417T025441_0179_016_364_2160_LR2_R_NT_002

Figure 114: RGB composite of the OLCI sample scene over Venice processed by acolite

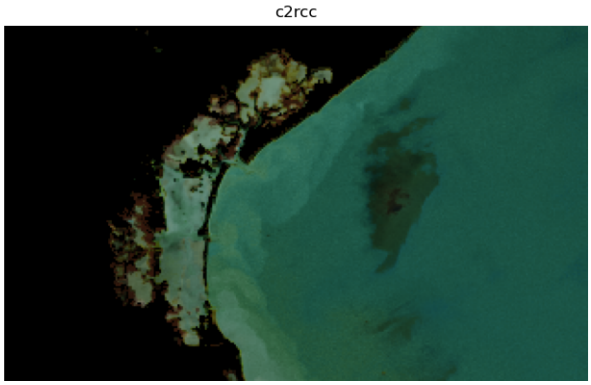

Figure 115: RGB composite of the OLCI sample scene over Venice processed by c2rcc

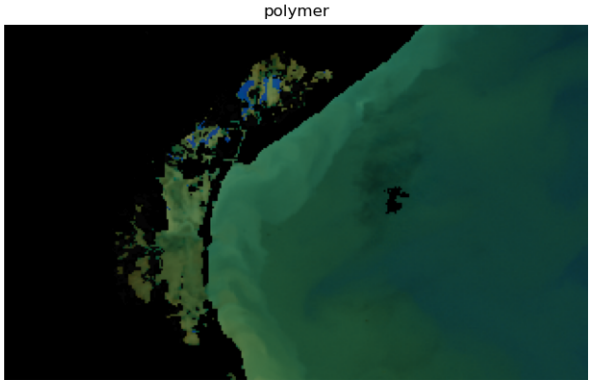

Figure 116: RGB composite of the OLCI sample scene over Venice processed by polymer

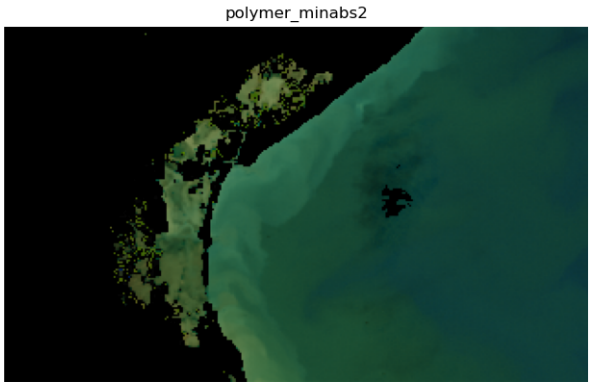

Figure 117: RGB composite of the OLCI sample scene over Venice processed by polymer_minabs2

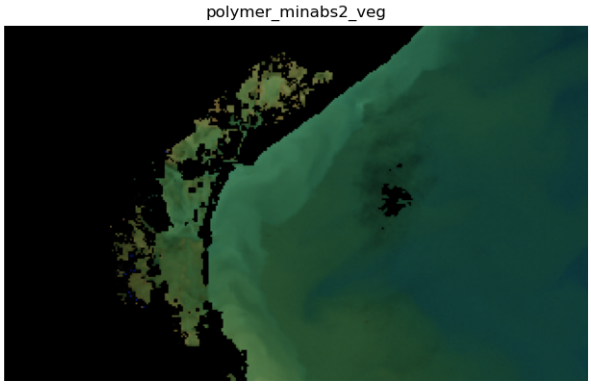

Figure 118: RGB composite of the OLCI sample scene over Venice processed by polymer_minabs2_veg

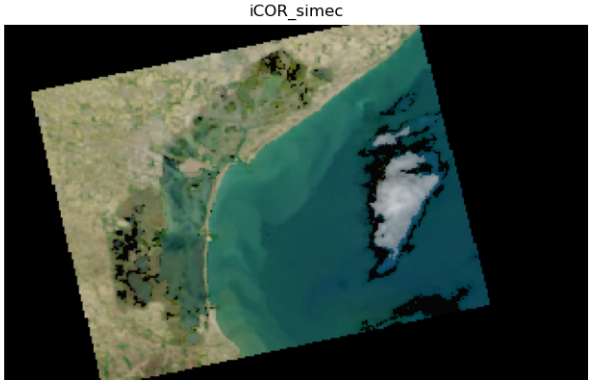

Figure 119: RGB composite of the OLCI sample scene over Venice processed by iCOR_simec

8.2 Annex 2: Merged products

8.2.1 MSI

8.2.1.1 Elbe

Product name: S2A_MSIL1C_20200407T104021_N0209_R008_T32UME_20200407T110356

8.2.1.1.1 Merged product

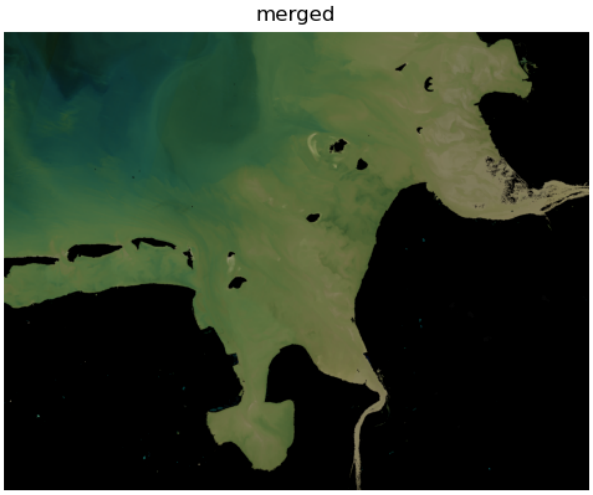

Figure 120: Merged product for MSI sample scene (Elbe)

8.2.1.1.2 Algorithm merging

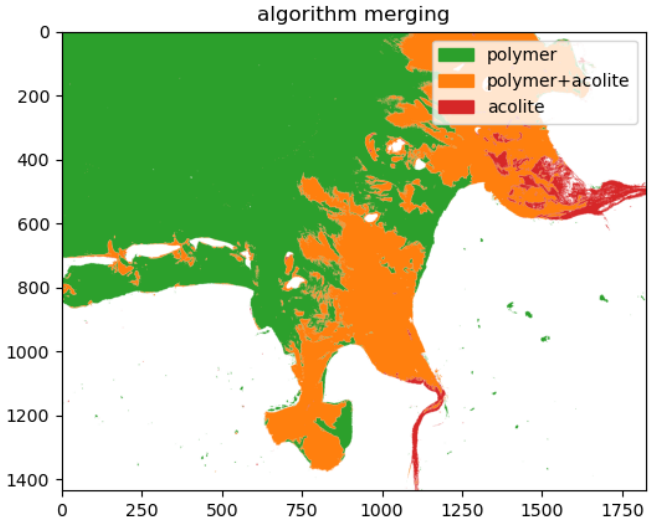

Figure 121: Algorithm regions for the merged product (sample scene Elbe)

8.2.1.2 Curonian

Product name: S2B_MSIL1C_20200410T100029_N0209_R122_T34UDF_20200410T125625

8.2.1.2.1 Merged product

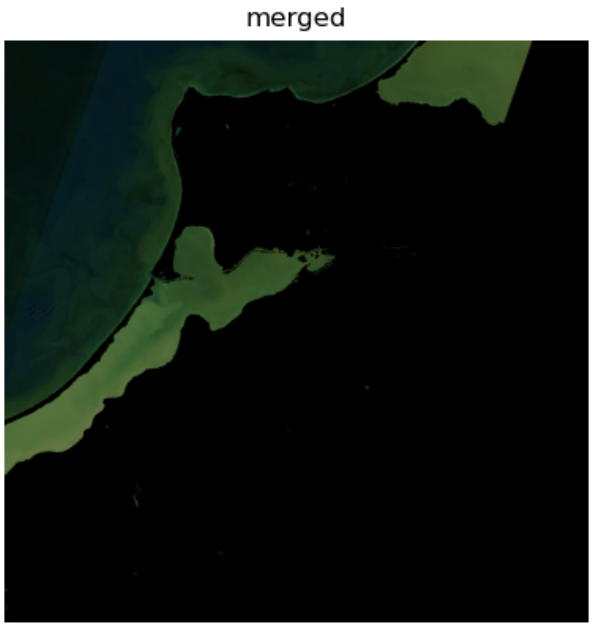

Figure 122: Merged product for MSI sample scene (Curonian)

8.2.1.2.2 Algorithm merging

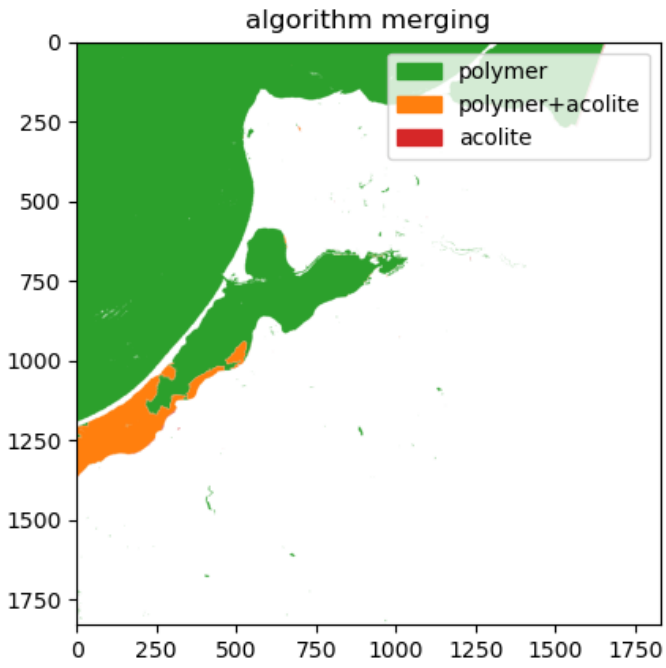

Figure 123: Algorithm regions for the merged product (sample scene Curonian)

8.2.1.3 Danube

Product name: S2A_MSIL1C_20200407T085551_N0209_R007_T35TPK_20200407T103455

8.2.1.3.1 Merged product

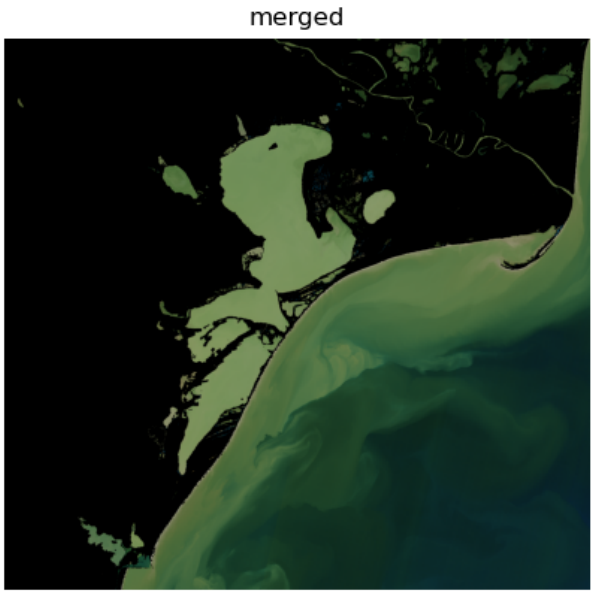

Figure 124: Merged product for MSI sample scene (Danube)

8.2.1.3.2 Algorithm merging

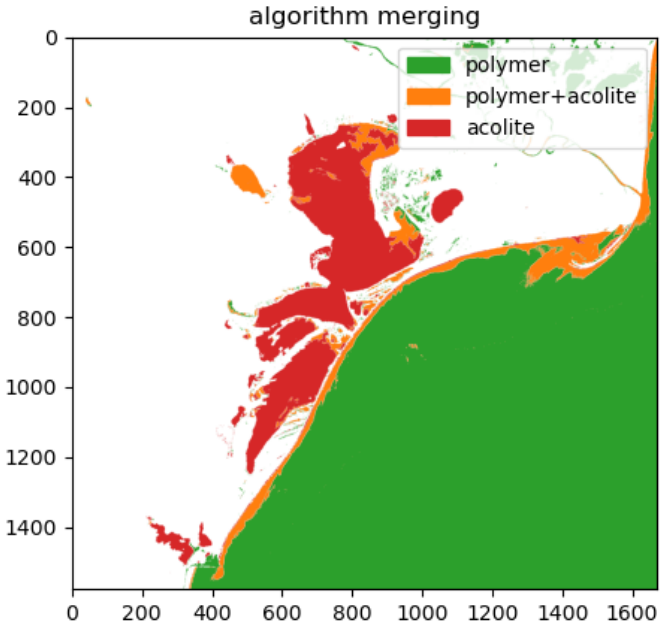

Figure 125: Algorithm regions for the merged product (sample scene Danube)

8.2.1.4 Tagus

Product name: S2B_MSIL1C_20200424T112109_N0209_R037_T29SMC_20200424T123554

8.2.1.4.1 Merged product

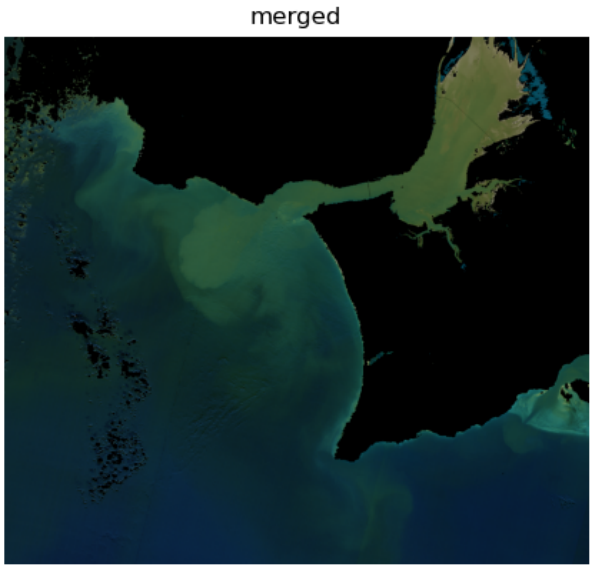

Figure 126: Merged product for MSI sample scene (Tagus)

8.2.1.4.2 Algorithm merging

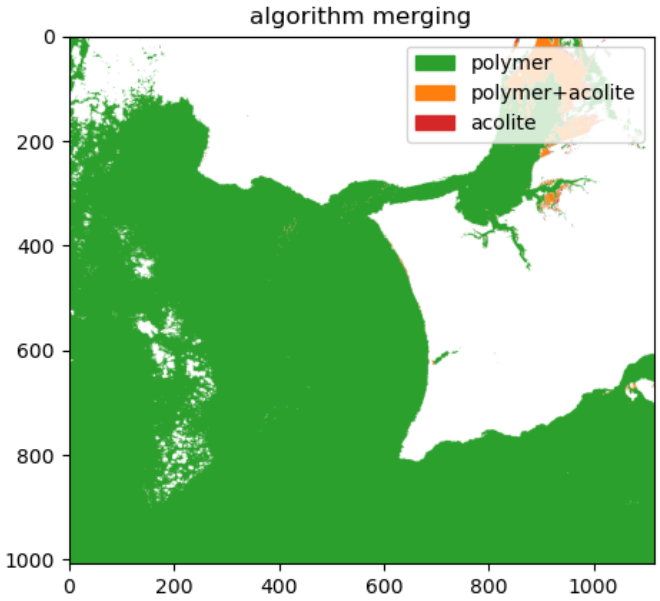

Figure 127: Algorithm regions for the merged product (sample scene Tagus)

8.2.1.5 Tamar

Product name: S2A_MSIL1C_20200409T112111_N0209_R037_T30UVA_20200409T132421

8.2.1.5.1 Merged product

Figure 128: Merged product for MSI sample scene (Tamar)

8.2.1.5.2 Algorithm merging

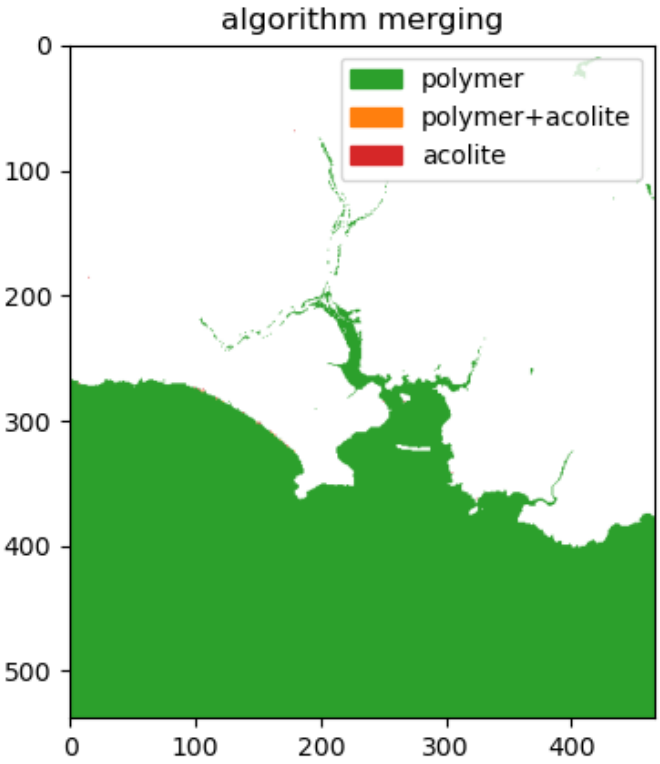

Figure 129: Algorithm regions for the merged product (sample scene Tamar)

8.2.1.6 Venice

Product name: S2A_MSIL1C_20200408T101021_N0209_R022_T32TQR_20200408T153254

8.2.1.6.1 Merged product

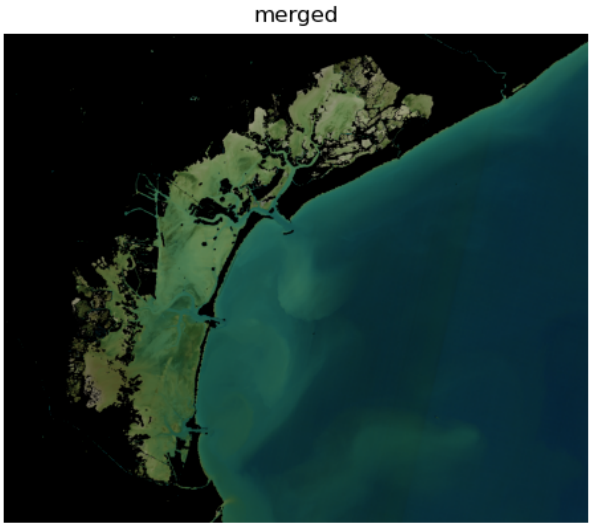

Figure 130: Merged product for MSI sample scene (Venice)

8.2.1.6.2 Algorithm merging

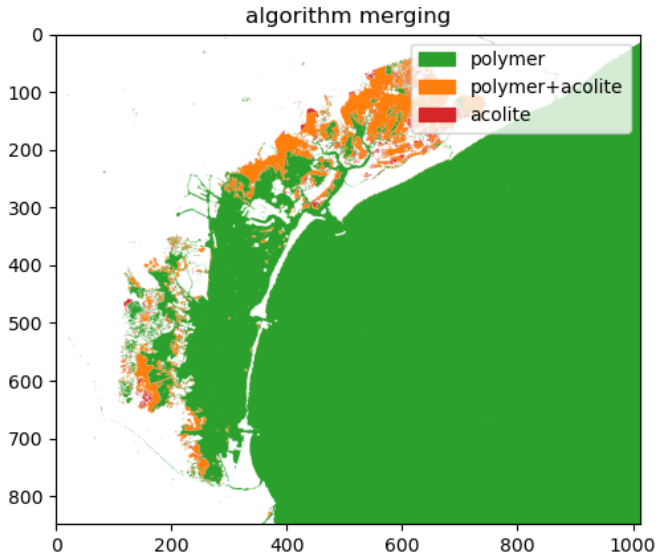

Figure 131: Algorithm regions for the merged product (sample scene Venice)

8.2.2 OLCI

8.2.2.1 Elbe

Product name:
S3A_OL_1_EFR____20200406T101735_20200406T102035_20200407T150905_0179_057_008_1980_LN1_O_NT_002

8.2.2.1.1 Merged product

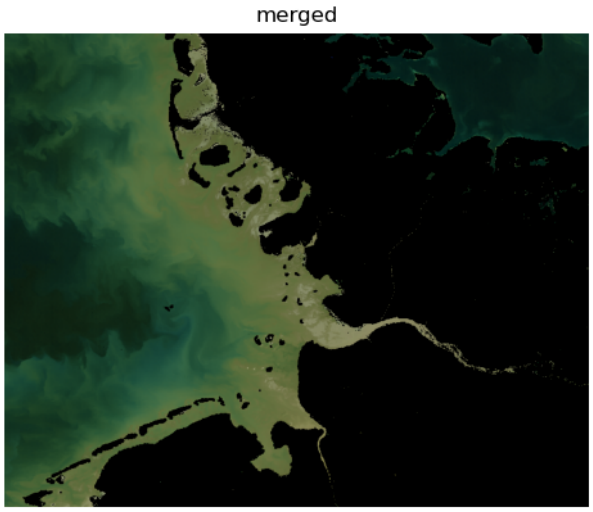

Figure 132: Merged product for OLCI sample scene (Elbe)

8.2.2.1.2 Algorithm merging

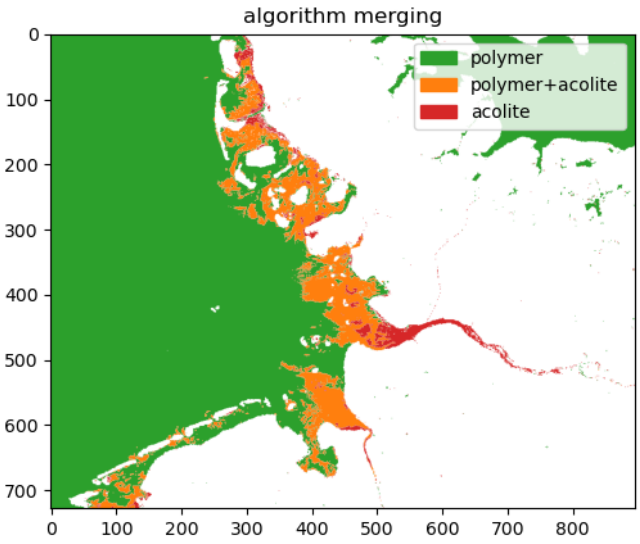

Figure 133: Algorithm regions for the merged product (sample scene Elbe)

8.2.2.2 Curonian

Product name:
S3B_OL_1_EFR____20200406T093801_20200406T094101_20200407T134625_0179_037_250_1980_LN1_O_NT_002

8.2.2.1.1 Merged product

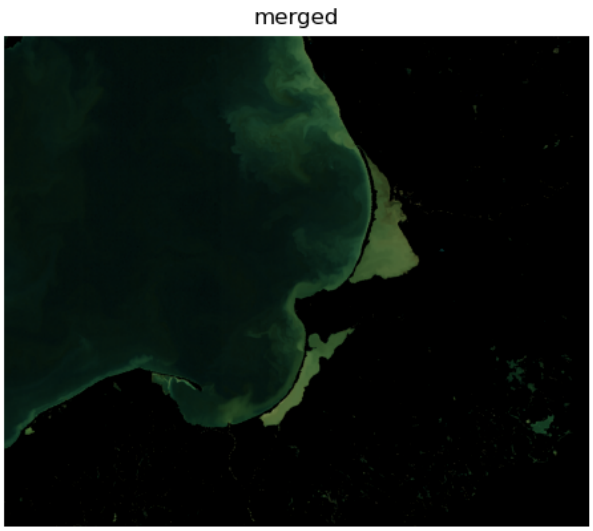

Figure 134: Merged product for OLCI sample scene (Curonian)

8.2.2.2.2 Algorithm merging

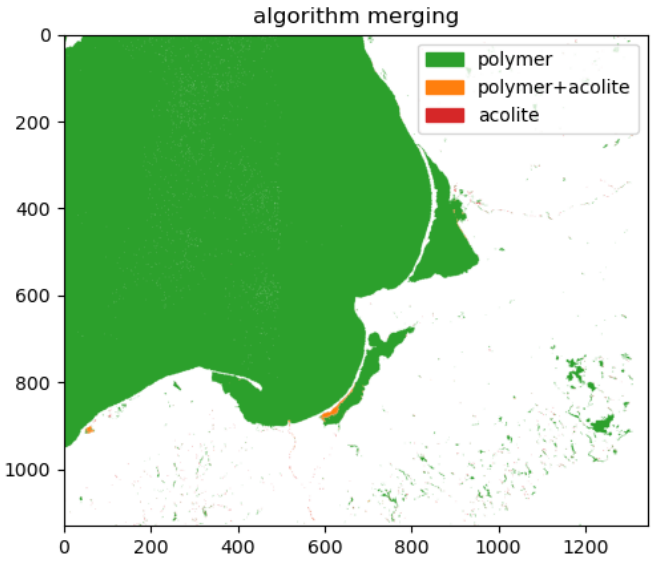

Figure 135: Algorithm regions for the merged product (sample scene Curonian)

8.2.2.3 Danube

Product name:
S3A_OL_1_EFR____20200402T084320_20200402T084620_20200403T124743_0179_056_335_2160_LN1_O_NT_002

8.2.2.3.1 Merged product

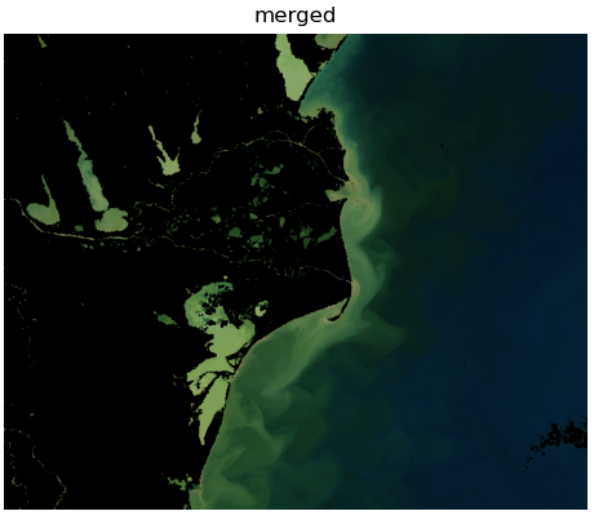

Figure 136: Merged product for OLCI sample scene (Danube)

8.2.2.3.2 Algorithm merging

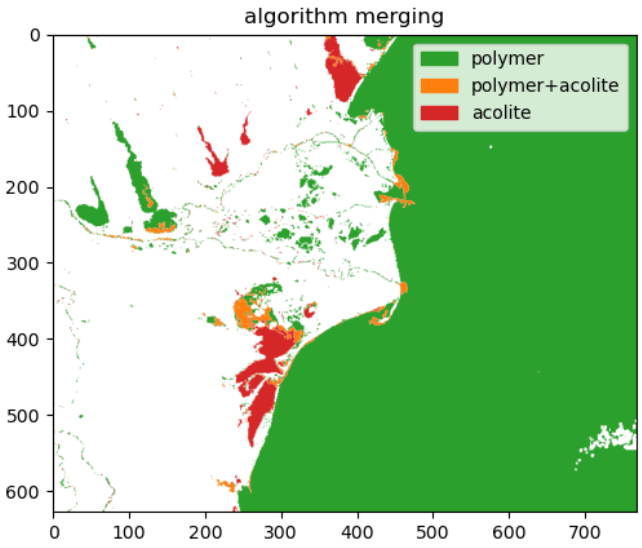

Figure 137: Algorithm regions for the merged product (sample scene Danube)

8.2.2.4 Tagus

Product name:
S3A_OL_1_EFR____20200402T102719_20200402T103019_20200403T142621_0179_056_336_2340_LN1_O_NT_002

8.2.2.4.1 Merged product

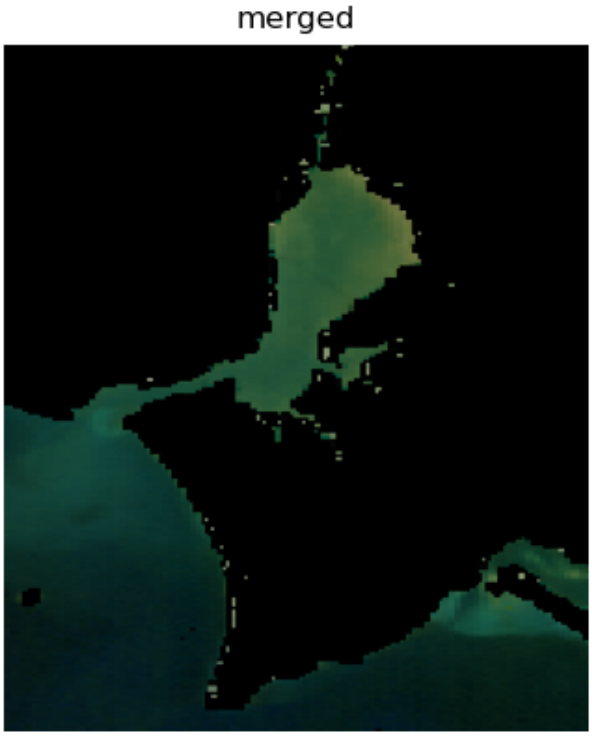

Figure 138: Merged product for OLCI sample scene (Tagus)

8.2.2.4.2 Algorithm merging

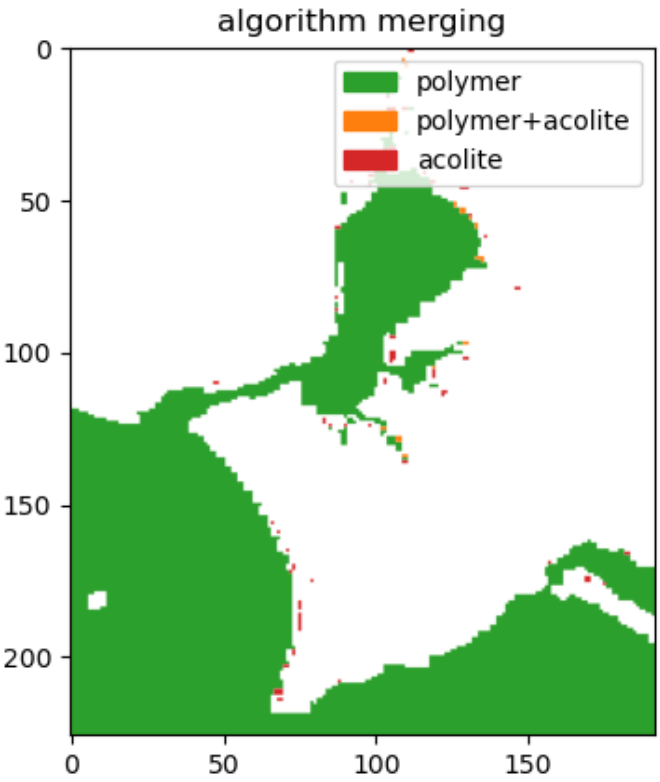

Figure 139: Algorithm regions for the merged product (sample scene Tagus)

8.2.2.5 Tamar

Product name:
S3A_OL_1_EFR____20200404T110957_20200404T111257_20200405T144706_0179_056_365_1980_LN1_O_NT_002

8.2.2.5.1 Merged product

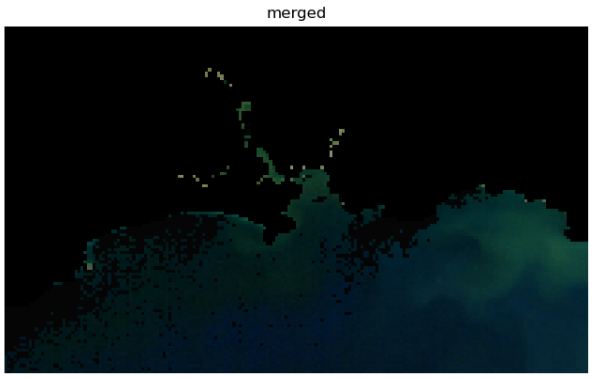

Figure 140: Merged product for OLCI sample scene (Tamar)

8.2.2.5.2 Algorithm merging

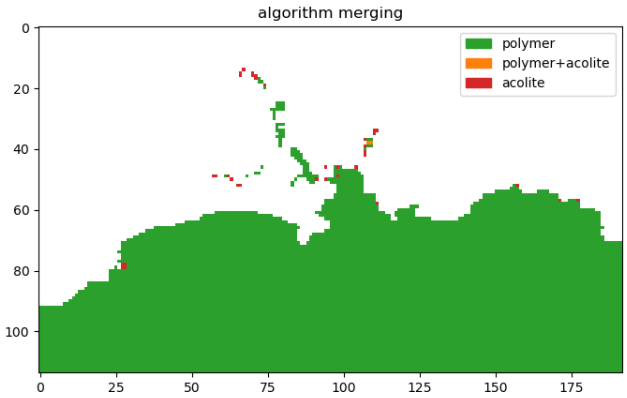

Figure 141: Algorithm regions for the merged product (sample scene Tamar)

8.2.2.6 Venice

Product name:S3A_OL_1_EFR____20170420T093144_20170420T093444_20180417T025441_0179_016_364_2160_LR2_R_NT_002

8.2.2.6.1 Merged product

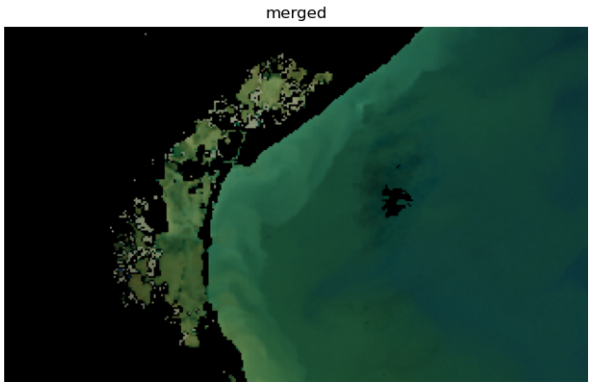

Figure 142: Merged product for OLCI sample scene (Venice)

8.2.2.6.2 Algorithm merging

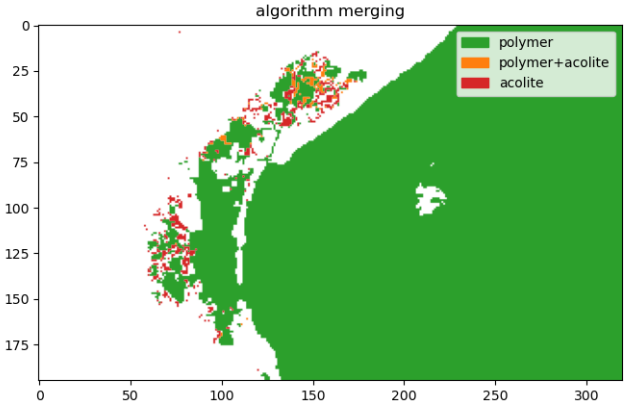

Figure 143: Algorithm regions for the merged product (sample scene Venice)